Alma Mater Studiorum - Università di Bologna

Dipartimento di Fisica e Astronomia
Corso di Laurea Magistrale in Astrofisica e Cosmologia

Multiwavelength analysis of the radio source 3C111 through VLBA observations

Tesi di Laurea Magistrale

Presentata da:
Vieri Bartolini

Relatore:
Chiar.mo Prof.
Daniele Dallacasa
Co-Relatori:
Dr. Marcello Giroletti
Dr. Josè Luis Gómez
Dr. Rocco Lico

Appello IV
Anno Accademico 2020-2021

To those who know

This Thesis work was done as part of the research activity of the Instituto Astrofísica Andalucía - Consejo Superior de Investigaciones Científicas (IAA-CSIC) in Granada, in cooperation with the Istituto di Radioastronomia - Istituto Nazionale di Astrofisica (IRA-INAF) in Bologna.

Sommario

Nel corso di questa tesi verranno presentati i risultati dell'analisi di osservazioni a più lunghezze d'onda della galassia attiva 3C111, ottenute con il Very Long Baseline Array (VLBA) nel maggio 2014. Le osservazioni sono state effettuate a 5, 8,5, 15, 21, 43 e 86 GHz. Il VLBA è un array di telescopi indipendenti in Nord America, che osserva utilizzando la tecnica della Very Long Baseline Interferometry (VLBI). Questo tipo di interferometria fornisce la più alta risoluzione spaziale di qualsiasi strumento astronomico disponibile. L'emissione radio dalle galassie attive (AGN) è uno dei fenomeni più interessanti e ricchi di informazioni fra quelli accessibili con la tecnica del VLBI. Gli AGN sono eccellenti laboratori per una varietà di processi fisici estremi. Il modello standard degli AGN suggerisce la presenza di un buco nero supermassiccio (SMBH) al centro della galassia, che accresce la materia ed è circondato da un toro oscurante. La complessa dinamica nei dintorni del SMBH e la presenza di intensi campi magnetici, possono portare alla produzione di due flussi di plasma di particelle cariche, che emettono radiazione di sincrotrone, chiamati getti con orientamento opposto l'uno all'altro. 3C111 contiene uno dei nuclei più luminosi alla lunghezza d'onda millimetrica rispetto a molte altre galassie e presenta un'emissione variabile di diversi Jy. Su scale del pc e inferiori, si osserva un getto one-sided dovuto ad effetti di amplificazione relativistica con un'apparente moto superluminale. Oltre a queste caratteristiche, data la sua vicinanza, 3C111 ($z = 0.049$), è un oggetto eccellente per studiare la fisica dei getti con mm-VLBI. I dati raccolti con il VLBA sono calibrati, producendo immagini della sorgente con la più alta risoluzione possibile per questo array 86 GHz. Oltre alle immagini di intensità totale, vengono calcolate anche le mappe di polarizzazione per tutte le bande. Attraverso il confronto delle immagini di intensità totale è possibile calcolare le mappe di indice spettrale per tutte le coppie di frequenze adiacenti. Inoltre, per alcune terzine di frequenze è anche possibile calcolare le mappe della misura di rotazione (RM). Al fine di fornire relazioni tra caratteristiche distinte nel getto, la distribuzione spaziale dell'emissione in ciascuna banda è modellata con un insieme di componenti Gaussiane circolari. Per ciascuna di esse viene fornita una stima della temperatura di brillanza (con un massimo di $T_{B,max} \approx 1,3 \times 10^{12}$ K e un minimo di $T_{B,min} \approx 5,2 \times 10^{8}$ K) e il campo magnetico (con un massimo di $H_{max} \approx 57$ mG e un minimo di $H_{min} \approx 7.5 \times 10^{-2}$ mG). Per ognuno dei parametri fisici trovati durante il model fitting delle componenti, viene fornita una relazione che risulta più o meno accurata, a seconda dei parametri considerati. I parametri determinati nell'ambito di questo studio, potranno essere di grande utlità come vincoli con cui confrontare gli output delle numerose simulazioni numeriche in fase di produzione.

Abstract

This thesis will present the results of the analysis of multi-wavelength observations of the active galaxy 3C111, obtained with the Very Long Baseline Array (VLBA) in May 2014. The observations were made at 5, 8.5, 15, 21, 43, and 86 GHz. The VLBA is an array of independent telescopes in North America, observing using the Very Long Baseline Interferometry (VLBI) technique. This type of interferometry provides the highest spatial resolution of any astronomical instrument available. Radio emission from active galaxies (AGNs) is one of the most interesting and information-rich phenomena among those accessible using the VLBI technique. AGNs are excellent laboratories for a variety of extreme physical processes. The standard model of AGNs suggests the presence of a supermassive black hole (SMBH) at the center of the galaxy, which accretes matter and is surrounded by obscuring torus. The complex dynamics around the SMBH and the presence of intense magnetic fields, may lead to the production of two plasma streams of charged particles, emitting synchrotron radiation, called jets with opposite orientation to each other. 3C111 contains one of the brightest cores at the millimeter wavelength compared to many other galaxies and exhibits variable emission of several Jy. On pc scales and below, a one-sided jet is observed due to relativistic amplification effects with apparent superluminal motion. In addition to these features, given its proximity, 3C111 ($z = 0.049$), is an excellent object to study the physics of jets with mm-VLBI. The data gathered with the VLBA are calibrated, yielding source images with the highest resolution possible for this 86 GHz array. In addition to the total intensity images, polarization maps are also calculated for all bands. By comparing the total intensity images, spectral index maps can be calculated for all adjacent frequency pairs. Moreover, for some triplets of frequencies it is also possible to compute rotation measure (RM) maps. In order to provide relationships between distinct features in the jet, the spatial distribution of the emission in each band is modeled with a set of circular Gaussian components. For each of them, it is provided an estimate of the brightness temperature (with a maximum of $T_{B,max} \approx 1.3 \times 10^{12}$ K and a minimum of $T_{B,min}(T_{B,max} \approx 5.2 \times 10^{8}$ K) and the magnetic field (with a maximum of $H_{max} \approx 57$ mG and a minimum of $H_{min} \approx 7.5 \times 10^{-2}$ mG). For each of the physical quantities found during the model fitting of the components, a relation is provided that is more or less accurate, depending on the parameters considered. The parameters determined as part of this study, will be of great utility as constraints against which to compare the outputs of the numerous numerical simulations.

Contents

Chapter 1

Introduction

In the first Chapter of this thesis it will be introduced and briefly explained the Active Galactic Nuclei (AGN) system, its structure, its morphology, the emission processes behind it and the state of the art about them. This introduction does not claim to be a complete review of the AGN but only a general view of the subject. For a more extended review see Padovani et al. (2017).

1.1 A brief presentation of Active Galactic Nuclei

Like normal galaxies, active galaxies are systems of stars, gases, and dust that are tied through gravity. However, active galaxies contain a nucleus with extreme luminosity (up to $L_{bol} \approx 10^{48}\,\mathrm{erg\ s^{-1}}$) and compact size (pc scale). AGN are energetic astrophysical sources powered by accretion onto supermassive black holes (SMBHs), and present unique observational signatures that cover the full electromagnetic spectrum over more than twenty orders of magnitude in frequency. It is thought that almost every galaxy has at its center a SMBH but only $\approx 5\%$ of them is considered active.
Since the discovery of quasars (QUASi-stellAR radio sources or QSOs) in 1963 (Schmidt (1963)), the study of these phenomena has grown exponentially and it is considered now a whole new branch of astronomy. AGN have many interesting properties, such as:

- Very high luminosities, which make them the most powerful non-explosive sources in the Universe and therefore visible up to very high redshifts.
- Small emitting regions in most bands, as inferred from their rapid variability implying high energy densities.
- Strong evolution of their luminosity functions and detectable emission covering the whole electromagnetic spectrum.

These galaxies are very complex systems and the exact way of how they work is still uncertain.

1.2 The AGN zoo

AGN activity is visible in various types of source classification, based on which emission appears particularly relevant. In the following the so-called *zoo* will be briefly presented.

- **Radiogalaxies**: they are usually associated with giant elliptical galaxies with non thermal nuclear emission. They can reach very high luminosities up to $L_{bol} \approx 10^{47}$ erg/s. These objects are further divided into **FR I** and **FR II** Fanaroff & Riley (1974), based on their radio emission and morphology.
  The FRI radiogalaxies are characterized (at 1.4 GHz) by jet dominated emission ending into low-surface brightness lobes and a power of $P_{1.4\ \mathrm{GHz}} < 10^{24.5}$ W/Hz. A jet can appear as one-sided close to the core, but beyond a few kpc it becomes two-sided and continuous. Sometimes, the host galaxy is in a cluster. As the galaxy moves through the intra-cluster medium, the gas can sweep back and distort the radio structure through ram pressure, which explains why narrow-angle-tail or wide-angle-tail sources, appear to be derived from the FR I class of objects.
  On the other hand, FR II radiogalaxies, are called edge-brightened, since the most luminous parts are the hot-spots, namely the termination shock of the jet interacting with the ambient medium. Their power at 1.4 GHz is $P_{1.4\ \mathrm{GHz}} > 10^{24.5}$ W/Hz. In these sources, it is usually possible to find a one-side jet at kpc scales or even closer to the core. The environment of FR-II sources seems to be less "crowded" than the FR I one.
  Recently a third class, **FR 0**, was suggested by Baldi et al. (2016), which includes radiogalaxies sharing the properties of FR I but lacking prominent extended radio emission, being a ≈ 30 times more core-dominated. Most of the radiosources are thought to be FR0.

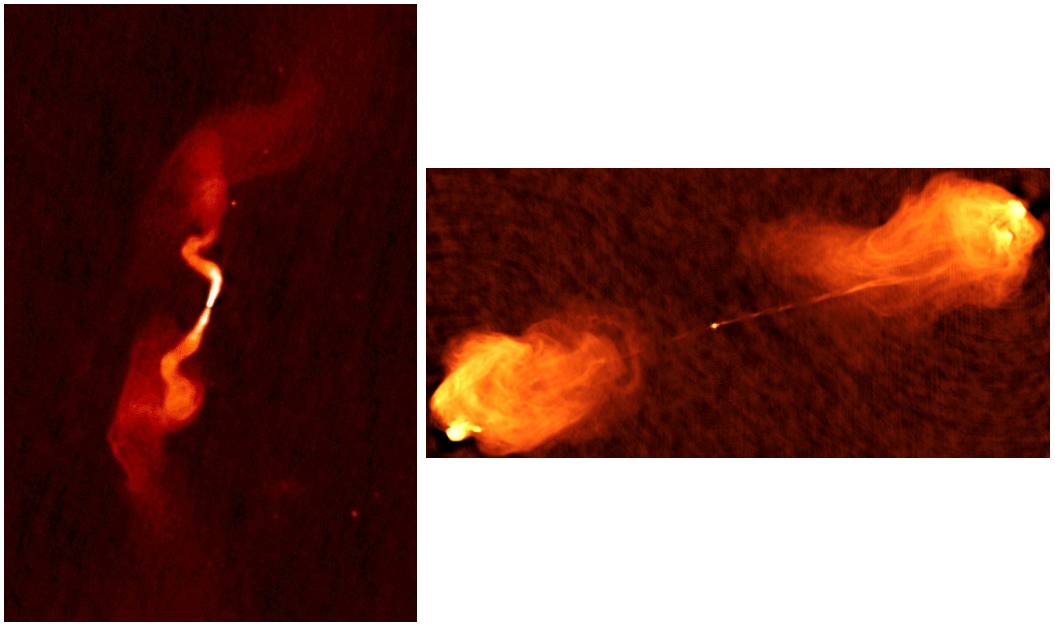

Figure 1.1: The comparison between the two types of the Fanaroff-Riley classification. **Left:** The FR I radio galaxy 3C31 at 1.4 GHz. Image Credit: NRAO/AUI 1999. **Right:** The FR II radio galaxy Cygnus A at 5 GHz. Image Credit: Carilli & Barthel 1996

- **Quasars**: as suggested by their name, since QSOs are dominated by a very compact emission they look point-like as the stars. These are characterized by a strong variability both in their SED and in their morphology, broad spectral lines mostly in emission, high redshift and a non thermal emission. As it will be discussed in section 1.5, these objects are AGN with the jet that lies at a small angle with respect to the line of sight. Just as radiogalaxies, also quasars can be divided into two classes: Radio Loud and Radio Quiet. The difference revolves around the radio emission with respect to the optical one (1.3.1). Even though their discovery was made in the radio domain, the majority of QSOs are thought to be Radio Quiet. In addition to that, it is common to divide quasars based on their radio spectrum: if $\alpha \geq 0.5$ then the object is called Steep Spectrum Radio Quasar (**SSRQ**), in the other case ($\alpha < 0.5$) the source is called Flat Spectrum Radio Quasar (**FSRQ**). These two different groups roughly correspond respectively to extended and compact sources.

- **BL Lac**: BL Lacertae (BL Lac) objects are characterized by an optical spectrum, which at most shows weak emission lines, sometimes displays absorption features, and in some cases can be completely featureless. Similarly to QSOs, these objects have their jet pointed towards the observer. BL Lac together with FSRQs are the two main sub-classes of **Blazars**. Blazars are a class of AGN with extreme variability even on very short timescales. In addition to that they emits strongly polarized radiation and they usually show strong X-ray emission as well.

- **Seyfert galaxies**: discovered in 1943, these objects are mostly spiral galaxies with a strong nuclear activity dominated by non thermal radiation. A Seyfert

galaxy has a quasar-like nucleus, but the host galaxy is clearly detectable. Seyfert galaxies are QSO at low redshift and therefore the host galaxy can be seen. Also for these objects, there is a division: **Seyfert I** and **Seyfert II**. The main difference is in the strong spectral lines that are present mostly in the optical part of the spectrum. Seyfert I galaxies have mostly permitted spectral lines with both broad and narrow FWMH, while Seyfert II have both permitted and prohibited spectral lines but only with narrow FWMH ($\lesssim$ 1000 km/s). This is shown in the right panel of the Fig. 1.2.

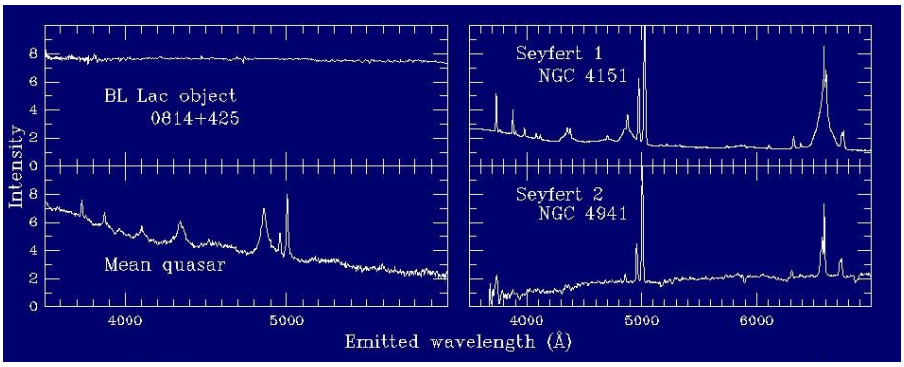

Figure 1.2: The comparison between the optical spectra of different galaxies. **Left:** The BL Lac object 0814+425 spectrum (Credit: Lawrence et. al, 1996) and the "mean quasar" spectrum from a composite generated by Francis et. al, 1991. **Right:** The Seyfert I galaxy NGC 4151 spectrum (Credit: William C. Keel) and the Seyfert II galaxy NGC 4941 spectrum (Credit: Keel, 1983). These spectrum were taken from the web page of Dr. W. C. Keel `https://pages.astronomy.ua.edu/keel/agn/spectra.html`.

- **LINERs**: The Low-Ionization Nuclear Emission-line Region galaxies (LINERs) are rather controversial because AGN activity signatures are generally weak (e.g., lack of highly ionized atomic emissions and direct disk emission features). Near-infrared observations often find that the high star formation rate of LINER's host galaxies produce signatures similar to those of AGN. On the other hand, LINERs are found mostly in spiral galaxies and associated with compact radio emission feature in the centers of the galaxies. The compact radio emission is believed to originate from the hot BH accretion flows or weak radio jets, which are AGN signatures. Therefore LINERs are also referred in literature to as low luminosity AGNs (LLAGNs).

This list of AGNs, it is not complete but it includes most of the commonly used names to distinguish between various types of AGN.

1.3 AGN Classification

Among the various flavours of AGN classifications, in this work, particular attention will be devoted to the evidence/properties available for the radio and optical bands

1.3.1 Radio classification

A commonly used classification is the one related to the radio emission and more specifically to the rate between the flux density at 5 GHz (radio) and the one at 4400 Å (optical). This rate is commonly referred as $R_{r,o}$ and, as already mentioned, it discriminates between **Radio Loud** AGN (RL AGN) with $R_{r,o} > 10$ and **Radio Quiet** AGN (RQ AGN) with $R_{r,o} < 10$. This is an historical classification but, as stated in Padovani et al. (2017) it is obsolete because the difference in these objects is mostly intrinsic and not only observational. Therefore they suggest to use a different type of classification that discriminates between the presence (*jetted*) or not (*not-jetted*) of the relativistic jets in the AGN. Since this introduction aims at giving a general picture of these objects, both RL-RQ and jetted-non jetted classification will be used. RL AGNs emits a large fraction of their energy non-thermally and in association with powerful relativistic jets, while the multi wavelength emission of RQ AGN is dominated by thermal emission, directly or indirectly related to the accretion disk. The objects presented in 1.2, can be catalogued as follow 1.1.

Radio Loud/jetted	**Radio Quiet/non-jetted**
Radio Loud Quasars	Radio Quiet Quasars
FR I	Seyfert I
FR II	Seyfert II
BL Lac	LINERs

Table 1.1: The Radio Loud - Radio Quiet classification for the objects presented in 1.2.

1.3.2 Optical classification

For what concerns the optical part of the spectrum, AGNs are usually classified on the basis of their spectral characteristics. More specifically, the two classes are divided by looking at the spectral lines. If the source has both narrow and broad spectral lines, it is classified as **Type 1 AGN** or Broad Line Radio Galaxy (BLRG). Therefore, AGNs with these characteristics are commonly referred as Type 1 Quasars, Type 1 FR I, and so on. On the other hand, if there are only narrow lines in the spectrum, the object is referred as **Type 2 AGN** or Narrow Line Radio Galaxy (NLRG). If an AGN has only narrow lines in its spectrum, it is referred as Type 2 Quasars, Type 2 FR I, and so on. For objects like the Seyferts galaxies, there are widely used intermediates classes between 1 and 2. These optical classifications, just as the radio one, will be clearer once the unified model will be introduced 1.5. In literature, in addition to these classifications, it is widely used another one based also on the spectral lines. The division is into objects characterized by strong emission lines in their spectra, and sources which exhibited either absorption line spectra typical of giant elliptical galaxies. In general, objects without and with high-excitation emission lines in their optical spectra are referred to as **LEGs** (Low Excitation Galaxies) and **HEGs** (High Excitation Galaxies), respectively. More specifically, quasars and Seyferts belong to the HEG category, while LINERs and

elliptical galaxies are classified as LEGs. There are fundamental physical differences between these two types of radio AGN. Namely, LEGs have on average redder optical colours and higher stellar masses than HEGs . LEGs exhibit radiatively inefficient accretion, possibly fuelled by the hot phase of the inter-galactic medium (IGM), and are typically highly efficient in collimated jet production. HEGs accrete in a radiatively efficient manner, are fuelled by the cold IGM phase, are related to a strong star formation phase probably triggered by a merger and are less likely to launch collimated jets. By relating these two classes with the radiogalaxies, it has been showed that HEGs are only FRII while LEGs can be associated with both FR I and FR II.

1.4 The AGN structure

Thanks to the study of the multi-wavelength emission from the AGN, it was possible to build a model of the structure of these objects. This model, tries to explain the main physical features of the AGN system. The different components will be presented based on their distance from the center.

1.4.1 The central engine

One of the most important questions about AGN concerns the source of their emitted energy. In the black hole paradigm, the strong gravitational potential attracts surrounding matter and forces the generation of an **accretion disk**, in which matter is transported inwards while angular momentum is transported outwards due to the viscosity of the medium. Once matter reaches the innermost stable orbit (ISCO), it is accreted onto the black hole. This raises the question of the efficiency in converting masses to energy. As a matter of fact, the most efficient process is the accretion of matter onto a source of strong gravitation, namely compact objects like neutron stars or black holes. However, the maximum luminosity that can be emitted from an object with mass M is known as the *Eddington limit* or Eddington luminosity: $L_{edd} = 1.3 \times 10^{38} \dfrac{M}{M_\odot}$ ergs^{-1}. Where $M_\odot \approx 2 \times 10^{33}$ g is the solar mass. This can be demonstrated by balancing the radiation pressure P_{rad} with the gravitational force F_{grav} as shown in the Eq. 1.1.

$$\begin{aligned} P_{rad} = \frac{L}{4\pi r^2} = \frac{dE}{dtdA} = \frac{dp}{cdtdA} \Rightarrow \frac{dp}{dt} = \sigma_T \frac{L}{4\pi c r^2} = \frac{GMm_p}{r^2} = F_{grav} \Rightarrow \\ L_{edd} = \frac{4\pi G m_p c}{\sigma_T} M = 1.3 \times 10^{38} \frac{M}{M_\odot} \text{ ergs}^{-1} \end{aligned} \tag{1.1}$$

where L is the luminosity, r is the distance from the center, E is the energy, t is the time, A is the area on which the pressure applies, p is the momentum, c is the speed of light, σ_T is the Thompson cross section, G is the gravitational constant and m_p is the proton mass. Furthermore, the variability of AGN Δt places a lower limit to the size of the emission region. Since the smallest size of an object of mass M is the Schwarzschild radius $R_s = \dfrac{2GM}{c^2}$, it can be shown that: $\Delta t \gtrsim$

$10^{-5}\frac{M}{M_\odot}$ s. Nevertheless, this shows the possibility of a SMBH in the center of these galaxies. Also non-active galaxies may harbour a SMBH in their center. This has been discovered to be true, for example, in our own Galactic center known as Sagittarius A* (Sgr A*). Both the Eddington limit and the variability of AGNs do not include relativistic beaming of emission, which has to be considered especially in RLAGN, as will be discussed in 1.6.1.

Supermassive black holes

SMBHs are a scaled-up version of typical astrophysical black holes such as stellar mass black holes. As the name implies, SMBHs have extraordinarily large masses ranging between $10^6 - 10^{10} M_\odot$. It is still not fully understood how SMBHs were able to accumulate such a large mass over the cosmic time. However, during the last decades, several evolutionary pathways to produce SMBHs have been proposed. The scenarios basically suggest that SMBHs and/or their seeds were formed in the early universe when primordial cold gas in proto-galaxies condensated due to the gravity of a dark matter halo (e.g. Volonteri et al. (2012)). Observationally it has been found a strong correlation between the mass of SMBHs and the host galaxy stellar mass thus indicating that there have been strong interplay between the SMBH and its host galaxy during their evolution over cosmic time.
SMBHs can be characterized by two main parameters: their mass (M_{BH}) and spin (a). The mass is a dominant factor in determining the size of the event horizon, that is the region of space around a black hole in which the escape velocity equals the speed of light. The event horizon of a non-rotating BH is characterized by the Schwarzschild radius R_s. This implies that more massive BHs are larger, since the radius is directly proportional to the mass. Another useful definition is the gravitational radius $R_g = \frac{GM_{BH}}{c^2}$ from which it is possible to express R_s as $R_s = 2R_g$, since the gravitational radius is not affected by the BH spin. On the other hand, SMBHs in galaxies presumably have non-zero spin because of their astrophysical origin. The BH spin a is expressed in a normalized form by $a = (Jc)/(GM_{BH}^2$ where J is the BH angular momentum (the BH spin values range is $0 < a < 1$). A non-zero BH spin has an important implication because it changes the structure of the spacetime near the event horizon as well as the size of the event horizon itself.

The accretion disk

As already mentioned, gas in the vicinity of the central engine falls towards central BH due to the strong gravitational potential. In astrophysical circumstances, the gas has non-negligible angular momentum with respect to the central BH. Therefore, the gas forms a rotating flow. Such flow has different rotation speeds at different radial distances as a consequence of the Keplerian motion. Therefore, various kinds of viscosities are naturally developed between different layers. The viscosity gradually transports part of the angular momentum of the inner region to the outer region. This helps the gas to fall into the BH. Such kind of inflow is broadly called accretion flow. Observational evidence for the presence of accretion flows in AGNs includes the large bolometric luminosity of AGN and shape of the spectral energy distribution

(SED) in the optical and ultraviolet wavelengths.

The hot corona

Based on the existence of hard X-ray continuum emission in AGN (i.e., photon energies $\gtrsim 10$ keV), astronomers have suggested the existence of a rarefied coronal medium on top of the AGN accretion disk, with a very high temperature of $\approx 10^9$ K. The corona most likely contains energetic electrons and produces X-ray radiation by inverse Compton scattering of photons from accretion disks (Fig. 1.3). Moreover, the continuum X-ray photons ionize gas in the accretion disk. This results in highly ionized iron and other emission lines, which are frequently observed at X-ray energies. It is still debated if the corona is just a part of the hot accretion flow or it is a group of clouds floating above the disk. Studies suggest that the X-ray corona is often located very close to the BH. One of the important merits of observing the X-ray corona emission is that it allows us to indirectly probe geometry and properties of the inner BH accretion disk.

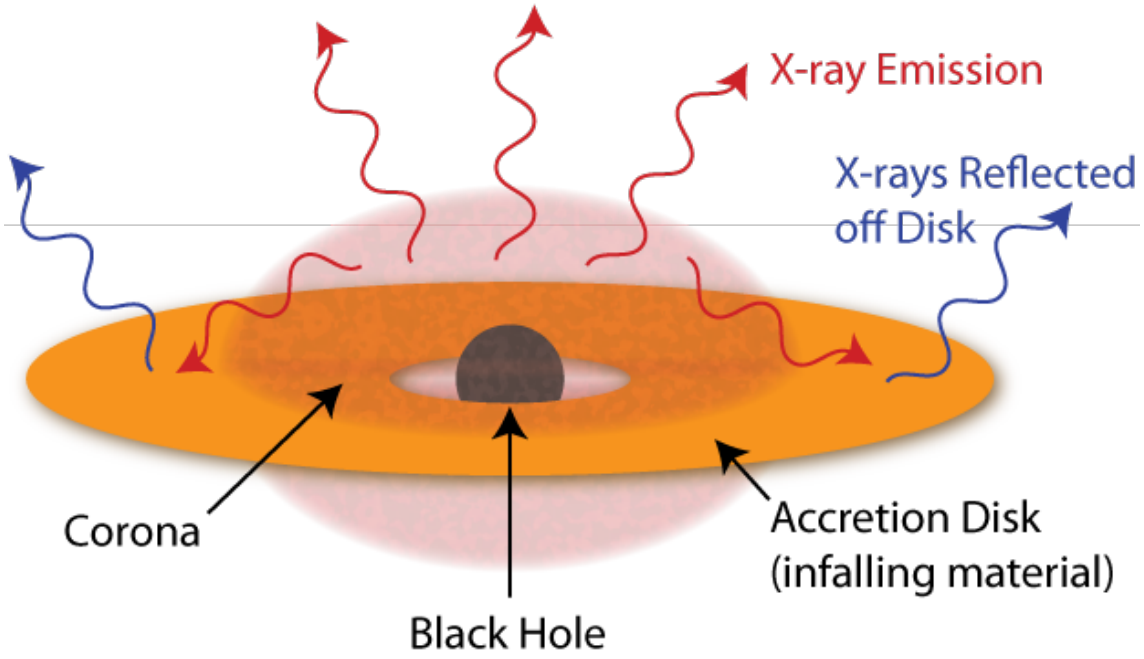

Figure 1.3: A scheme of the innermost region of an AGN. Image Credit: D. Wilkins

1.4.2 The Broad Line Region (BLR)

The gravitational potential of the central engine is strong enough to hold the gas at even larger distances from the central BH. The gas can be photo-ionized by the strong continuum radiation from the accretion disk. Therefore, they produce unique emission lines with very large line widths ($FWHMs \sim 10^3\,\mathrm{km/s}$). This region is called broad line region (BLR) and it lies at a distance from the nucleus of $\sim 0.1 - 1\,\mathrm{pc}$. It is unclear if there are groups of randomly moving clouds or if they

form an organized stream surrounding the central engine. The thermal Doppler broadening cannot reproduce the observed line widths because the corresponding kinetic temperature ($T \sim 10^8\,\mathrm{K}$), would ionize all the elements in the gas and therefore blocking the production of spectral lines. This indicates that the broad lines are produced by bulk, Keplerian random motions of the gas under strong gravity. Another interesting feature of the BLR is that the variability of this region is correlated with the variable continuum radiation from the disk. The time difference between the disk and the BLR provides an estimate of the distance of the gas from the BH.

1.4.3 The dusty torus

The torus is a key element in the unified model of AGN 1.5. This toroidal component is mainly made of dust and gas and it lies in the disk plane at a distance from the core of $\sim 1 - 100\,\mathrm{pc}$. The main effect of the torus is the obscuration of the central engine due to the dust extinction that reprocess the radiation at IR wavelengths, when it lies on the line of sight (l.o.s.). Therefore the orientation of the dusty torus with respect to the l.o.s. is what separates the type 1 and type 2 AGNs. Since it is made of dust, its temperature has to be lower than $\sim 10^3\,\mathrm{K}$ (the dust sublimation temperature). In addition to that, the internal composition of the torus is still under debate. The two main models are the *smooth* and *clumpy* torus, postulating either an homogeneous structure or a fragmented one. Another interesting feature of the torus is that its distance from the center seems to be related to the luminosity of the AGN. More luminous sources produce an higher radiation pressure that can sublimate the dust at longer distance and therefore, placing the torus further away (*receding torus* model). Lastly, it is worth noting that the origin of the dusty torus is still unclear. Theories suggest that its formation involves gas and dust transported from the outer accretion disk, direct feeding of molecular gas from the host galaxy, and/or molecular clouds vertically outflowing from the outer accretion disk.

1.4.4 The Narrow Line Region (NLR)

The Narrow Line Region (NLR), differently from the BLR, exhibit narrow, but strong permitted as well as narrow forbidden lines of the order of ($FWHMs \sim 10^2\,\mathrm{km/s}$). In addition to that, it is important to notice that the narrow lines are much less time-variabile with respect to the lines of the BLR. The gas responsible for this emission is considered to be located in the so-called narrow line region (NLR) that can extend from $\sim 100\,\mathrm{pc}$ up to several kpc. The narrower widths and smaller velocities suggest the NLR is located farther from the BH than the BLR. Moreover, the lack of the time variability also indicates that the gas in the NLR is kinetically separated from the BLR.

1.4.5 The relativistic jets

A relativistic jet is an outflow of ionized plasma concentrated in a narrow beam (opening angle of a few degrees on kpc-scales). In particular, jets in AGN are char-

acterized by their highly collimated structure, relativistic propagation speeds (close to the speed of light), and non thermal particles distribution. These peculiar outflows can extend to kpc scales even though they are thought to be produced in the surrounding of the SMBH ($\approx 0.1\,\mathrm{pc}$) The jet emits radiation from radio to optical and X-ray wavelengths. Moreover, the jet, if it is strongly beamed (1.6.3), can produce photons even up to GeV and TeV energies by the inverse Compton scattering or by intrinsic hadronic processes within the jet (see 1.6). In the nearby Universe, jets are found in approximately 10 % of AGNs. This small fraction suggests that, even though, the jet formation requires certain conditions. Indeed, jets are found in AGNs with quite low Eddington ratios ($\frac{L}{L_{edd}} < 0.01$) and very massive central BHs. Low and high Eddington ratio AGNs differ for the geometry and physical properties of the accretion flows. Relativistic AGN jets contain large amount of kinetic energy and the jets can affect the interstellar medium in the surrounding environment. The interaction between the jet and the environment is commonly referred as **AGN feedback**. The AGN feedback can be used to solve some astrophysical issues that are hard to comprehend without taking into account the jets produced by AGNs. This is the case, for instance, of the cooling flow problem. This is an issue that involves the observed hot gas ($T \approx 10^{7-8}$ K) in the intracluster medium. This problem can be explained with the jets of AGNs in the centers of the galaxy clusters. The importance of mechanical AGN feedback through relativistic jet is also importantly recognized in galaxy formation in cosmological context.
One of the greatest issues in the AGN field regards the formation of the jets. A relativistic jet requires matter in the outer accretion disk to fall towards the vicinity of the central BH and to escape from the deep gravitational potential. Various models were suggested during the last decades. The best candidate is the magnetic field that emerges in astrophysical plasmas. Moreover, magnetic fields work efficiently, especially for rotating and turbulent plasma (like accretion flows near the BH). Currently, two most favored scenarios of jet launching involve the central SMBH (Blandford-Znajek) and the inner accretion disk (Blandford-Payne).
It is evident from observations that the collimated jets loose their kinetic energy in several different forms and there are several different processes that lead to termination of the pc-scale jet on larger scales. When interacting with the inter-galactic medium, the flow loses its energy and can produce (in the case of FRII) lobes on either side (**hot spots**). These hot spots are not the result of a single event, but are probably constantly fuelled by the jet.

1.5 The unified model

Urry & Padovani (1995) developed a "unified scheme model" in which the observed properties of AGNs are interpreted in terms of orientation of the LoS with respect to an astrophysiscal entity with non isotropic emission. The main criteria are the viewing angle θ, the Eddington ratio $l = L/L_{Edd}$ (where L_{edd} is the one of 1.1), and the radio loudness $R_{r,o}$ (1.3.1). The inclination determines the fraction of the AGN light from the central engine region which can be directly observed against torus obscuration. The Eddington ratio characterizes the mass accretion rate and geometry of the accretion flow. This geometrical model explains the differences among Type 1 AGN (those with broad lines in the optical spectrum, and substantial

UV and X-ray radiation) and Type 2 AGN (those with only narrow lines and little/no UV-Xrays) based on the line of sight. In the latter the l.o.s. crosses the molecular dusty torus which is optically thick to high energy radiation. An illustration of this model is shown in 1.4 where in addition AGN are divided in two main classes depending on the radio loudness.

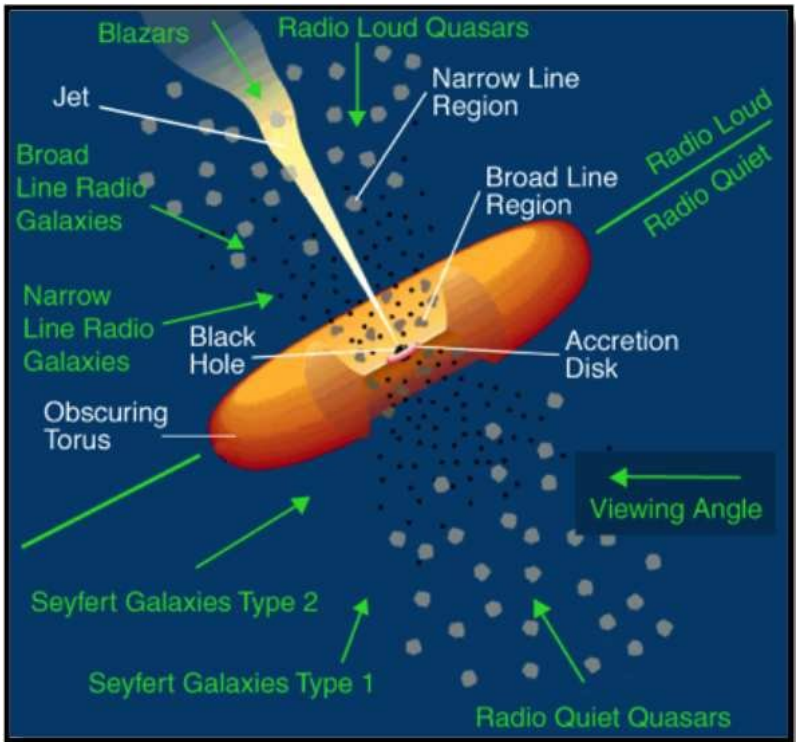

Figure 1.4: An artistic representation showing the main components of an AGN, along with the basic idea behind the unification schemes Urry & Padovani (1995). The white labels describe the different AGN components. The green labels note some of the different AGN types, and the arrows show the viewing angle. Image Credit: Raban D.

1.6 General properties of relativistic jets

Given the nature of the relativistic jets as collimated flows of plasma in a magnetic field, they are subject to different processes that will be explained in this section. The observations show that jets are not homogeneous, but have structures known as components with a more intense emission. These components are the nucleus, a compact and bright structure from which the jets are launched (thus it is also called base of the jet), and the emission regions along the jet, that can move with apparent superluminal motion 1.6.3. Moreover, it is possible to define the **core** that corresponds to the region in which the transition between optically thick and thin takes place.

1.6.1 Radiation processes

The emission of relativistic jets spans from radio waves to X-rays and even γ-rays. The main part of the radiation is generated through high-energy non-thermal processes, involving relativistic charged particles within strong photon and magnetic fields. According to observational evidence, the two main emission mechanisms are synchrotron, related to the magnetic field and inverse Compton (IC), related to the photon field.

Synchrotron radiation

When a charged particle is moving at a non-relativistic speed around a magnetic field, the particle is centrifugally accelerated by the field and gyrates with a specific period. A sinusoidal radiation is produced as a result. The radiation spectrum can be characterized by a well-defined single electromagnetic frequency. When the particle moves at a speed v comparable with the speed of light c (relativistic case), however, the resulting radiation is significantly beamed parallel to the particle velocity vector and the observed electromagnetic pulses result in a broader radiation spectrum. This is the mechanism producing the synchrotron radiation. It is important to define the Lorentz factor $\Gamma = (\sqrt{1-\beta^2})^{-1}$ (where $\beta = v/c$) that can be used as an indicator of the particle speed/energy.
In real AGN jets, the number density of particles usually follows a power-law energy distribution. The power-law particle energy distribution is generally produced as a result of particle acceleration in a shock. The number density of the non-thermal particles $n(\epsilon)$ per unit particle energy interval $[\epsilon, \epsilon + d\epsilon]$ can be expressed by:

$$n(\epsilon)d\epsilon \propto \epsilon^{-p}d\epsilon \tag{1.2}$$

where p is the particle spectral index. The synchrotron radiation spectrum $F(\nu)$ of an ensemble of electrons in the jet plasma for the optically thin case (i.e., no self-absorption), is given by:

$$F(\nu) \propto NH^{(p+1)/2}\nu^{-(p-1)/2} = NH^{1+\alpha}\nu^{-\alpha} \tag{1.3}$$

where N is the total number of particles, H is the magnetic field intensity and $\alpha = \frac{p-1}{2}$ is the **synchrotron radiation spectral index**. The total synchrotron power P (or energy loss rate) is given by:

$$P = -\left(\frac{dE}{dt}\right)_{sync} = \frac{4}{3}c\sigma_T\Gamma^2 U_H\beta^2 \tag{1.4}$$

where σ_T is the Thompson scattering cross-section, $U_H = \dfrac{H^2}{8\pi}$ is the magnetic energy density. From this equation, it is possible to see that more energetic electrons loose their energy faster than lower energies one, in the same magnetic field. The spectrum in the synchrotron self-absorbed (SSA) regime can be obtained by calculating an equivalent thermodynamic temperature T of relativistic electrons with the corresponding Γ ($T = \Gamma m_e c^2/k_B$ where m_e is the electron mass and k_B is the

Boltzmann's constant) and comparing it with the brightness temperature of a black body 1.6.2. Thus:

$$F(\nu) \propto \nu^{5/2} H^{-1/2} \tag{1.5}$$

The transition from the optically thick ($\tau_\nu > 1$) to thin ($\tau_\nu < 1$) regime occurs at a frequency ν_t called turn-over frequency, when the synchrotron opacity τ_ν is approximately equal to 1. The turn-over frequency can be estimated from the spectrum (Fig. 1.5) and it could provide a measure of the magnetic field, since:

$$\nu_t \approx F_t^{2/5} d^{-4/5} H_\perp^{1/5} (1+z)^{1/5} \tag{1.6}$$

where F_t is the flux density at the turn-over frequency, d is the source angular size, $H_\perp$ is the magnetic field component perpendicular to the l.o.s. and z is the redshift. Another way to estimate the magnetic field is based on the assumption that the source is in the state of minimum energy. This is called equipartion state and the associated magnetic field is called, indeed, **equipartition magnetic field** H_{eq}. The total energy of a synchrotron emitting body U must take into account both particles U_E and magnetic field U_H. The energy associated with the relativistic particles (electrons) radiating synchrotron emission can be calculated as $U_e = C_e H^{-3/2} L$, where C_e is a constant, H is the magnetic field intensity and L is the luminosity of the source. On the assumption that the protons emits the same energy as the electrons, it is possible to write U_E as $U_E = (1+k)U_e$ where k indicates the total energy of protons with respect to electrons. The energy stored in the magnetic field can be written as $U_H = C_H H^2 V$, where C_H is a constant and V is the volume of the source. Therefore it is possible to write the total energy budget :

$$U = U_E + U_H = (1+k) C_e H^{-3/2} L + C_H H^2 V \tag{1.7}$$

By deriving the Eq. 1.7 with respect to the magnetic field, it is possible to found the minimum energy (Fig. 1.5), that corresponds to $(1+k)U_e = \frac{4}{3} U_H$. Thus, the magnetic field calculated in the minimum energy state (equipartition) is:

$$H_{eq} = \left[\frac{3}{4} (1+k) \frac{C_e}{C_H} \right]^{\frac{2}{7}} \left[\frac{L}{V} \right]^{\frac{2}{7}} \tag{1.8}$$

This can be calculated from observations, although a number of assumptions are hidden. For instance, the particle density is assumed to be homogeneous and the magnetic field is supposed to be uniform all over the relativistic plasma. Despite all the assumptions, the equipartition magnetic field, has been found out to be a good estimate of the actual magnetic field[1] for a good number of radio sources.

Inverse Compton

The Inverse Compton emission (IC) occurs when a photon with energy $E_{ph} = h\nu$ interacts with an electron with rest mass $E_0 = m_e c^2$ that moves at highly relativistic velocity. If $E_{ph} \ll E_0$ the electron loses some of its kinetic energy by transferring it

[1] Orienti & Dallacasa (2008)

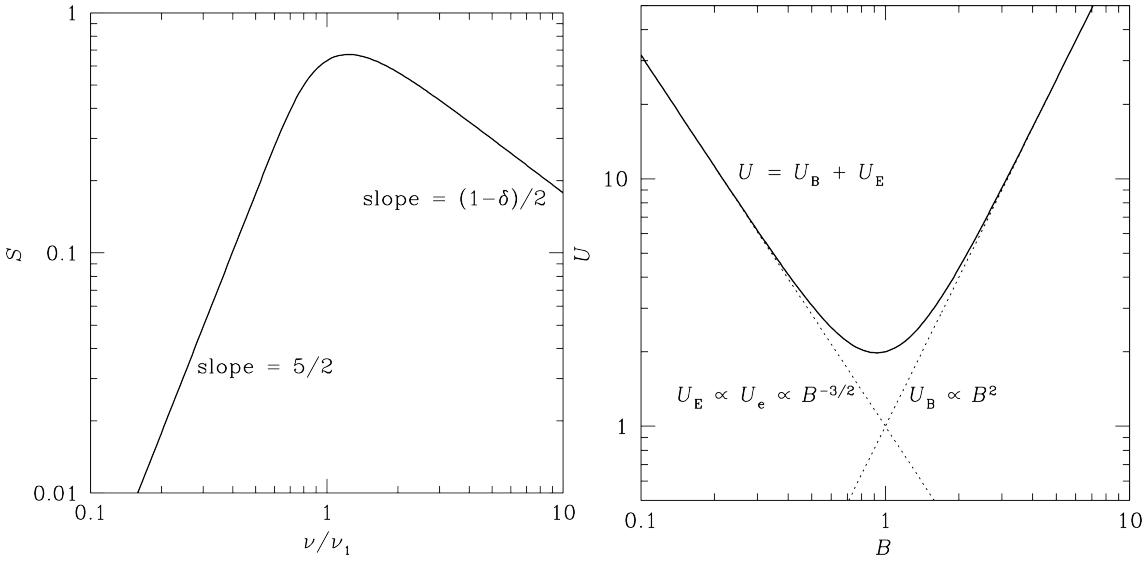

Figure 1.5: **Left**: A mock synchrotron spectrum with self absorbtion (SSA). The plot is in logaritmic scale. S is the flux density, ν is the frequency, δ is the particle spectral index, ν_t is the turn-over frequency and the slope represent the exponent of the frequency. For $\nu < \nu_t$, there is self absorption. Image Credit: Essential Radio Astronomy, NRAO. **Right**: The energetic of a radio source. U_E is the particle energy density, B is the magnetic field, U_B is the magnetic energy density and $U = U_E + U_B$ is the total energy. Image Credit: Essential Radio Astronomy, NRAO.

to the scattered photon, that gains energy. The energy loss rate of IC radiation is really similar to the synchrotron rate ((1.4)):

$$P = -\left(\frac{dE}{dt}\right)_{IC} = \frac{4}{3} c \sigma_T \Gamma^2 U_{ph} \beta^2 \tag{1.9}$$

where U_{ph} is the photon energy density. The relationship between the incident and the up-scattered photon goes as $\nu \approx \Gamma^2 \nu_0$. Therefore, inverse Compton can change infrared/optical photons into X-ray/γ-ray radiation assuming a sufficiently high Lorentz factor. An interesting case is the one in which photons interact with the same relativistic electrons in the jet plasma, which originally produced them via synchrotron emission. These electrons increase the energy of the photon field via IC scattering. The process is called **Synchrotron Self-Compton** (SSC) and may be an important factor in explaining the high-energy emission of AGN such as blazars. By comparing the energy loss rates of synchrotron (1.4) and IC (1.9), it can be seen that:

$$\frac{(dE/dt)_{sync}}{(dE/dt)_{IC}} = \frac{U_H}{U_{ph}} \tag{1.10}$$

In this case, it can be estimated the magnetic flux density if it is possible to determine the synchrotron and IC energy loss rates through observations.

1.6.2 Brightness Temperature

The surface brightness of synchrotron radiation in AGN jets can also represented by the **brightness temperature**. The brightness temperature T_B of a radiation in

the radio frequencies is defined by:

$$T_B = \frac{c^2 I(\nu)}{2k_B \nu^2} \tag{1.11}$$

where $I(\nu)$ is the intensity, k_B is the Boltzmann constant, and ν is the observing frequency. This definition is originated from the Rayleigh-Jeans law since photons in the radio bands have typically much lower energies than the particle ($h\nu/k_B T \ll 1$ with h Planck constant). For thermal radiation, T_B provides a good estimation of the true gas temperature. For non-thermal radiation such as synchrotron radiation in AGN jets, however, the brightness temperature, does not correspond to the physical thermodynamic temperature of the particle energy distribution. This is simply because the particle energies are not Maxwellian distributed, but, as shown in 1.6.1, they are in the form of a power law. Nevertheless, the brightness temperature indicates the temperature that a black body should have in order to emit $I(\nu)$. In addition to that, in the case of SSA, it can be demonstrated that:

$$\frac{L_{IC}}{L_{sync}} \approx \left(\frac{T_{B,max}}{10^{12}\ \mathrm{K}}\right)^5 \left(\frac{\nu}{\mathrm{GHz}}\right) f(\alpha) \tag{1.12}$$

where L_{IC} and L_{sync} represent the luminosity of IC and synchrotron emission, respectively and $f(\alpha)$ is a function that depends from the spectral index. For brightness temperatures above 10^{12} K , the radiation field has undergone to a dramatic amplifcation. IC would become the most effcient and dominant cooling process and a source would radiate its energy in a very short time. This is called the **Compton catastrophe**. Therefore, the brightness temperature limit for a radio source is $T_{B,max} \approx 10^{12}$ K. In some astrophysical cases, however, the observed T_B seems to exceed this limit. This problem can be explained through the Doppler boosting 1.6.3.

1.6.3 Doppler boosting

The study of a source, such as a jet, in motion with respect to the observer frame requires to consider some relevant geometric properties. More specifically, since the jet has a velocity v_j that is close to the speed of light c, it is necessary to take into account the relativistic effects that affects the observations. Because of the special relativistic time dilation and length contraction, the isotropic radiation in the jet frame appears anisotropic in the observer's frame. The radiation is therefore preferentially beamed along the moving direction and focused within a critical angle $\theta_{crit} \approx 1/\Gamma$, where Γ is the Lorentz factor. It is possible to define the Doppler factor δ as:

$$\delta = \frac{1}{\Gamma(1 - \beta \cos\theta)} \tag{1.13}$$

where θ is the angle between the moving direction and the line of sight. It can be demonstrated that δ affects some physical quantities in the observer frame:

$$F(\nu) = F'(\nu)\delta^{3+\alpha}\ ;\ T_B = T_B^{'}\delta \tag{1.14}$$

where $F(\nu)$ is the observed flux, α is the spectral index, T_B is the brightness temperature and the apex $'$ indicates quantities measured in the jet rest frame. Since the

jets are ejected in a symmetrical way with respect to the SMBH, the approaching jet is boosted, while the receding one is dimmed. Therefore, their flux densities are going to be Doppler boosted or de-boosted by a factor $\delta^{3+\alpha}$ and the Doppler factors are:

$$\delta_a = \frac{1}{\Gamma(1-\beta\cos\theta)} \; ; \; \delta_r = \frac{1}{\Gamma(1+\beta\cos\theta)} \tag{1.15}$$

where the subscripts a and r represent the approaching and receding jet respectively. Thus, the ratio between their observed flux density F is:

$$\frac{F_a}{F_r} = \left(\frac{1+\beta\cos\theta}{1-\beta\cos\theta}\right)^{3+\alpha} \tag{1.16}$$

Depending on the intrinsic speed and the viewing angle, the de-boosting can be very large. This explains why most of relativistic jets with fast speed appear to be one-sided.

Superluminal motion

The superluminal motion represents the case in which the velocity of an object seems to exceed the speed of light (hence, disproving the theory of relativity). The reason of this is that the object (the jet) is moving close to c in a direction close to the line of sight to the observer. To arrive to such conclusion, it is possible to consider a certain component travelling within the jet at a speed v, very close to c (Fig. 1.6). It emits two light pulses at two different times, separated by a time interval Δt. In this period of time, the first pulse going towards the observer, travels a distance $c\Delta t$. The component keeps advancing within the jet at velocities close to the light speed, so at the time the second light pulse is emitted, it has travelled the projected distance in the observer direction: $v\Delta t\cos(\theta)$, where θ is the angle between the velocity vector and the line of sight. The second pulse travels a shorter distance before reaching the observer: $c\Delta t - v\Delta t\cos(\theta)$, meaning that the time difference between the pulses in the reference frame of the observer, can be expressed as $(c\Delta t - v\Delta t\cos(\theta))/c$. The ratio between the component's path projected along the observer plane and the arrival time difference of both pulses yields the apparent speed (β_{app}) for the observer, and the one measured.

$$\beta_{app} = \frac{\beta\sin(\theta)}{1-\beta\cos(\theta)} \tag{1.17}$$

With β close to 1 and θ close to 0, the apparent velocity projected on the plane of the sky can exceed c.

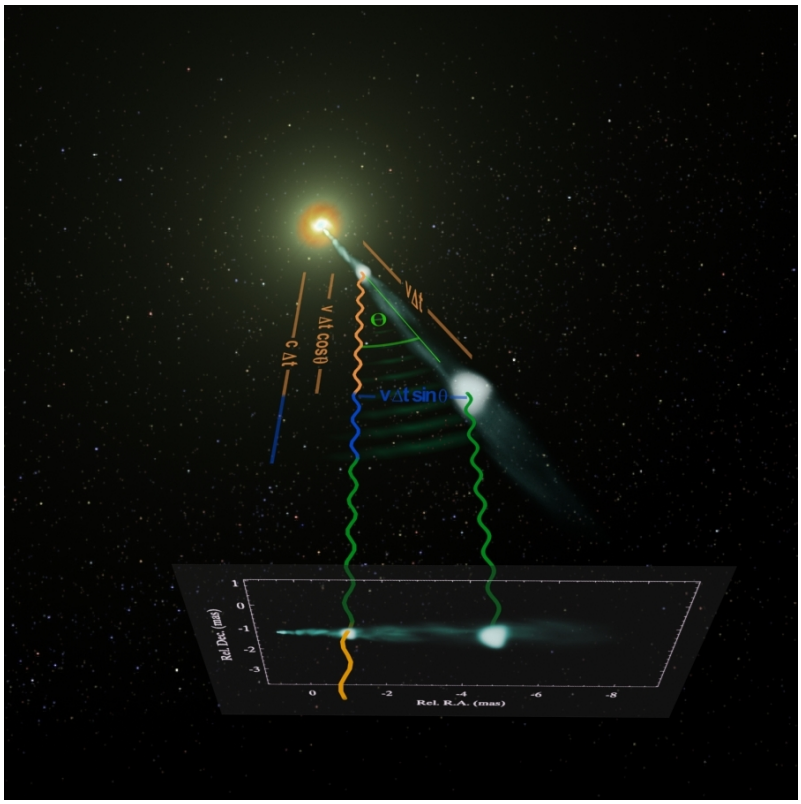

Figure 1.6: Representation of superluminal motion. Image Credit: Steffen W. & Gómez J. L.

1.7 The SED of the AGN

In general, AGN emission can be detected in many if no all the observing windows. Orientation may play role in enhancing/depressing some of the emitting regions, providing different flavours of the Spectral Energy Distribution (Fig 1.7). Hereafter those aspects related to the non-thermal emission in the jet, will be mainly consider.

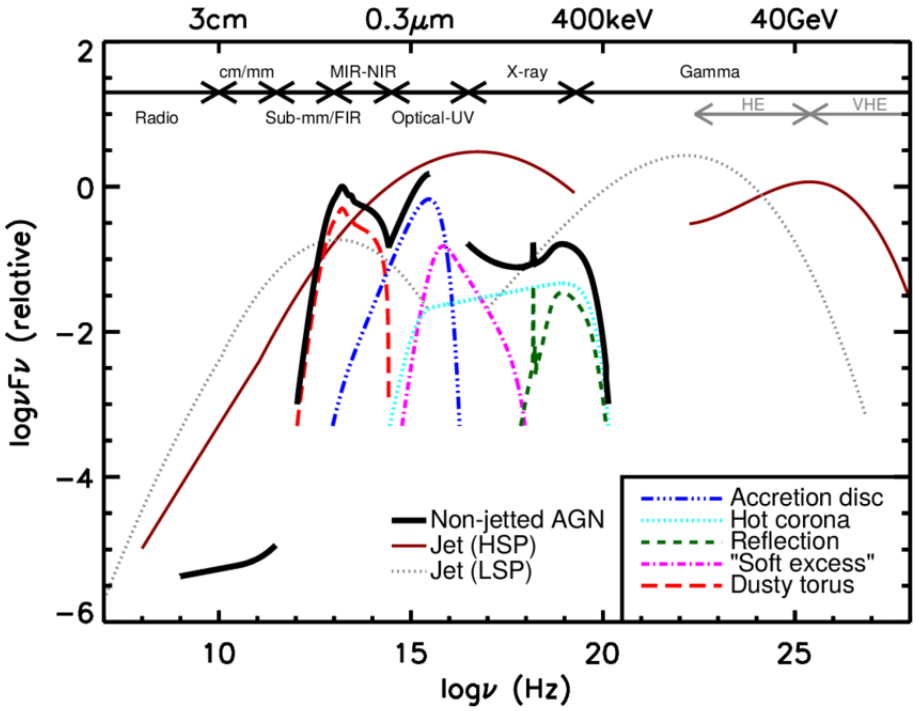

Figure 1.7: A schematic representation of an AGN spectral energy distribution (SED). The black solid curve represents the total emission and the various coloured curves (shifted down for clarity) represent the individual components. Image Credit: C. M. Harrison.

For what concerns the **radio** domain, as explained in the section 1.6.1, the emission of the AGN is non-thermal and is mainly produced by the synchrotron process in the jet.
The **infra-red** band, is dominated by the reprocessing of the radiation from the dusty torus with a peak, typically at $\sim 10-20$ μm. In addition to that, at ~ 1.6 μm and ~ 100 μm there could be other peaks that are caused by the stellar emission of old stars and by the dust present in the host galaxy. Therefore, since these components are added to the torus emission, it is not easy to distinguish between them and this leads to a difficult characterization of the torus. For the RLAGN, it could be present also a non-thermal emission due to the synchrotron radiation that has its peak at higher frequencies.
The **optical** part of the SED is characterized by a big bump in the form of the so-called *Big Blue Bump* in the range $\sim 300-3000$ Å. This bump can be understood as follows. Near the BH, the rotation velocity of accretion flow becomes very high and the viscosity effect is also strong. This makes the gas temperature high ($\gtrsim 10^4$ K) and the exact flow temperature depends on the distance from the BH. Given that

the accretion disk is optically thick, the emission spectrum of a local region in the disk can be approximated by that of a black body with the disk temperature. The sum of the black body spectra with different disk temperature gives rise to the excess ultraviolet emission from the entire accretion disk. Similarly, the SEDs of accretion disks can be decomposed into several black body spectra that emit at a given temperature. Moreover, it is possible to notice the presence of narrow lines from the NLR, that can be used as indicator of the intrinsic emission of the AGN or broad lines from the BLR that can be used to constrain the SMBH mass.
The **X-ray** emission is characterized by different components that can or cannot be present based on the orientation of the AGN. The main emission is produced by the IC between the relativistic electrons of the Hot Corona and the photons from the accretion disk. The reflected component generates a bell shape called *Compton Hump*. This emission can produce photons up to hundreds of keV. Moreover, there is an excess in the energy range $\sim 0.1 - 1$ keV, called *soft excess* that is still under debate. It could be the tail of the big blue bump or the direct emission from the Hot Corona. At slightly higher energies it is possible to notice an absorption that is associated with a clumpy gas further out from the core with respect to the hot corona called *warm absorber*, that could correspond to the BLR. As already mentioned in the 1.4.1, the Hot Corona could also produce the Fe line at 6.4 keV. The iron line can be used to estimate various parameters such as the distance between the disk and the SMBH or its spin.
Lastly, the AGN can produce also emission in the γ**-ray** domain. Usually, this emission is present in Blazar since the jet is on the line of sight and therefore the Doppler boosting strongly amplifies the radiation, up to very high energies (~ 100 MeV $- 10$ TeV). This emission is caused by the IC process described in the Sect. 1.6.1.

1.8 Main aim of this thesis

This introduction has tried to emphasize the importance of jet and outflows in AGNs that has been recognized in various astrophysical contexts over the last decades. The main aim of this work is to provide better observational constraints on the theories of relativistic jets. This is done through the analysis of high-resolution multi-frequencies VLBA observations of the radio source 3C111. More specifically, through the study of polarized emission this work will try to estimate the magnetic field in different parts of the jet. As outlined above, such information is key to better characterize the nature and emission processes of relativistic outflows. The source studied throughout the thesis, as will be described in the Sect.3.1, is an FR II radio galaxy containing two radio lobes and a one-sided jet. 3C111 has a remarkable jet, beautiful to the eye and rich in physical terms and it has been at the center of various studies in the past years (p.e. Schulz et al. (2020), Schulz (2012) or Beuchert et al. (2018)) In this study, for the first time, the analysis of the source spans across 6 different radio bands observed simultaneously. Among these the 15 GHz one is part of the MOJAVE program Lister (2018). Moreover the 86 GHz image is the highest resolution map ever produced with the VLBA, for 3C111. As will be described throughout the thesis, various analysis has been performed in order to get a number of images and to provide relations between numerous physical quantities.

Chapter 2

Radio interferometry and VLBA observations

The Earth atmosphere is transparent to electromagnetic waves in the radio band ($\sim 0.01 - 1000$ GHz), as shown in the figure 2.1. This feature is typical only of radio and optical wavelengths. The similarity between these bands can be seen also in the way telescopes are built.
At difference with respect to optical telescopes, in the radio, the instrumentation works at the diffraction limit. However, one of the biggest problems in radio astronomy is the angular resolution (θ_{res}) that is given by the formula: $\theta_{res} \sim \lambda/D$, where λ is the wavelength at which the observation is performed and D is the diameter of the antenna. Since in the radio band, the wavelengths spans from ~ 0.3 mm at 1 THz to ~ 30 m at 10 MHz, to have a resolution of a few arcsec at 1.4 GHz, the diameter of the antenna should be of a few kilometers. The antennas can not be larger than ~ 100 m due to engineering problems, so in order to have a better resolution, a different approach is needed. Moreover, the great range of frequencies covered by the radio band, involves the use of a variety of observation techniques.

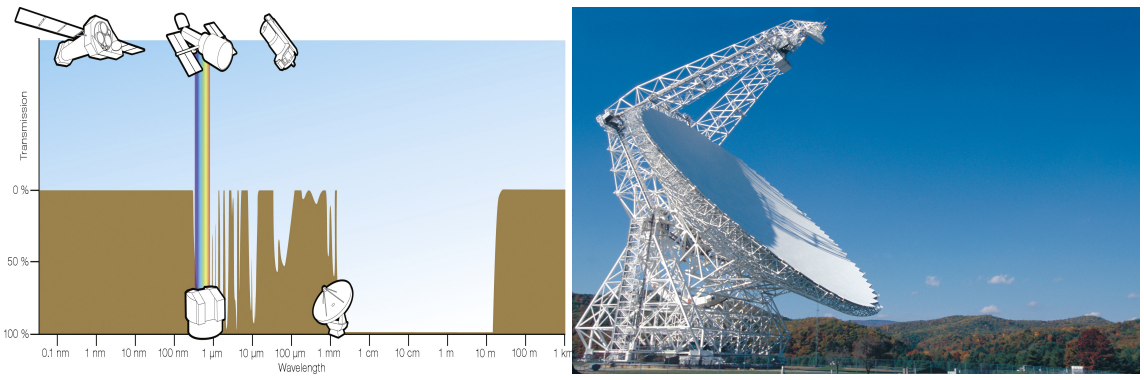

Figure 2.1: **Left:** Atmospheric transmission versus wavelength. Only the radio and the visual bands do not present absorption, thus it is possible to perform ground based observations. Image Credit: ESA/Hubble. **Right:** The 100m Green Bank Telescope (GBT) in West Virginia. Image Credit: NRAO/AUI/NSF.

2.1 Single dish

Single dish antennas have a structure which is grossly similar to optical telescopes. The mirror (reflecting surface) collects a very weak radio signal which needs to be amplified in the receiving system. Each telescope has a specific beam pattern, namely the directional sensitivity. The main lobe (figure 2.2) defines the resolution, measured as the Half Power Beam Width (HPBW), while some additional power is collected via the (secondary) sidelobes.

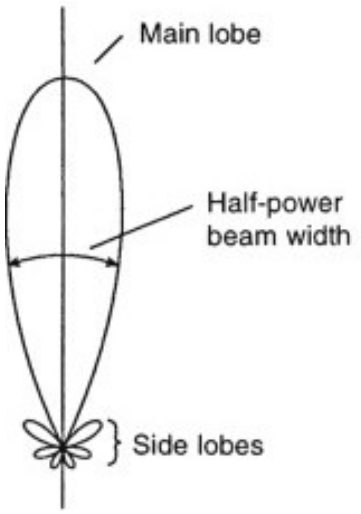

Figure 2.2: A generic antenna pattern with the main lobe and the sidelobes. The half power beam width (HPBW) is also represented. Image Credit: J. D. Kraus

The beam size θ is inversely proportional to the diameter of the aperture D and proportional to the observing wavelength $\theta = a \times \lambda/D$. The constant a is nearly unity and varies depending on the detailed aperture geometry. The mirror has a characteristic surface rms. All the radiation with $\lambda > 20rms$ is perfectly reflected. Such rms defines the minimum λ at which the telescope can effectively work. The efficiency dramatically drops at $\lambda/4$. A large dish means a large collecting area and so a high sensitivity S, since it is proportional to the square of the collecting area $S \propto D^2$. However, large telescopes like GBT or Effelsberg, are extremely costly and difficult to operate.
Each telescope needs a set of receivers where the incoming electromagnetic signal is sampled and detected. In fact, electromagnetic waves can be decomposed into any set of two orthogonal polarizations (e.g., vertical/horizontal or left/right circular vectors). If the receivers are circular, they are called *feed horns* and they decompose the incoming polarization in Right Circular Polarization (RCP) and Left Circular Polarization (LCP). On the other hand, if the receivers are linear, they are called *dipoles* and they decompose the incoming polarization in x and y.

2.1.1 Data acquisition and processing

The procedures of data acquisition and processing can typically be summarised in the following steps:

1. The receivers, that are usually two orthogonal dipoles, convert incoming electromagnetic waves into electrical voltages with a phase and an amplitude.

2. The raw signals from astronomical sources are very weak compared to laboratory voltages. Therefore, the frequency down-converted data are amplified by standard digital/analog signal processing instruments. On the other hand, the amplification generates additional noises from the individual amplifiers.

3. An autocorrelation spectrometer (or simply correlator) is used to digitize and obtain the final source spectrum by Fourier transform. For interferometers, the auto correlator is replaced by the cross correlator.

2.1.2 System Temperature and SNR

For a radio telescope, it is convenient to represent the source brightness in Kelvin rather than in Jansky (1 Jy $= 10^{26}$ $\mathrm{Wm^{-2}Hz^{-1}} = 10^{23}\,\mathrm{ergs^{-1}cm^{-2}Hz^{-1}}$) because engineers used this notation. For a source with flux density S_{sou}, the following equation applies:

$$S_{sou} = G \times \frac{T_{ant}}{T_{sys}} \times T_{sys} = G \times \frac{C_{ant}}{C_{sys}} \times T_{sys} \tag{2.1}$$

where G is the characteristic Kelvin-to-Jansky conversion factor of the system (*antenna gain*); T_{ant} is the increase in the receiver temperature due to the source; T_{sys} is the system temperature and C_{ant} and C_{sys} are uncalibrated counts for the source and the system in arbitrary system count units. The antenna gain G can be well determined by observing a flux calibrator with known flux density. The system count C_{sys} can be obtained by flux measurements with closed shutter. Since the count towards the source is $C_{ant} + C_{sys}$, the source count can be obtained. The system temperature T_{sys} is the sum of the temperatures of all components that cause noise.

$$T_{sys} = T_{ant} + T_R + (1 - e^{-\tau})T_{atm} + T_{spill} + T_{bkg} + ... \tag{2.2}$$

where T_R is the receiver temperature; $(1 - e^{-\tau})T_{atm}$ is due to the atmosphere where τ is the opacity of the atmosphere and T_{atm} is the atmospheric temperature; T_{spill} accounts for spillover radiation that the feed picks up; T_{bkg} is the average sky brightness temperature contributed by all background radio sources and ... represent all other minor noise effects. Typically, the system noise temperature is written as follow:

$$T_{sys} = T_{ant} + T_{rec} + (1 - e^{-\tau})T_{atm} \tag{2.3}$$

and T_{rec} is related to the receiver noises (such as T_R and T_{spill}). Typically, T_{rec} is known a-priori from lab measurements, T_{atm} and T_{ant} can be directly measured from the observatory site and the opacity term is usually solved by assuming a plane-parallel model for the atmosphere.
Astronomical sources are faint and the blank sky counts also fluctuate with time. Therefore, one needs to know the signal-to-noise ratio (SNR) of the observation. It can be demonstrated that the rms error of the receiver output σ_T, can be written as:

$$\sigma_T = \frac{T_{sys} + T_{ant}}{\sqrt{\Delta\nu\Delta t}} \xrightarrow{T_{ant} \ll T_{sys}} \sigma_T \sim \frac{T_{sys}}{\sqrt{\Delta\nu\Delta t}} \tag{2.4}$$

where $\Delta\nu$ is the bandwidth of the observation and Δt is the integration time. It can be found that $T_{ant} \ll T_{rec}$ is true also for larger telescopes, even though their gain (and so their T_{ant}) are bigger. Therefore, the SNR is the increase in the temperature produced by the source divided by σ_T, times a constant that depends on the system design C:

$$SNR = C \times \frac{T_{ant}}{T_{sys}} \sqrt{\Delta\nu \Delta t} \tag{2.5}$$

2.2 Interferometry

As discussed in the previous sections, one of the main problems of radio observations is the poor angular resolution of the telescopes. The resolution can be significantly improved with a technique called **Radio Interferometry** or aperture synthesis. This technique consists in the creation of arrays of physically separated telescopes that are electronically connected. The distance b between two antennas is called **baseline**. The angular resolution θ_{res} of a system of two electronically connected telescopes, in the baseline direction, for a radiation wavelength λ is:

$$\theta_{res} \approx \frac{\lambda}{b} \tag{2.6}$$

The signals received by different elements of the array have to be combined coherently. As shown in figure 2.3, this can be done considering the geometric delay τ_g between the antennas receiving the same signal. The received waves can be considered as plane and parallel (*far field* assumption). The output voltages of the two antennas are $V_1 = V\cos[2\pi\omega(t-\tau_g)]$ and $V_2 = V\cos(2\pi\omega t)$, where V is the amplitude of the radiation and $2\pi\omega$ is the angular frequency of the radiation. These two are correlated (multiplied and time averaged) in order to obtain the synthetic response of the two telescopes R_C:

$$R_C = P\cos(2\pi\omega\tau_g) = P\cos(2\pi\frac{\vec{b}\cdot\hat{s}}{\lambda}) = P\cos(2\pi ul) \tag{2.7}$$

Where P is a constant for the amplitude, $\vec{b}$ is the baseline vector, $\hat{s}$ is the versor in the source direction, λ is the wavelength of the radiation, u is the baseline length normalized by the wavelength, θ is rge angle between $\vec{b}$ and the incoming radiation and l is cosine of θ. The cosinusoids $\cos(2\pi ul)$ are called **fringes**. The term $\phi = 2\pi ul$ is the **phase** of the fringes.

The synthesized response of the telescopes in the Fourier space (the counterpart of the projected sky plane), is called **visibility** V. Every antenna samples V in the two polarization and so it produces two data streams.

2.2.1 (u, v) plane and visibilities

It is needed to discuss the Fourier transform and the Fourier space, in order to describe the principles of the interferometry. As known, the Fourier transform (FT) of a function $f(x)$ is defined as:

$$F(s) = \int_{-\infty}^{+\infty} f(x)e^{-i2\pi xs}dx \tag{2.8}$$

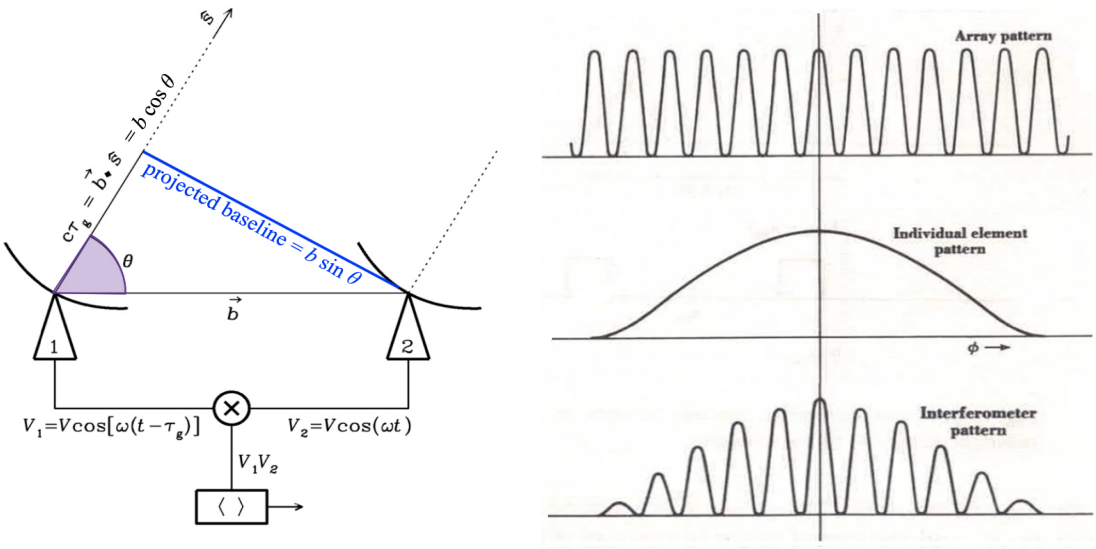

Figure 2.3: On the left: A schematic representation of an interferometer composed by 2 antennas. τ_g is the geometric delay; θ is the angle between the baseline vector $\vec{b}$ and the incident radiation direction vector $\hat{s}$; V_1 and V_2 are the output voltage of the antennas. Image Credit: Essential Radio Astronomy, NRAO. On the right: Starting from the top it is represented the FT of the double pulse function (the response of the 2 elements array), the FT of the rectangle function (the response of the single antennas) and the response of the interferometer. Image Credit: Gitti M., Unibo.

While the Fourier antitrasform (FT^{-1}) is defined as:

$$f(x) = \int_{-\infty}^{+\infty} F(s) e^{i2\pi xs} ds \tag{2.9}$$

In addition to that, it can be defined the operation of convolution between the functions f and g:

$$fg = \int_{-\infty}^{+\infty} f(u) g(x-u) du \tag{2.10}$$

It can be demonstrated that the FT of a convolution is equal to the product of the FT of the two functions. So, in the Fourier space, the convolution is just a multiplication (*Convolution theorem*). The observations are the sky brightness distribution convolved with the beam pattern. The function that approximately describes the single antenna aperture in 1D is the rectangle function (in the ideal case, is the δ_{Dirac}) and its FT is the *sinc* function. If two (pointlike) apertures are considered, their total response is a double pulse function, whose FT is a Cosine. So, in order to obtain the response of the interferometer, it is necessary to convolve the rectangle function with the double pulse function. In the Fourier space this is just the product between the cos and the $sinc^2$ function. Therefore, the resultant response of the interferometer is a cosine modulated by a $sinc^2$ as shown in figure 2.3.
In order to improve the response of an interferometer, it is possible to add antennas. A multi-element interferometer with N antennas will have $\frac{N(N-1)}{2}$ combinations

of baselines. The combined pattern of all the antennas is called **dirty beam** and is the response of the interforemeter to a point source. In addition to that, looking back at the equation 2.6, it can be seen that the angular resolution varies with the inverse of the baseline length (or, more correctly with the projected baseline $b \sin\theta$) and this corresponds to the spacing in the cosine function. Longer baselines are sensible to compact objects while shorter ones are sensible to extended sources. Since the minimum baseline is, at most, equal to the diameter of the antenna, isotropic sources like CMB are not samoled by the interferometer. This is called the *missing short spacings* problem.
For extended sources, it is possible to consider the response of the interferometer as the sum of the response to point-like sources. In order to do that, it is needed to integrate the equation 2.7 over the solid angle towards $\hat{s}$ and change the constant P to the source brightness $I(\hat{s})$. It is useful to express the response of the correlator in an odd $R_{C,O}$ and an even $R_{C,E}$ part:

$$\begin{aligned} R_{C,O} &= \int\int I(\hat{s}) \cos(2\pi \frac{\vec{b}\cdot\hat{s}}{\lambda}) d\Omega \\ R_{C,E} &= \int\int I(\hat{s}) \sin(2\pi \frac{\vec{b}\cdot\hat{s}}{\lambda}) d\Omega \end{aligned} \tag{2.11}$$

It is now possible to define the **complex visibility function** by treating the sinusoidal functions as complex exponential $e^{i\phi} = \cos\phi + i\sin\phi$:

$$\mathcal{V} = R_c - iR_s = Ae^{i\phi} = \int\int I(\hat{s}) exp(-i2\pi\vec{b}\cdot\hat{s}/\lambda) d\Omega \tag{2.12}$$

Where $A = (R_c^2 + R_s^2)^1/2$ is the amplitude visibility, i is the imaginary unit and $\phi = \tan^{-1}(R_s/R_c)$ is the phase.
In order to obtain a more practical expression of the visibility function 2.12, a new coordinate system is required. Therefore, the directional vector can be written as $\hat{s} = (x, y, z)$ and it is defined with respect to a reference direction $\hat{s_0}$, called the *phase center* (i.e. the direction where the telescopes point to). The baseline vector, on the other hand, can be written as $\vec{b} = (u, v, w)$, where u, v and w are measured in units of λ. This new coordinate system forms the (u, v) **plane** that is the Fourier plane and can be interpreted as how the source "sees" the pairs of the interferometer while w is the normal to the plane and represent the source direction versor in the (u, v) plane (Fig 2.4). By applying the coordinate change to the 2.12, it can be seen that, for $\vec{s}$ close to the phase center, the visibility function and the intensity distribution can be written as follow:

$$\mathcal{V}(u, v) = \int\int I_\nu(x, y) exp[-2\pi(ux + vy)] dxdy \tag{2.13}$$

$$I_\nu(x, y) = \int\int \mathcal{V}(u, v) exp[+2\pi(ux + vy)] dudv \tag{2.14}$$

Thus, one of the most important piece of information related to the interferometry technique can be extrapolated: the *Van Cittert-Zernike theorem.* **For any interferometer, the sky intensity distribution $I_\nu(x, y)$ is obtained by the inverse Fourier transform of the visibility function $\mathcal{V}(u, v)$.** The interferometer samples the visibility function that is the FT of the sky brightness distribution $B(\theta, \phi)$.

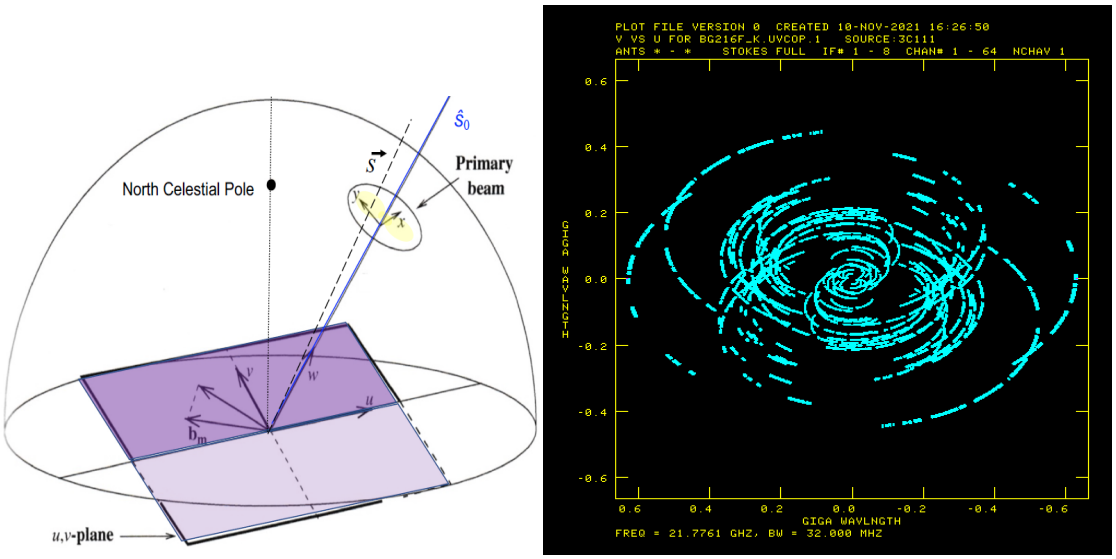

Figure 2.4: **Left**: A schematic representation of the (u, v) plane. $\vec{S}$ represent the directional vector, $\hat{S}_0$ the phase center, x and y the new sky coordinates and u, v, w the new baseline coordinates. Image Credit: Bai, Xuening; Princeton University. **Right**: An example of the UV coverage taken from the BG216F project of the MOJAVE program (the one analysed in this thesis). The image shows the distribution of the visibility in the (u, v) plane for the K band (21 GHz) throughout all the observation. Image Credit: this work.

The latter is obtained with the FT^{-1} of the $\mathcal{V}$ (e.g. deconvolving and convolving). A dense sampling of the visibility function is ideal to obtain a great representation of the B. Each interferometer of N antennas, instantly produce $N(N-1)/2$ samplings. The Earth rotation constantly modifies the baselines. This produces tracks (ellipses) in the (u, v) plane where the $\mathcal{V}$ is sampled (*Earth rotation synthesis*). The distribution of the visibilities in the (u, v) plane is called *UV coverage* (Fig. 2.4).

2.2.2 Calibration and imaging

As previously stated, the interferometric technique provides a clear upgrade in the radio observations. This is done at the expense of a more complex data reduction, with respect to the single dish. For the interferometer, as for the single dish, the visibilities are corrupted by the instrumentation and the atmosphere and need to be corrected. The calibration is done in order to obtain the real flux density and phase of the source. To this aim, a *primary calibrator* is observed: it is a source with known flux density, constant in time, and point-like for the instrument (i,e, model brightness as a delta, whose FT is constant, namely the same flux density on all baselines). It is usually observed at the beginning or at the end of the observation. For what concerns the phase calibrator (or *secondary calibrator*), instead, a source spatially near to the target is needed. The secondary calibrator is needed in order to get a model of how the phases are affected from the atmosphere. Since the phase corruptions varies very quickly, the phase calibrator is observed alternately with the target.
The complex visibility V_{ij}^{obs} is equal to the real visibility V_{ij}^{true} multiplied by complex

gain factors G_i , G_j that describe the response of the antennas i and j:

$$V_{ij}^{obs} = V_{ij}^{true} G_i G_j \tag{2.15}$$

The complex gain G can be divided in two parts: the amplitude a and the phase θ. This allows to write the equation 2.15 as follows:

$$A_{ij}^{obs} e^{i\theta_{ij}^{obs}} = A_{ij}^{true} a_i a_j e^{i(\theta_i - \theta_j + \theta_{ij}^{true})} \tag{2.16}$$

where A_{ij}^{obs} is the observed amplitude, A_{ij}^{true} is the true amplitude of the source, θ_{ij}^{obs} is the observed phase and θ_{ij}^{true} is the true phase of the source. These relations are based on the assumption that the gains are factorizable over the single antennas (i), (j) and polarization. The corrections can be applied by multiplying the factors (in the case of the amplitudes A) or by summing them (for the phases θ).
The different issues that can affect the observation of the target, are treated separately and each one of them has its own contribution to the gain. Therefore, the process of calibration is performed with the data from the calibrator and then only the final gain is applied to the source.
Once the calibration has been performed, it is possible to produce the images. This is done through a process called *imaging*. As can be seen in Fig. 2.2 the beam pattern is maximized at the center but it also has positive and negative responses around the peak (i.e. the sidelobes). For sources with complex structure, this can be an issue since they are convolved with the true visibility function and this can produce artifacts. This convolved map is the direct Fourier transform of the sampled visibility function and it is called **dirty map**. Therefore, in order to produce the true brightness maps, a careful deconvolution process is needed. Before going deep in the deconvolution algorithm, it is advisable to present the basic steps of the imaging:

- Computing the *sampling function* III; this function is the (u, v) coverage and it is calculated by putting a mask to the sampled visibility. This mask assigns a value of 1 (actually, it gives a value of 1 to the amplitude and 0 to the phase) to the points in the (u, v) plane that have data, and 0 where there are no data. In the Fourier space, the convolution between III (the Sha function) and the continuous visibility function V_t, gives in output the sampled visibilities function V_s, that represent the actual data that comes after the calibration process. $III * V_t = V_s$

- Obtaining the *dirty beam* DB; the dirty beam is the interferometric response to a point-like source i.e. the beam pattern. This is calculated by doing the Fourier anti-trasform of the sampling function III. $DB = FT^{-1}(III)$

- Producing the *dirty map* I_d; the convolution between the dirty beam and the true brightness function I_t, is called dirty map. This is calculated by doing the Fourier anti-trasform of the sampled visibility function V_s. $I_d = FT^{-1}(V_s)$

- Deconvolving the dirty map; by summing all the previous points and by using the Eq. 2.10 it is possible to see that:

$$\mathbf{I_d} = FT^{-1}(V_s) = FT^{-1}(V_t * III) = FT^{-1}(V_t) \times FT^{-1}(III) = \mathbf{I_t} * \mathbf{DB} \quad (2.17)$$

  where the $*$ indicates a convolution and $\times$ a multiplication. From the above equations, it can be seen that, in order to have the true brightness function, it is needed to deconvolve the dirty map. The final image is then produced by convolving the $\mathbf{I_t}$ with the clean beam (e.g. a fitted elliptical Gaussian function with the center of the dirty beam).

One of the most popular deconvolution algorithms is the *cleaning*. The basic idea is to model a continuous intensity distribution as the sum of many discrete components. The cleaning process works as follows:

1. Locate the peak position in the dirty map (x, y). This is the delta component that is stored in a table.
2. Convolve the delta component with the dirty beam.
3. Subtract the delta component convolved with the dirty beam, in the position (x, y), eliminating the component and its sidelobes. The resulting dirty map is called **residual map**
4. If there is still flux, then repeat the steps (1-3) until all the main emissions are subtracted.
5. Reconstruction of all the delta components by convolving them with the clean beam.
6. After that, the **clean image** is produced

This algorithm is a computationally efficient method and works greatly on different sources. An example of a cleaning process is represented in Fig. 2.5.

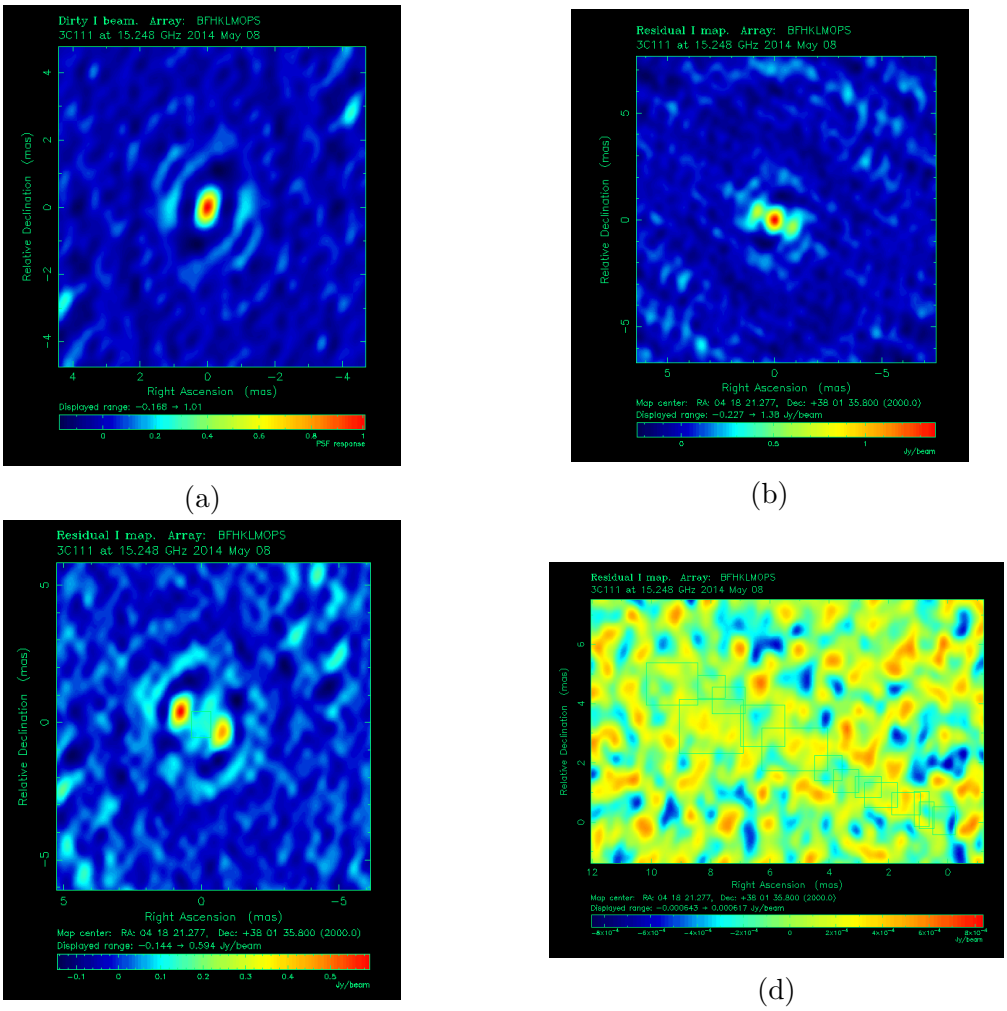

Figure 2.5: An example of some steps of the cleaning process. All of the maps have been obtained with `difmap`. **(a)**: The dirty beam map for the 15 GHz observation of the BG216F project of the MOJAVE program (the one in analyis in this thesis). It is the PSF of the observation. **(b)**: The dirty map for the 15 GHz observation of the BG216F project of the MOJAVE program (the one in analyis in this thesis) after the calibration of the dataset. No cleaning process is been performed yet. Sidelobes around the peak, are visible. **(c)**: The residual map for the 15 GHz observation of the BG216F project of the MOJAVE program (the one in analyis in this thesis) after the first cleaning iterations. Here, it is possible to see how the a priori calibration models (point-like sources) cause the symmetric emission. That is the reason for the "fake counter-jet" that disappears with the autocalibration. **(d)**: The residual map for the 15 GHz observation of the BG216F project of the MOJAVE program (the one in analyis in this thesis) after the cleaning process has been performed. It can be clearly seen that the emissions left are not due to the source but to the noise.

2.3 VLBI polarimetry

Polarization measurements are very important in radio astronomy. Most synchrotron radiation shows some degree of linear polarization that describes the projected geom-

etry/topology of the ordered magnetic field within the source. Therefore, through polarization studies, it is possible to infer important information about the magnetic field. The linear and circular polarizations of electromagnetic waves can be parameterized by different combinations of orthogonal electric vectors. In optics, polarization is described by the Stokes' parameters I, Q, U, and V . Stokes I is used for total intensity while different combinations of Q, U and V represent the linear and the circular polarization. The circular polarization can be divided into a left hand circular polarization (LCP) and a right hand circular polarization (RCP). These parameter are related with the RR, LL, RL and LR circular correlations in the following way:

$$V_{RR} = I + V \ ; \ V_{RL} = Q + iU \ ; \ V_{LR} = Q - iU \ ; \ V_{LL} = I - V \tag{2.18}$$

Moreove, Stokes parameters can be combined as follows in order to obtain:

$$m_l = \frac{\sqrt{Q^2 + U^2}}{I} = \frac{P}{I} \ ; \ m_c = \frac{V}{I} \ ; \ m_t = \frac{\sqrt{Q^2 + U^2 + V^2}}{I} \tag{2.19}$$

$$\theta = \frac{1}{2} \tan^{-1} \left(\frac{U}{Q} \right) \tag{2.20}$$

where m_l , m_c , and m_t are the fractions of linear, circular, and total polarization, respectively, P is the linear polarization intensity and θ is the Electric Vector Polarization Angle or **EVPA**.
Radio telescopes are sensitive to polarized signals. However, they bring in some "instrumental" polarization, which is often comparable if not even stronger than the source polarization. This spurious signal is related on the response of the whole system (antenna+receiver), and it is frequency dependent. The sensor for a given polarization (X,Y or R,L) has a (small) contribution from the other term, generally called *polarization leakage* or **D-term**. In practice the RCP feed measures a small contribution from the LCP signal, namely:

$$V_{R,obs} = V_{R,true} + D_R V_{L,true} \text{ and } V_{L,obs} = V_{L,true} + D_L V_{R,true} \tag{2.21}$$

The D-terms are often described as the leakage of the orthogonal polarization into the antenna and represent the instrumental polarization. Usually, these leakages have amplitudes of % order and are stable in times (days/weeks). If the ratio of the LCP and RCP gains does not vary a lot during an observing run, the D-terms can be best estimated by observing an unpolarized, point-like calibrator source. In such case, any polarization signature in the uncalibrated LR and RL visibilities can be associated with the polarization leakage effect. This can be understood as follows. The D-terms, also affect the RR,LL,RL and LR correlations. More specifically, it is possible to see that for the RR and LL correlations:

$$\begin{aligned} RR_{o,ij} &= (R_t + D_R L_t)_i (R_t + D_R L_t)_j = RR_{t,ij} + D_i LR_{t,ij} + D_j RL_{t,ij} + D_i D_j LL_{t,ij} \\ LL_{o,ij} &= (L_t + D_L R_t)_i (R_t + D_R R_t)_j = LL_{t,ij} + D_i RL_{t,ij} + D_j LR_{t,ij} + D_i D_j RR_{t,ij} \end{aligned} \tag{2.22}$$

where the subscripts o and t indicates the observed and true values, respectively and the subscripts i and j represent two different antennas. Since $D \approx 0.01$ for each

antennas, only the first term ($RR_{t,ij}$ or $LL_{t,ij}$) is significant. For the RL and LR correlations, on the other hand, it is possible to see that:

$$\begin{aligned} RL_{o,ij} &= (R_t + D_R L_t)_i (L_t + D_L R_t)_j = RL_{t,ij} + D_i LL_{t,ij} + D_j RR_{t,ij} + D_i D_j LR_{t,ij} \\ LR_{o,ij} &= (L_t + D_L R_t)_i (R_t + D_R L_t)_j = LR_{t,ij} + D_i RR_{t,ij} + D_j LL_{t,ij} + D_i D_j RL_{t,ij} \end{aligned} \tag{2.23}$$

Here, the first three terms are comparable (since the last one is a second order D-term, namely $0.01 * 0.01$). Therefore it can be seen how these D-terms affects the LR or RL correlations. In addition to that, if the source does not produce polarized emission, only the terms DLL and DRR are different from zero. For relatively low angular resolution observations at long wavelengths ($\lambda > 1\,\mathrm{cm}$), several well known calibrators are available for such purposes. However, most of the AGN sources are somehow resolved by much higher angular resolution for mm-VLBI observations. The calibrators also show larger intrinsic linear polarization at shorter wavelengths. Therefore, the technique used by VLBI polarimetric calibration algorithms, is to divide the total intensity and the unknown polarization structure of the calibrator into several discrete components and solve the D-terms and the source polarization simultaneously.

Another issue in polarimetric VLBI observations arises from the fact that the absolute value of the phase offsets between the RCP and LCP receivers are not known a priori. So, the polarization angle of the main science target can be determined only when the instrumental R-L phase offset is known. This can be achieved by observing suitable sky calibrators or using other external information. A couple of suitable calibrators are known to have stable polarization angles at long wavelengths.

2.4 The Very Long Baseline Array (VLBA)

The Very Long Baseline Array (VLBA) is an interferometer of the National Radio Astronomy Observatory (NRAO) consisting of 10 identical parabolic antennas, each one of them with a diameter of 25 m. The VLBA observes at different wavelengths, from 90 cm to 3 mm (327 MHz to 96 GHz) in eight discrete bands (P, L, S, C, X, U, K, Q and W). The VLBA antennas are located all across the United States and are identified as shown in Fig 2.6.

Figure 2.6: The map of the 10 VLBA antennas with the corresponding names. Image Credit: NASA/Goddard Space Flight Center.

The maximum baseline is 8600 km between Mauna Kea (the westernmost antenna) and Saint Croix (the easternmost antenna), while the shortest baseline is 200 km between Pie Town and Los Alamos in New Mexico. The signals from each antenna are recorded and the information is time-stamped using atomic clocks. The location of the VLBA antennas provides a reasonably uniform sampling of the (u, v) plane, allowing a suitable sensitivity to emitting regions covering nearly 2 orders of magnitude in angular size.

Chapter 3

Multiwavelenght observations of 3C111

3.1 Source introduction

The source that is taken into analysis is 3C111, a radio source with J2000 coordinates $RA = 4h18m21.277s; Dec = +38d1'35.800"$ and with a redshift of $z = 0.0491$. 3C 111 is a broad-line radio galaxy (BLRG) and it is classified as a Fanaroff-Riley class II (FR II) radio galaxy containing two radio lobes and a single-sided jet. In the radio domain, 3C111 has blazar-like behavior, although the jet lies at an angle significantly greater than the one of typical blazars ($10° - 20°$ with respect to the line of sight Jorstad et al. (2005)). The counter-jet is too faint to be detected because of the Doppler deboosting 1.6.3. The radio core is exceptionally compact and bright and the parsec-scale jet reveals features of an apparent superluminal motion. These blazar-like properties contrast with the morphology on larger scales, which is reminiscent of a typical radio galaxy. Apart from that, 3C111 has shown several radio flares in the past and it has also been detected at γ ray energy Schulz et al. (2020).

3.1.1 The MOJAVE program and the observation

MOJAVE[1] (Monitoring Of Jets in Active galactic nuclei with VLBA Experiments) is a long-term program to monitor radio brightness and polarization variations in jets associated with active galaxies visible in the northern sky Lister (2018). These jets are powered by the accretion of material onto billion-solar-mass black holes located in the nuclei of active galaxies. Their rapid brightness variations and apparent superluminal motions of blobs in the jet indicate that they contain highly energetic magnetized plasma moving on trajectories close to the line of sight at speeds approaching that of light.
The observations are made with the Very Long Baseline Array (VLBA). The observation taken in exam in this thesis is the one of the project BG216F in the MOJAVE program. The date of the observation is 08/05/2014 and it lasted from 15:07:00 UT to 02:05:00 UT (09/15/2014). It was performed by nine of the ten antennas of the VLBA array, because North Liberty did not observed due to a broken axle. The bands at which the observation was performed are L (~ 1.4 GHz), C (~ 5 GHz), X

[1] `https://www.physics.purdue.edu/MOJAVE/`

(~ 8.3 GHz), U (~ 15 GHz), K (~ 21 GHz), Q (~ 43 GHz), W (~ 86 GHz) and the WC band ($\sim 4-7$ GHz). In every band, there are 8 Intermediate Frequencies (IFs) separated by a bandwith (BW) of 32 MHz. The L-band observations, were discarded because they were affected by problems in the calibration of the IFs. Also the Wide C observation are not taken into account because they presented only 5 scans and it was probably just a test performed in the observation. In order to perform the calibration, apart from the target, four more sources were observed. These are $0415+398$, $4C39.25$, $3C84$, $3C454.3$. All the information about the observations in the various frequencies are shown in the table 3.1.

Band	Scans	Sources	1st - 8th IFs (GHz)	Visibilities (Target)
C	48	$0415+398$, $4C39.25$, $3C84$, $3C454.3$, $3C111$	4.86 - 5.09	81537 (21055)
X	48	$0415+398$, $4C39.25$, $3C84$, $3C454.3$, $3C111$	8.30 - 8.52	83437 (22834)
U	120	$0415+398$, $4C39.25$, $3C84$, $3C454.3$, $3C111$	15.13 - 15.36	139375 (51012)
K	174	$0415+398$, $4C39.25$, $3C84$, $3C454.3$, $3C111$	21.77 - 22.00	475564 (377885)
Q	147	$4C39.25$, $3C84$, $3C454.3$, $3C111$	43.67 - 43.90	164478 (141033)
W	147	$4C39.25$, $3C84$, $3C454.3$, $3C111$	87.44 - 87.66	164379 (140988)

Table 3.1: Information about the BG216F observation performed on the 08/05/2014. In the columns are shown: the band for which the information are given; the number of the total scans obtained; the sources that were observed; the first and last IFs ($BW = 32$ MHz); the number of the total visibilities and the ones relative to 3C111. The L band and the Wide C band were discarded due to technical problems.

3.2 Calibration of the dataset

The analysis of the dataset has been performed with AIPS and with ParselTongue. The *Astronomical Image Processing System* (AIPS), is a software, primarily used for the reduction and analysis of radio interferometric data, that allows calibration, data analysis and image display. The calibration tasks of AIPS do not work directly on the actual visibility dataset, they create instead, tables to be applied to the data. The vast majority of all the data analysis, was actually performed using ParselTongue scripts. ParselTongue is a python interface to AIPS and it performs the data reduction in an automated way. The scripts used in this thesis were provided by Dr. J. L. Gómez and his research team but then, they were accurately adapted for this work.
Thanks to these scripts, it was possible to perform the calibration and reduction of the dataset. As stated in 2.2.2, the calibration is needed in order to obtain the real amplitude and phase of the visibilities, taking into account all the factors that could affect the observations (the atmosphere, the instrumentation, the geometric delay, etc ...). After reading the data, through the ParselTongue script, an inspection of the system temperature was performed. As explained in the 2.1.2, the system temperature T_{sys} is the sum of the temperature of all the components and it is related to the SNR through the bandwidth and the integration time. A little percentage of the data were flagged because they were clearly outliers. This was done through the task `SNEDT`. After setting the flux of the various sources in the source (SU) table (a table that contains source specific information such as flux densities and positions), the autocorrelation of the data was performed with the task `ACCOR`. This allows the

signals of a source, received by all the antennas, to be properly added. Once the autocorrelation has been completed, the a priori amplitude calibration and opacity corrections can be calculated. This procedure is done with the `APCAL` task selecting the correct value of the system temperatures for the various IFs and polarizations. After that, the parallactic angle correction has been applied to the dataset with the task `CLCOR`. The calibration procedures described until now, are called *a priori* because they use known information about the observation to estimate predictable effects that are due to the antenna positioning, the positions of the radio source, the thickness of the atmosphere (opacity) and so on.

3.2.1 Fringe fitting

After the initial correlation, the data still exhibits residual fringe rates and delays. The main causes for these residuals are, for example, different clock models, weather and different geometric paths over the telescopes. The process of finding these residuals is known as *Fringe Fitting*, as explained in Cotton (1995). As a result, the visibility data become more coherent in both frequency and time. As stated in 2.2, an interferometric phase ϕ can be written as $\phi = 2\pi\nu t$. Therefore a first-order approximation of the phase error $\Delta\phi$ can be expressed as:

$$\Delta\phi = \phi_0 + \left(\frac{\partial\phi}{\partial\nu}\Delta\nu + \frac{\partial\phi}{\partial t}\Delta t\right)$$

where $\frac{\partial\phi}{\partial\nu}$ is called *delay* and describes the variation of the residual phase in frequency, and $\frac{\partial\phi}{\partial t}$ is called *fringe rate* or simply *rate* and describes the variation of the residual phase in time. Delays and rates can be reasonably assumed as characteristics of each station, thus the modeling is performed *antenna basis*. Moreover, the number of baselines of an array $N(N1)/2$ is usually much larger than the total number of antennas N.

Fringe Fitting (via the AIPS task FRING) solves for some residual error in the fringe position (delay and rate) in time and frequency, left over after the removal of the geometric model applied at the correlator. Their origin can be found in atmospheric transmission, cable transmission, etc. Delays and rates are factorized on each antenna/polarization (and IF) and are found by the comparison with a model visibility for a calibration source (assumed to be pointlike and at the phase center, i.e. where the each telescope was pointing). The effects of such correction can be seen in Fig. 3.1, where, after being corrected for delays and fringe rate, the phases of the baseline Fort Davis-Pie Town are quite well aligned to 0 across the whole observing bandwidth (right panel).

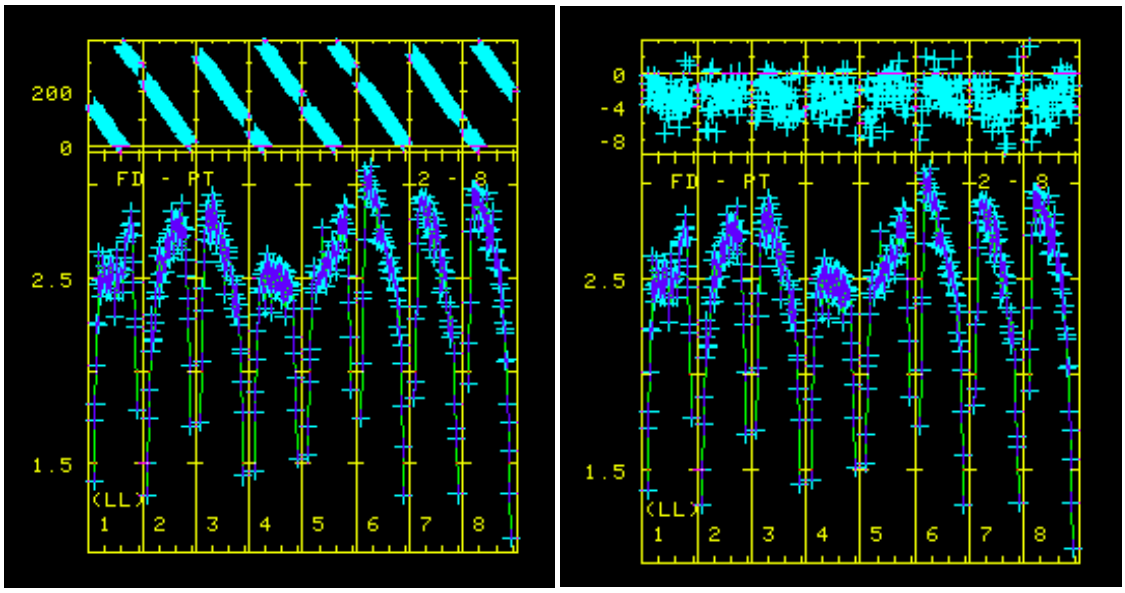

(a) (b)

Figure 3.1: An example of the effect of the *fringe fitting* on the dataset. **(a)**: Phase (top) and amplitude (bottom) of 3C111 in the C band, for a given scan, on the baseline between Fort Davies - Pie Town, before the fringe fitting. **(b)**: Phase (top) and amplitude (bottom) of 3C111 after the fringe fitting. Here it can be seen that the phases are now assuming a flat behaviour across the IFs.

After performing the fringe fitting, it was possible to calculate and apply the *bandpass calibration*. This is the process of measuring and correcting the frequency dependent part of the gains. The effect of this calibration is to normalize all the channels of each IFs at a certain value. Before splitting the multisource dataset for each source, it has been applied the atmospheric phase correction. This takes into account the way the atmosphere affect the visibilities, through models of absorption.

3.3 Imaging with `Difmap`

After determining the various calibrations, they were applied to the visibilities which were also averaged in frequency at the stage of "splitting" the dataset into the sources for each band. At this stage, it was possible to perform the imaging process with `Difmap`.
`Difmap` is a stand-alone program used by the radio-astronomy community to produce images from radio interferometers. It reads and writes the standard UV FITS file format produced by packages such as AIPS, and provides convenient ways to inspect, edit, and self-calibrate visibility data while incrementally building up a model of the sky. The first step was to inspect the data in order to see if the calibration has been successfully performed. Then it was possible to proceed with the cleaning. It is necessary to select the regions of emission and then keep on with the cleaning until what is left is just noise.

3.3.1 *Self-calibration* and closure relationships

Along with the cleaning, it is necessary to do the so called *phase self-calibration*. The fringe fitting and a-priori amplitude calibration get rid of many known effects that contaminate the data. However, even after rigorous data calibration, some systematic effects could come up. Some examples of these errors are the ones due to the antenna pointing or the turbulent phase variations caused by the atmosphere. These effects are unpredictable and occur on various temporal scales which need to be dealt with using an iterative approach. Therefore, several approaches are possible to estimate and remove the unpredictable errors. When the science target is sufficiently bright (that is the case of 3C111), the most basic structure of the source (e.g. the core) can be modeled and imaged even under the presence of unpredictable noises. Then it is possible to assume this structure as a "calibrator" and estimate station gain correction factors to calibrate certain fraction of the data. As the initial model is incomplete, this procedure can be repeated iteratively until the model agrees with the data. This strategy is called *self-calibration* or *selfcal*. In a general selfcal loop, the station gain correction factors are estimated so that they minimize the sum of the difference between the model and the corrected data. Furthermore, it is impossible to correct the data if they suffer from very large errors or if the first preliminary model is not suitable for the purpose. In this regard, the success of self-calibration depends on the total number of independent measurements. Therefore, in order to boost the number of constraints, special observable quantities immune to station-based errors can be calculated from the raw visibilities. Such observables are the **closure phases** and **closure amplitudes**. Taking the Eq. 2.16 only for the phases, it can be obtained:

$$\theta_{ij}^{obs} = \delta\theta_i - \delta\theta_j + \theta_{ij}^{true} \tag{3.1}$$

where $\delta\theta_i$ and $\delta\theta_j$ are the phases error of the antenna i and j respectively. The Eq. 3.1 is called *closure phases relationship*. This can be used to sum the phases of three different antennas i, j and k and, taking into account that $\delta\theta_i$, $\delta\theta_j$ and $\delta\theta_k$ cancel each other:

$$\Phi_c = \theta_{ij}^{obs} + \theta_{jk}^{obs} + \theta_{ki}^{obs} = \theta_{ij}^{true} + \theta_{jk}^{true} + \theta_{ki}^{true} = \Phi_c^{'} \tag{3.2}$$

where Φ_c is the observed closure phase and $\Phi_c^{'}$ is the true one. It can be easily seen that these two quantities are the same for a three antenna system. Similarly to the phases, by taking the Eq. 2.16 only for the amplitudes, it can be shown that the observed closure amplitude is equal to the true one for a system with four antennas. For N antennas, the number of independent closure phases is $(N-1)(N-2)/2$ and the number of independent closure amplitudes is $N(N-3)/2$. Therefore, a large number of antennas can produce enough data to recover the source information accurately. In addition to that, there is the true noise and therefore the solutions are computed in a statistical way. As the number of iterations increases the precision of the model that fits the visibilities.

3.3.2 Producing the total intensity images

The self calibration relationship explained before, need to be used together with the cleaning process. More specifically, the steps applied to produce the total intensity

images are:

1. Upload the calibrated data in `difmap`.
2. Select the Stokes parameter I in order to produce the total intensity images.
3. Inspecting the data with the visibility plot vs time (*vplot*), the amplitude and phases vs the uv distance (*radplot*), etc ...
4. Select the size of the map and of the pixel.
5. Perform the cleaning by choosing the cleaning boxes and applying the phase selfcal, until all the main emissions are covered.
6. Switch to the natural weighting that gives more importance to the shorter baseline, in order to better resolve the extended sources and re-do the step 5.
7. Inspect the radplot to see if the model fits correctly the data.
8. Perform the amplitude selfcal, starting with a long solution interval (e.g. 240 minutes).
9. Remove the model and repeat the steps 5 to 8 with a smaller solution interval (in this case 180,120,60,30,10,5,2,1 minutes) as long as the model fits better the data.

By following these steps, it was possible to produce the total intensity images in all the 6 bands. The images are shown in the following pages and the main features are written in each caption. The 86 GHz image (3.7), published in this thesis, is the first map of 3C111 ever made with the VLBA at this frequency. In addition to that, it is important to notice that the K band was too low and therefore all the visibilities were multiplied by a factor of ≈ 1.2. This is explained in more detail in the A. By looking at those maps, it is possible to notice that the jet lies approximately at a position angle of $\sim 65°$, in agreement with the literature.

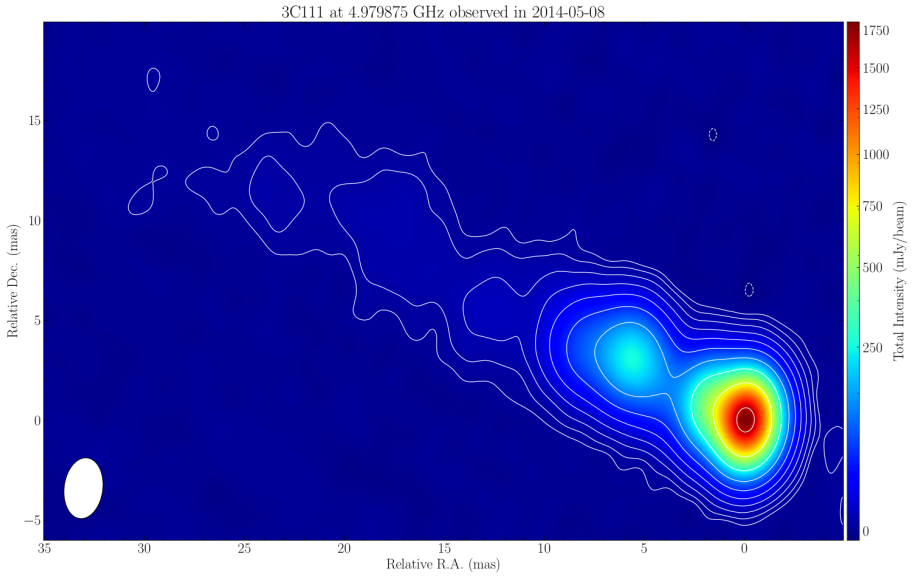

Figure 3.2: Total intensity map of 3C111 in the C band. The peak total intensity of the map is 1.80 Jy/Beam with an off-source rms of 0.18 mJy/Beam. The integrated total intensity is 2.95 Jy. Contour levels are $-0.03, 0.03, 0.07, 0.18, 0.43, 1.05, 2.56, 6.24, 15.18, 36.96, 90.0\%$ of the peak. The restoring beam, plotted in the bottom left corner, is 3.06×1.93 mas with a position angle of $-7.0°$.

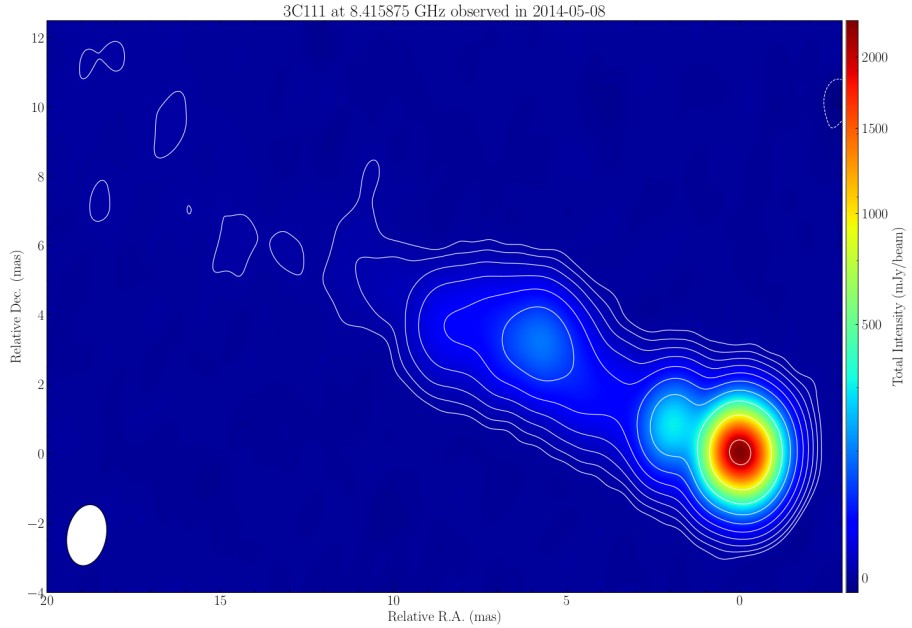

Figure 3.3: Total intensity map of 3C111 in the X band. The peak total intensity of the map is 2.28 Jy/Beam with an off-source rms of 0.30 mJy/Beam. The integrated total intensity is 3.83 Jy. Contour levels are $-0.04, 0.04, 0.09, 0.22, 0.52, 1.23, 2.9, 6.84, 16.15, 38.12, 90.0\%$ of the peak. The restoring beam, plotted in the bottom left corner, is 1.78×1.13 mas with a position angle of $-11.0°$.

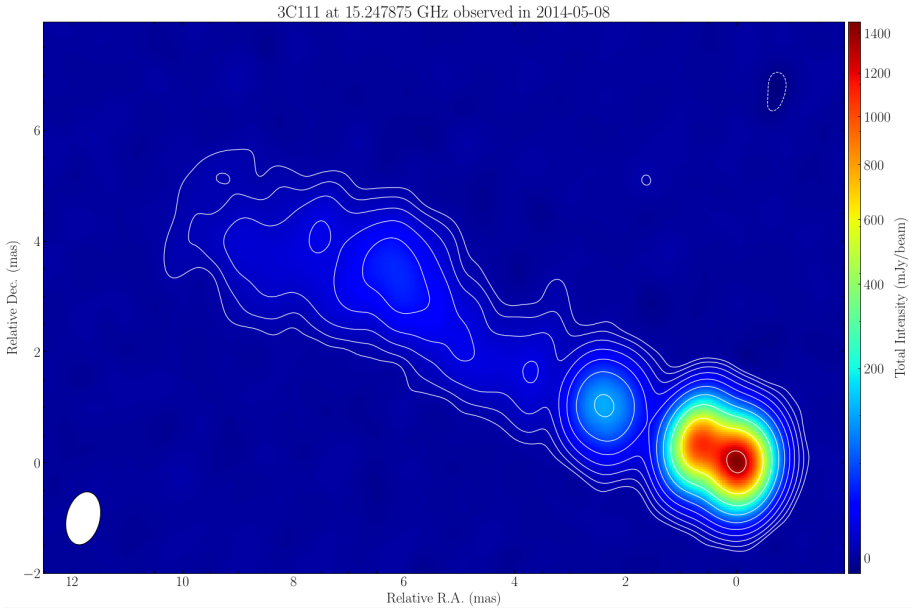

Figure 3.4: Total intensity map of 3C111 in the U band. The peak total intensity of the map is 1.46 Jy/Beam with an off-source rms of 0.30 mJy/Beam. The integrated total intensity is 3.43 Jy. Contour levels are $-0.06, 0.06, 0.14, 0.31, 0.7, 1.57, 3.53, 7.94, 17.83, 40.06, 90.0\%$ of the peak. The restoring beam, plotted in the bottom left corner, is 0.97×0.6 mas with a position angle of $-14.0°$.

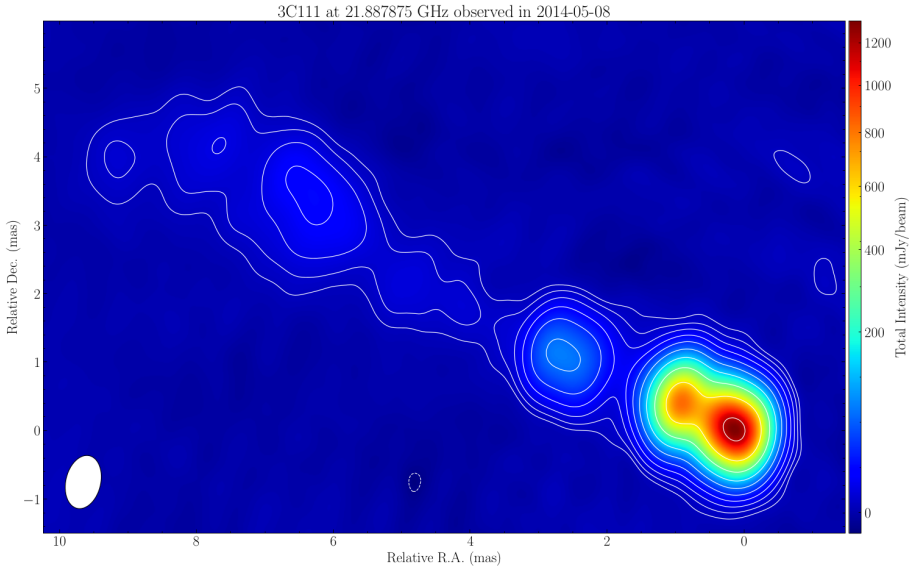

Figure 3.5: Total intensity map of 3C111 in the K band. The peak total intensity of the map is 1.31 Jy/Beam with an off-source rms of 0.65 mJy/Beam. The integrated total intensity is 3.30 Jy. Contour levels are $-0.15, 0.15, 0.3, 0.62, 1.26, 2.57, 5.23, 10.65, 21.69, 44.18, 90.0\%$ of the peak. The restoring beam, plotted in the bottom left corner, is 0.79×0.51 mas with a position angle of $-13.0°$.

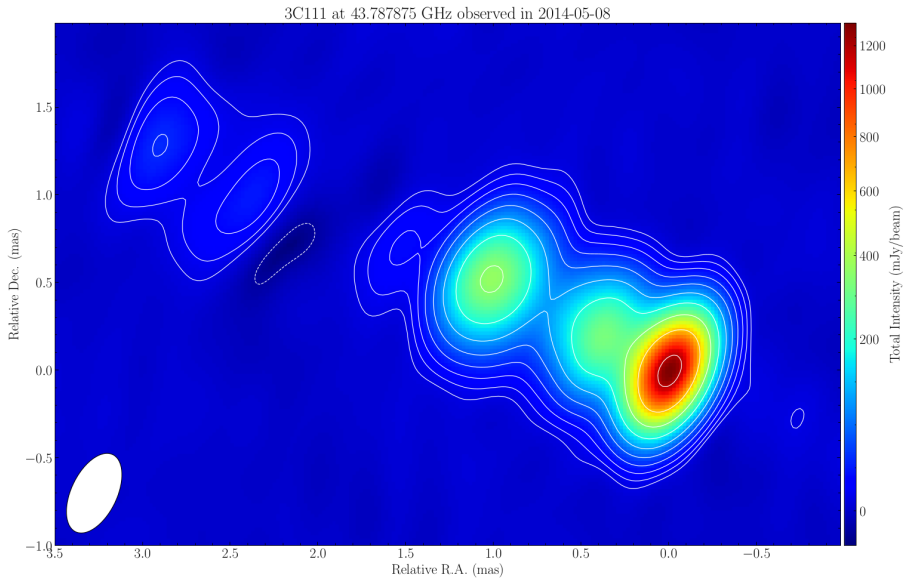

Figure 3.6: Total intensity map of 3C111 in the Q band. The peak total intensity of the map is 1.31 Jy/Beam with an off-source rms of 1.50 mJy/Beam. The integrated total intensity is 2.65 Jy. Contour levels are $-0.34, 0.34, 0.64, 1.18, 2.2, 4.08, 7.57, 14.06, 26.1, 48.47, 90.0\%$ of the peak. The restoring beam, plotted in the bottom left corner, is 0.49×0.26 mas with a position angle of $-26.0°$.

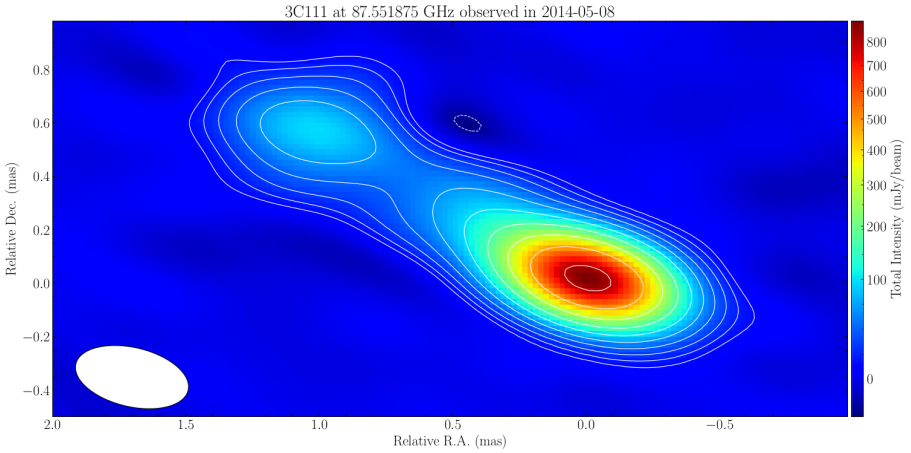

Figure 3.7: Total intensity map of 3C111 in the W band. The peak total intensity of the map is 0.89 Jy/Beam with an off-source rms of 2.50 mJy/Beam. The integrated total intensity is 1.19 Jy. Contour levels are $-0.84, 0.84, 1.42, 2.38, 4.0, 6.72, 11.29, 18.97, 31.88, 53.56, 90.0\%$ of the peak. The restoring beam, plotted in the bottom left corner, is 0.43×0.22 mas with a position angle of $77.0°$. This is the first image of 3C111 made at this frequency with the VLBA.

3.3.3 Producing the polarization images

After producing the Stokes I images, it was possible to analyse the polarization of the source in each band. In order to do that, as explained in the 2.3, additional calibration steps are needed.

Polarimetry calibration

The first step was to upload the final map file into the ParselTongue script. After that it was necessary to divide the source into discrete components (usually about 10) and then, thanks to the task `LPCAL` it was possible to determine the effective feed polarization parameter for the VLBA array. By looking at the output log produced in this last step, it was possible to check the D-terms for all the frequencies. The various D-terms are plotted in the Fig. 3.8.

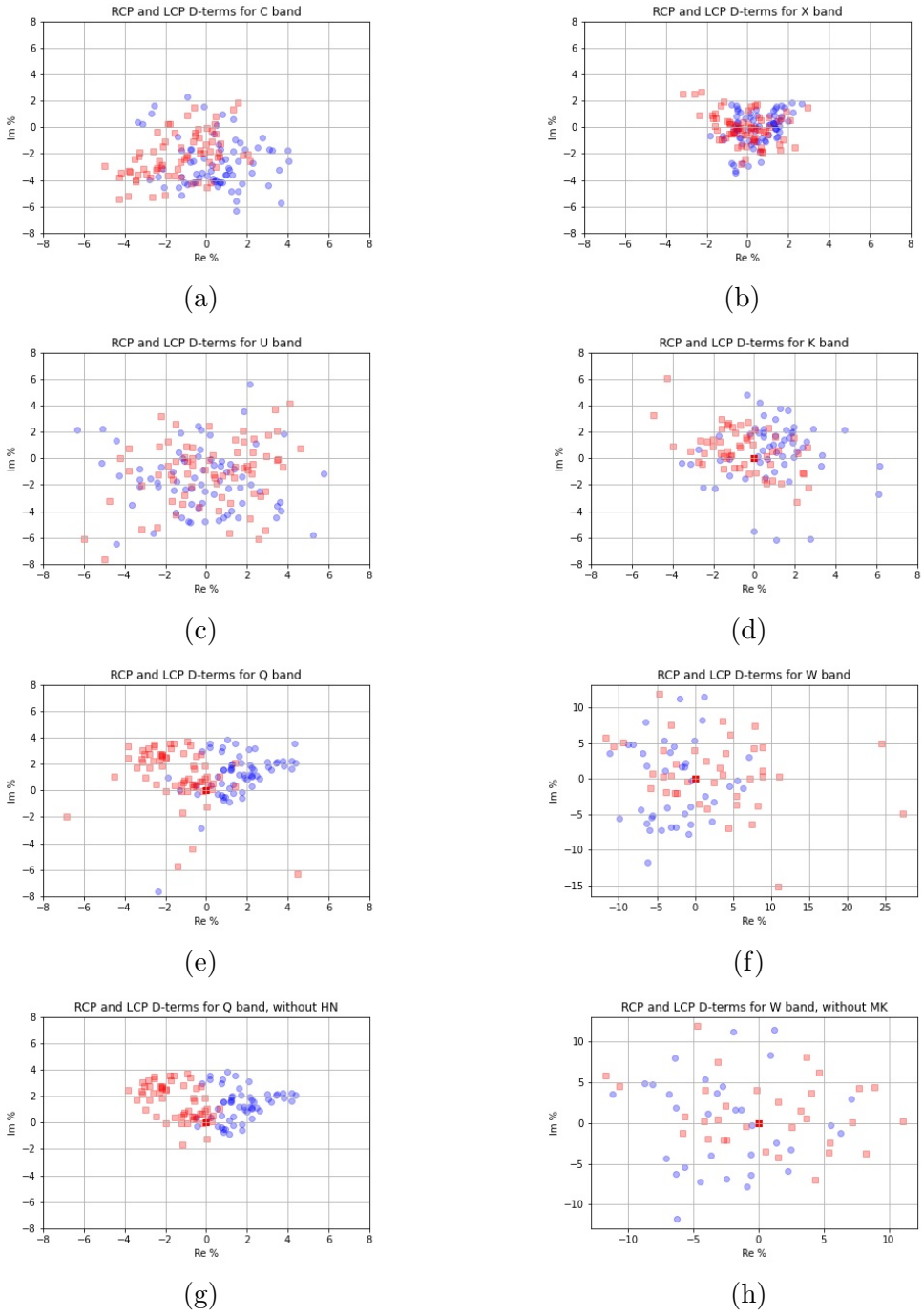

(a) (b) (c) (d) (e) (f) (g) (h)

Figure 3.8: From **(a)** to **(f)** are shown the D-terms plots for all the bands in the increasing frequency order (C,X,U,K,Q,W). In the axis are represented the percentage of leakage in the real and imaginary part of the polarization. **(g)** and **(h)** display respectively the D-terms for the Q band without HN and for the W band without MK.

As it can be seen in the Fig 3.8, the leakage factor is always below 10% in all the bands, except for the W. In the 86 GHz band, the leakage percentage can reach, with some values, a bit more of 10%, confirming that at mm-wavelengths the leakages are more important. By comparing 3.8e and 3.8f with 3.8g and 3.8h, it can be seen how some antennas (more specifically, HN for the Q band and MK for the W band)

had some issues that caused a major leaking with respect to the other ones.

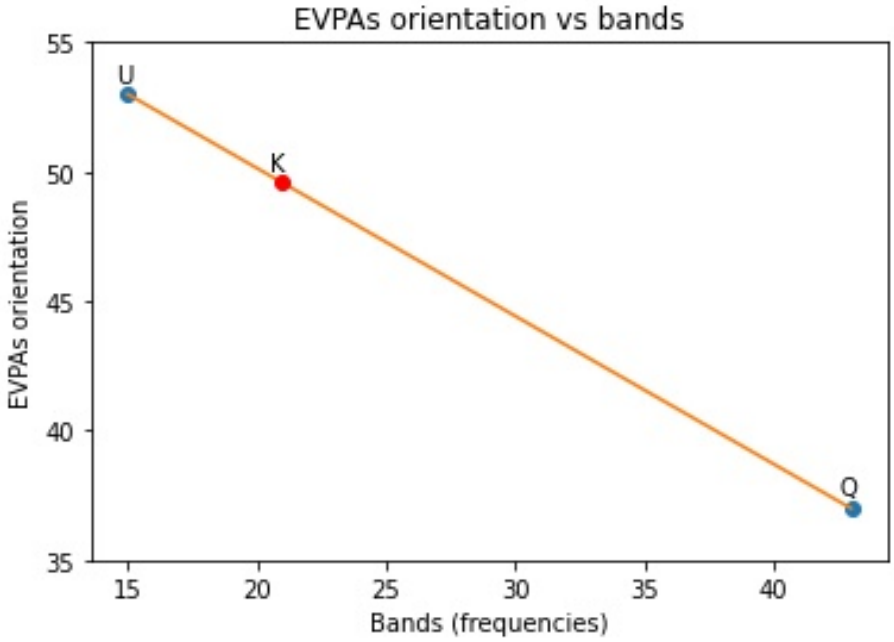

Figure 3.9: Plot of the EVPAs integrated orientation vs bands. The blue dots represent the known value taken from various sources of information while the red dot represent the value obtained with a linear fit that is presented as the orange line. The values for the calibrated EVPAs are 53° for the U band, 49° for the K band and 37° for the Q band

For what concerns the calibration of the absolute orientation of the EVPAs, that will be fundamental for the rotation measure analysis 4.3, different sources of information were used. For the U band, the MOJAVE database Lister (2018) for 3C111[2] provides a table in which it is possible to extract some parameters about the source for every observation. From here it was possible to get the integrated orientation of the EVPAs for the source at 15 GHz, that is equal to 53°. Another catalog that provides information of AGNs observation is the one from Boston University [3]. This survey is for observations in the Q band (43 GHz) and, luckily, it was possible to obtain the integrated orientation of the EVPAs for an observation of the source that took place a few days before the one analysed in this thesis (03/05/2014). The value of the integrated orientation of the EVPAs in the Q band is 37°. For what concerns the K band value, it has been derived with a linear fit, as shown in Fig. 3.9. The integrated orientation of the EVPAs for the K is 49°.

Polarization imaging

After the removal of the instrumental polarizazion, the calibration for the absolute orientation of the E vector, and the final stage of self-calibration, the Stokes' U

[2]The MOJAVE web page for 3C111: `http://www.physics.purdue.edu/astro/MOJAVE/sourcepages/0415+379.shtml`

[3]The Boston University web page for 3C111: `https://www.bu.edu/blazars/VLBA_GLAST/3c111.html`

and Q images have been obtained. In order to do that it is necessary to perform the cleaning in a slightly different way than before. This cleaning was guided on the basis of the total intensity emission, since polarized signal is expected on those regions. Moreover, since the components of P are vectors, it could also be present a significant negative signal (right panel of 3.10). Once the cleaning on the source has been performed, it is possible to extend the cleaning process to all the field to "lowering" the noise in order to have it similar to the one of the Stokes I map.

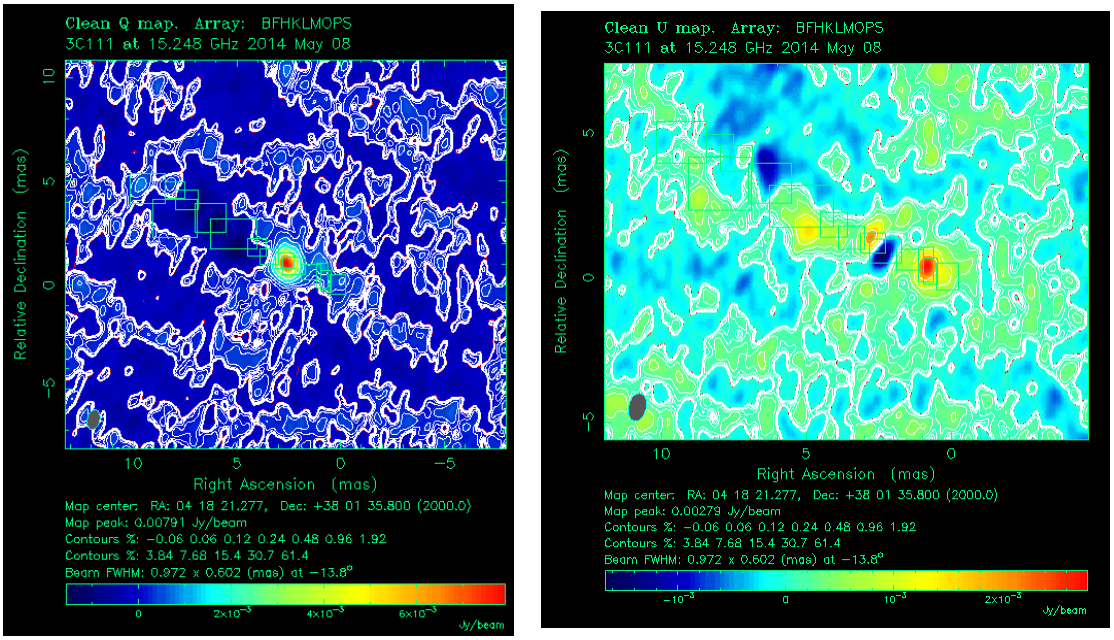

(a) (b)

Figure 3.10: An example of the clean maps of 3C111 in the U band for the Stokes Q **(a)** and the Stokes U **(b)** parameter. Both of the images are taken with `difmap`.

After computing the maps for the Stokes I, Q and U parameter, it is finally possible to produce the linear polarization maps of the source, thanks to the first equation in 2.19 ($P = \sqrt{U^2 + Q^2}$). For each observing frequency, in Figs 3.11 through 3.16 it is shown the total intensity emission in white contours along with the polarized emission in color and EVPAs. The EVPAs in the U, K and Q images were accurately rotated in order to obtain the value showed in 3.9.

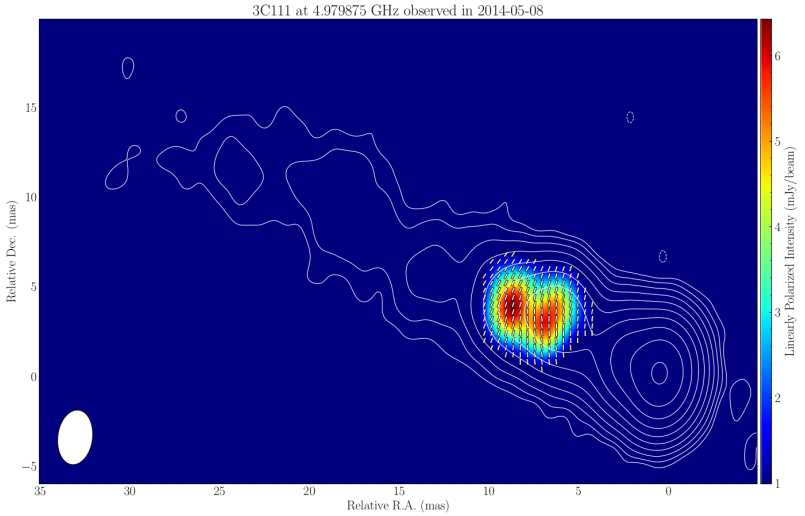

Figure 3.11: Polarization map of 3C111 in the C band. The peak linear polarization intensity of the map is 6.43 mJy/Beam with an off-source rms of 0.33 mJy/Beam. The integrated linear polarization intensity is 158.82 mJy. Contour levels are $-0.03, 0.03, 0.07, 0.18, 0.43, 1.05, 2.56, 6.24, 15.18, 36.96, 90.0\%$ of the peak. The restoring beam, plotted in the bottom left corner, is 3.06×1.93 mas with a position angle of $-7.0°$. The white bars represent the absolute orientation of the EVPAs.

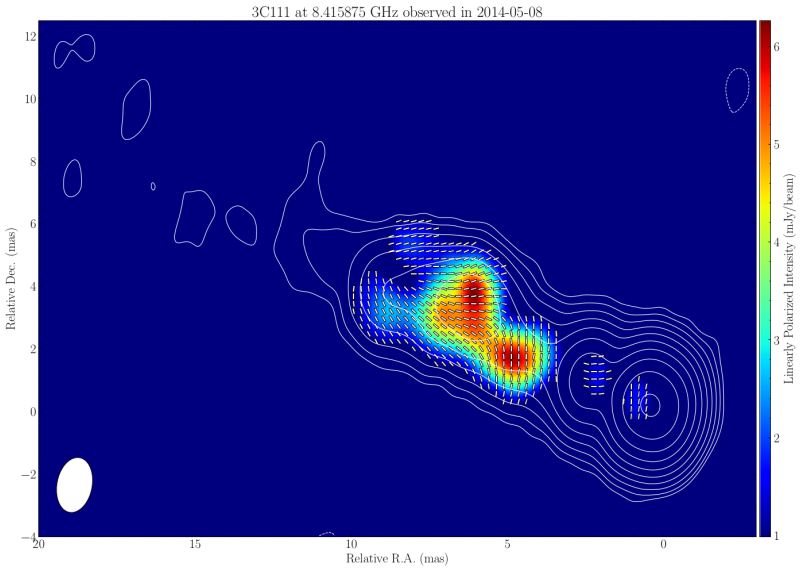

Figure 3.12: Polarization map of 3C111 in the X band. The peak linear polarization intensity of the map is 6.26 mJy/Beam with an off-source rms of 0.33 mJy/Beam. The integrated linear polarization intensity is 186.11 mJy. Contour levels are $-0.04, 0.04, 0.09, 0.22, 0.52, 1.23, 2.9, 6.84, 16.15, 38.12, 90.0\%$ of the peak. The restoring beam, plotted in the bottom left corner, is 1.78×1.13 mas with a position angle of $-11.0°$. The white bars represent the absolute orientation of the EVPAs.

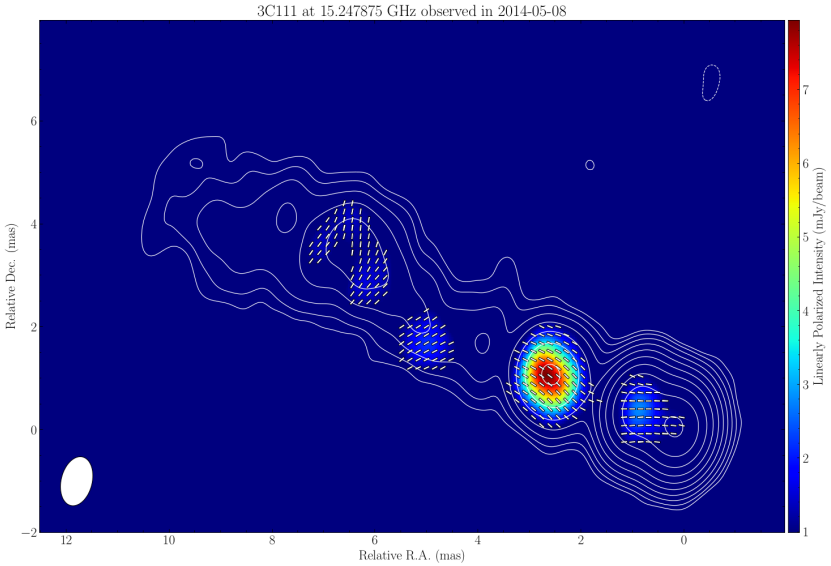

Figure 3.13: Polarization map of 3C111 in the U band. The peak linear polarization intensity of the map is 7.94 mJy/Beam with an off-source rms of 0.33 mJy/Beam. The integrated linear polarization intensity is 695.37 mJy. Contour levels are $-0.06, 0.06, 0.14, 0.31, 0.7, 1.57, 3.53, 7.94, 17.83, 40.06, 90.0\%$ of the peak. The restoring beam, plotted in the bottom left corner, is 0.97×0.6 mas with a position angle of $-14.0°$. The white bars represent the absolute orientation of the EVPAs.

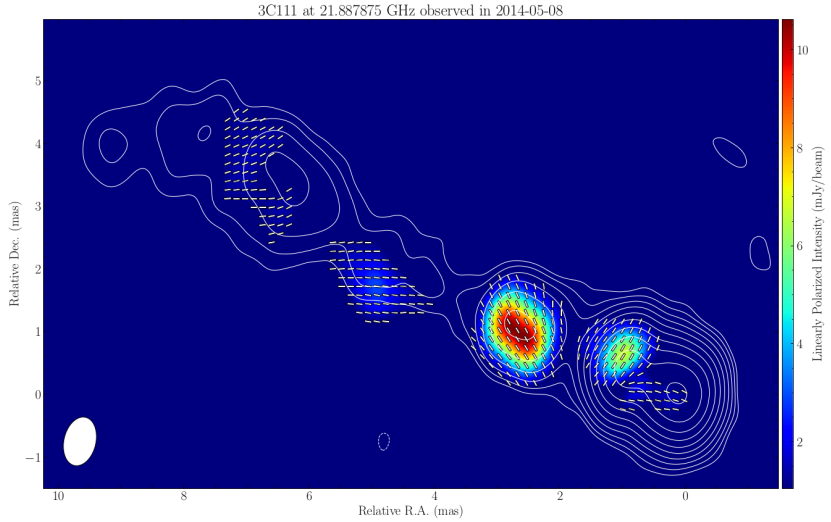

Figure 3.14: Polarization map of 3C111 in the K band. The peak linear polarization intensity of the map is 10.62 mJy/Beam with an off-source rms of 0.35 mJy/Beam. The integrated linear polarization intensity is 327.45 mJy. Contour levels are $-0.15, 0.15, 0.3, 0.62, 1.26, 2.57, 5.23, 10.65, 21.69, 44.18, 90.0\%$ of the peak. The restoring beam, plotted in the bottom left corner, is 0.79×0.51 mas with a position angle of $-13.0°$. The white bars represent the absolute orientation of the EVPAs.

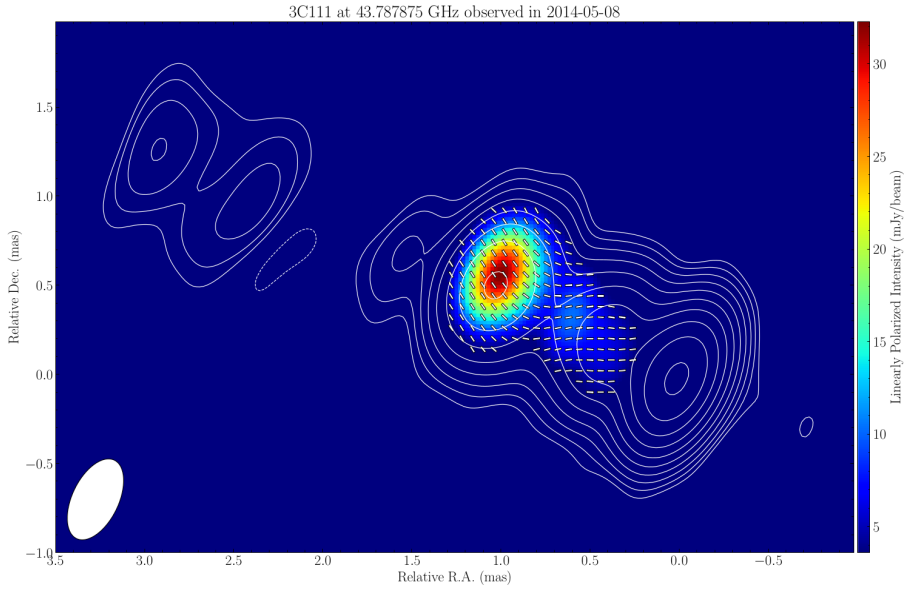

Figure 3.15: Polarization map of 3C111 in the Q band. The peak linear polarization intensity of the map is 32.29 mJy/Beam with an off-source rms of 1.20 mJy/Beam. The integrated linear polarization intensity is 501.44 mJy. Contour levels are $-0.34, 0.34, 0.64, 1.18, 2.2, 4.08, 7.57, 14.06, 26.1, 48.47, 90.0\%$ of the peak. The restoring beam, plotted in the bottom left corner, is 0.49×0.26 mas with a position angle of $-26.0°$. The white bars represent the absolute orientation of the EVPAs.

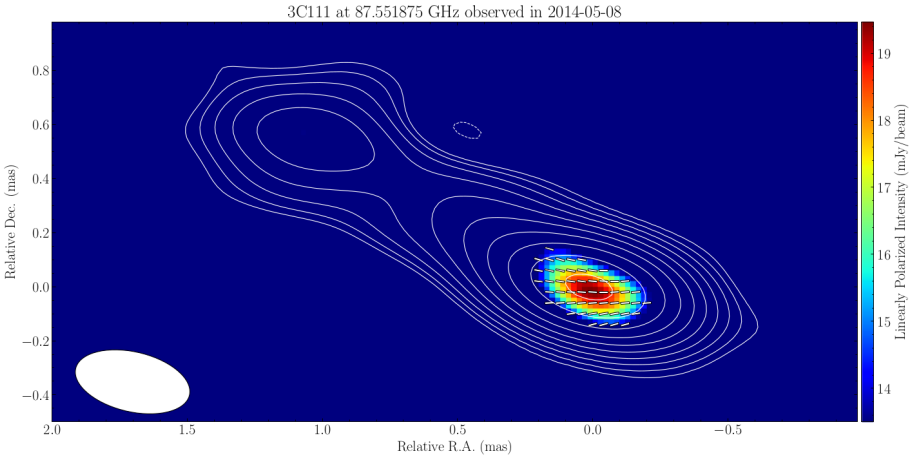

Figure 3.16: Polarization map of 3C111 in the W band. The peak linear polarization intensity of the map is 19.47 mJy/Beam with an off-source rms of 3.50 mJy/Beam. The integrated linear polarization intensity is 771.29 mJy. Contour levels are $-0.84, 0.84, 1.42, 2.38, 4.0, 6.72, 11.29, 18.97, 31.88, 53.56, 90.0\%$ of the peak. The restoring beam, plotted in the bottom left corner, is 0.43×0.22 mas with a position angle of $77.0°$. The white bars represent the absolute orientation of the EVPAs.

Moreover, it is possible to compute the **fraction of polarization**, defined in 2.19 as $m_l = \dfrac{P}{I}$. This is computed both for the integrated values of P and I and for

the peak. The peak fraction of polarization was computed by looking at the peak of the polarization map and storing its value and position. Once this was done, the value of the total intensity map for the same position could be computed. Hence, it was possible to estimate $m_{l,peak}$ as the ratio of the two values times 100 (to show that as a percentage). All the values are presented in the table 3.2.

Band	Total	Peak total	Pol	Peak pol	m_l	$m_{l,peak}$	EVPA
C	2.94 Jy	1.80 Jy/beam	158.82 mJy	6.43 mJy/beam	5.39%	8.17%	//
X	3.83 Jy	2.28 Jy/beam	186.11 mJy	6.26 mJy/beam	4.85%	5.42%	//
U	3.49 Jy	1.46 Jy/beam	695.37 mJy	7.94 mJy/beam	19.96%	6.35%	53°
K	3.30 Jy	1.31 Jy/beam	327.45 mJy	10.62 mJy/beam	9.92%	14.86%	49°
Q	2.65 Jy	1.31 Jy/beam	501.44 mJy	32.3 mJy/beam	18.95%	9.09%	37°
W	1.18 Jy	0.89 Jy/beam	771.29 mJy	19.5 mJy/beam	65.97%	2.19%	//

Table 3.2: A table that shows different values for each bands: The first column (*Band*) represents the bands; the second one (*Total*) represents the integrated total intensity of the map; the third one (*Peak total*) represents the peak total intensity of the map; the fourth one (*Pol*) represents the integrated linear polarization intensity of the map; the fifth one (*Peak pol*) represents the peak linear polarization intensity of the map; the sixth one (m_l) represents the integrated fraction of polarization of the map; the seventh one ($m_{l,peak}$) represents the fraction of polarization at the peak of the polarization map and the eighth one (*EVPA*) represent the integrated Electric Vector Position Angle of the map.

The polarized emission lies mostly in the jet at all the frequencies and, as the wavelength is decreasing, this emission arises also from regions progressively closer to the jet basis. It is possible to recognize some features that are common at more frequencies. For some of them, it will be performed the Rotation Measure analysis 4.3. Moreover, by looking at the values of the table 3.2 some interesting insights emerge. For example, it can be noticed the trend of m_l and $m_{l,peak}$ in the various bands. This can be explained by the fact that at lower frequencies the most prominent emission in the Stokes I maps is usually the core that does not show a significant amount of polarization, while in the polarization maps, the most prominent emission comes from the jet. At higher ν, on the other hand, the total intensity emission comes from smaller regions and so, if there is some polarization feature, this is more important in percentage. Furthermore, the peak of the polarization becomes a smaller fraction of the total intensity at higher frequencies. Similarly to what stated before, this can be also explained by looking at the emitting regions. In fact, since the polarized emission has a lower value in terms of Jy compared to the total intensity, if the peak of polarization is in a region close to the peak of the total intensity (namely the core), this will be less important in the fraction of polarization. For example, in the W band, it can be seen that $m_l \approx 66\%$ while $m_{l,peak} \approx 2\%$. This is due to the fact that the main emission comes from the core for both the total intensity and the polarization. Since the total intensity emission is considerably higher than the polarization, $m_{l,peak}$ is lower. The total emitting region in the Stokes I map, on the other hand, is small compared to the other frequencies. Therefore, the integrated value of P is a high percentage of the integrated value of I. A similar explanation can be provided for all the bands.

Chapter 4

Analysis and discussion

4.1 Core shift

The radio core is the site at the jet base where there is the transition from optically thick to thin emission. Therefore the observed position of the radio core depends on the frequency as stated in Lobanov (1998). Studies of the radio properties of astrophysical jets need to be carried out at various frequencies, and in their comparison and combination, the relative positions of emitting components must take into account this opacity effect. The "core-shift problem" emerges as a result of the higher frequencies, at which the optically thin region begins closer to the base of the jet than at lower frequencies. Generally, the unresolved radio core has been related to self-absorbed synchrotron radiation from the approaching jet. As can be seen in Dodson et al. (2017), the standard conical jet model hypothesizes that the core is not a physical feature in the jet, but corresponds to the location at which the jet becomes optically thin, and therefore its position shifts with observing frequency. It is possible to see that the distance r from a given reference, i.e. the BH position, scales as $r \propto \nu^k$, where ν is the frequency and k is a value close to -1. In order to estimate the core shift, all the images have been referenced to the highest frequency (86 GHz) and a cross-correlation between the images have been performed (see 4.2). After that, through `difmap` it was possible to extrapolate the x and y position (x_{pos}, y_{pos}) of the peak, in [mas] at the different frequencies. Therefore the distance from the core have been calculated in the following way:

$$r = \sqrt{x_{pos}^2 + y_{pos}^2} \text{ [mas]} \tag{4.1}$$

Moreover, the errors on x_{pos} and y_{pos} have been estimated, in a conservative way, as half of the pixel size $pixel/2$ for each map. From the Theory of error propagation Lindberg (2000), it is possible to estimate the associated uncertainties for r, through the Eq. (4.2).

$$\Delta r = \sqrt{\left(\frac{x_{pos}}{\sqrt{x_{pos}^2 + y_{pos}^2}}\Delta x_{pos}\right)^2 + \left(\frac{y_{pos}}{\sqrt{x_{pos}^2 + y_{pos}^2}}\Delta y_{pos}\right)^2} \text{ [mas]} \tag{4.2}$$

Since $\Delta x_{pos} = \Delta y_{pos} = pixel/2$, the associated error on r is again equal to half of the pixel size. The value of the parameters with their associated uncertainties is presented in Tab. 4.1.

Bands	x_{pos} [mas]	y_{pos} [mas]	r [mas]	Pixelsize [mas]
C	0.48 ± 0.04	0.16 ± 0.04	0.50 ± 0.04	0.08
X	0.36 ± 0.02	0.16 ± 0.02	0.40 ± 0.04	0.04
U	0.12 ± 0.02	0.08 ± 0.02	0.14 ± 0.0	0.04
K	0.12 ± 0.01	0.02 ± 0.01	0.12 ± 0.01	0.02
Q	-0.01 ± 0.01	-0.01 ± 0.01	0.01 ± 0.01	0.02
W	0 ± 0.01	-0.01 ± 0.01	0.01 ± 0.01	0.02

Table 4.1: The values used to compute the core shift analysis. x_{pos} and y_{pos} represent the peak position of the map in [mas]; r represent the distance from the reference point in [mas]; Pixelsize represent the size of the pixel in [mas]. The errors on the parameters are taken as half of the pixel size for each bands.

In the Fig. 4.1 it is possible to observe that the best fit between the distance from the core and the frequencies gives $r \propto \nu^{-1.20 \pm 0.18}$, in agreement with the literature. The fit have been performed with the scipy module `curve_fit`[1], taking into account the errors. The error on k have been estimated as the square root of the diagonal elements of the covariance matrix produced with the same scipy module. It is notable that the fit performed without considering the errors on r, gives $r \propto \nu^{-1.02 \pm 0.17}$, that is even more close to the theoretical value. It is also possible to notice that the Q band seems to be a little lower than expected from the fit, considering the estimated error.

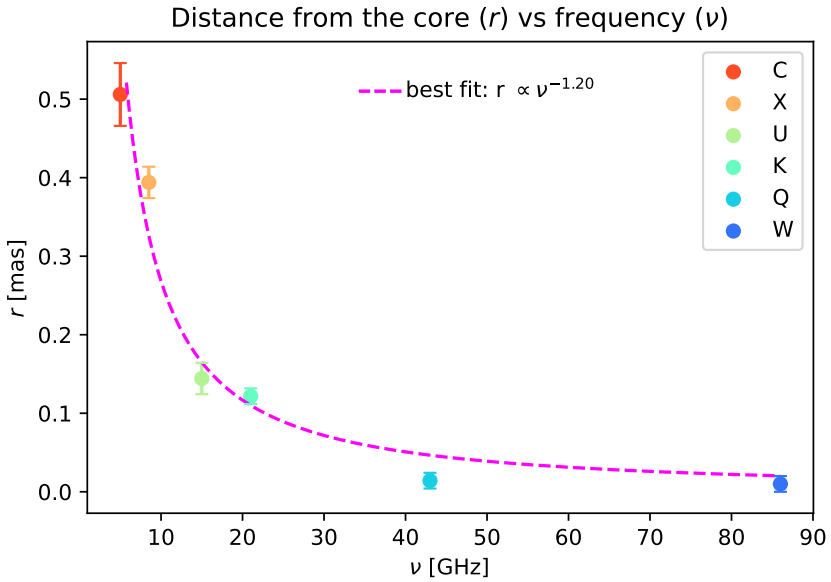

Figure 4.1: The core shift effect on 3C111. The best fit line is plotted in magenta. The errors have been estimated as half of the pixel size for each map as explained in (4.2)

[1] `https://docs.scipy.org/doc/scipy/reference/generated/scipy.optimize.curve_fit.html`

4.2 Spectral index maps

As stated in the 1.6.1, the emission in the radio domain, comes from the synchrotron process. Since $F(\nu) \propto \nu^{\alpha}$, the spectral index between two frequencies is:

$$\alpha = \frac{\log \frac{F(\nu_2)}{F(\nu_1)}}{\log \frac{\nu_2}{\nu_1}} \tag{4.3}$$

where ν_1 and ν_2 are the two observing frequencies and $F(\nu_1)$ and $F(\nu_2)$ the relative flux densities.

With such a large coverage in frequency with the same instrument and therefore, same baseline lengths, it is not possible (or it does make little sense, at least), to produce a single set of images with the same uv-range (in wavelength units), image sampling and resolution covering the whole range. Therefore, given the richness of features in 3C111, spectral index images were produced in frequency pairs. Table 4.2 shows the details of the spectral index images in Figs 4.3 through 4.7. At all frequencies the emission is dominated by the jet base, i.e. the core, while the various regions in the jet are detected at progressively outer distances with wavelength. The overall radio spectrum of 3C111 at the time of the observation is shown in Fig. 4.2, and it shows a turnover around 9 GHz.

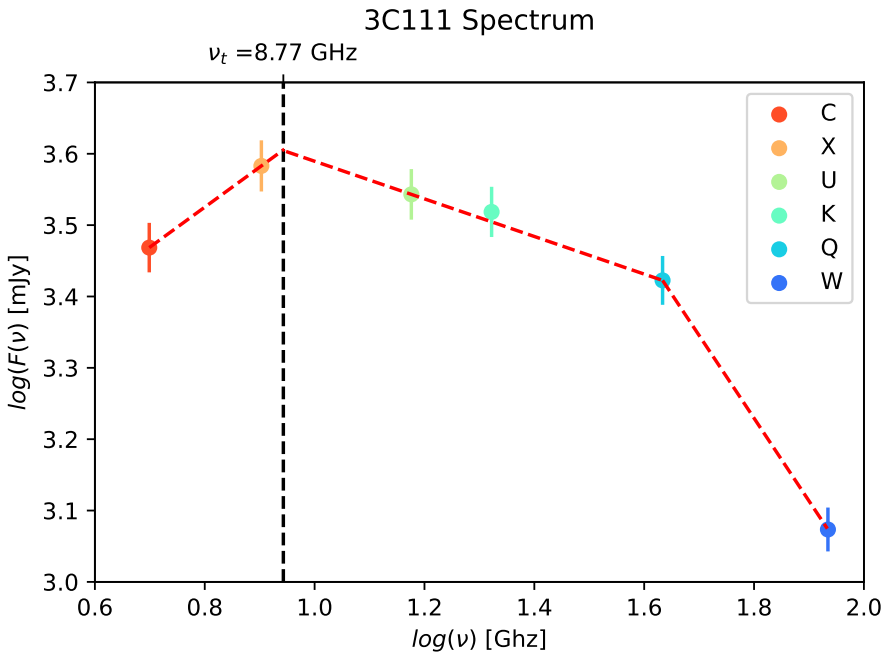

Figure 4.2: The spectrum of 3C111. The values represent the integrated values of the flux densities for each bands. The error associated with each point has been estimated as 10 % of the flux density.

However, more information can come from a spatially resolved study of the spectral index carried out on a pixel-by-pixel basis, as described below. In order

to compare two images at different bands, they need to be made with consistent parameters. These are the *uvrange* that is the range between the shorter baseline and the longer one, the size of the beam used to produce the map (*beamsize*), the size of the map (*mapsize*) and the size of the pixel (*pixelsize*). The values of these parameters are reported in the Table 4.2.

Bands	Uvrange [Mλ]	Beamsize [mas]	Mapsize [px]	Pixelsize [mas]
CX	4.06 - 146.25	1.9×1.9	2048	0.08
XU	7.54 - 245	1.1×1.1	2048	0.04
UK	11.14 - 441.5	0.6×0.6	2048	0.04
KQ	23.5 - 632	0.5×0.5	2048	0.02
QW	128.7 - 686	0.2×0.2	1024	0.02

Table 4.2: The chosen parameters to perform the spectral index maps. The values in each column are explained in the 4.2

Once the maps have been produced with these parameters, it was possible to analyse and compare the images. A Python script compares the images after a proper shift, computed to minimize artificial gradients across the jet, as result of separate (phase) calibration between the various bands. Therefore, after having applied the shift, it was possible to confront the values of the flux densities pixel by pixel to produce the spectral index maps. The estimate of the uncertainties has been calculated through the Eq. 4.4 that was computed according to the Theory of error propagation (Lindberg (2000)).

$$\alpha_{err} = \frac{1}{\log \dfrac{\nu_2}{\nu_1}} \sqrt{\left(\frac{\Delta F(\nu_1)}{F(\nu_1)}\right)^2 + \left(\frac{\Delta F(\nu_2)}{F(\nu_2)}\right)^2} \tag{4.4}$$

where $\Delta F(\nu)$ represent the error of the flux density that has been estimated as:

$$\Delta F(\nu) = \sqrt{(0.1F(\nu))^2 + rms^2} \tag{4.5}$$

where rms is the off-source rms of the map. The first term ($10\%F(\nu)$) is a conservative choice that represent the calibration error. This contribution dominates total error of $\Delta F(\nu)$. The spectral index maps are presented in the following pages along with their associated error maps.

Spectral index and error CX

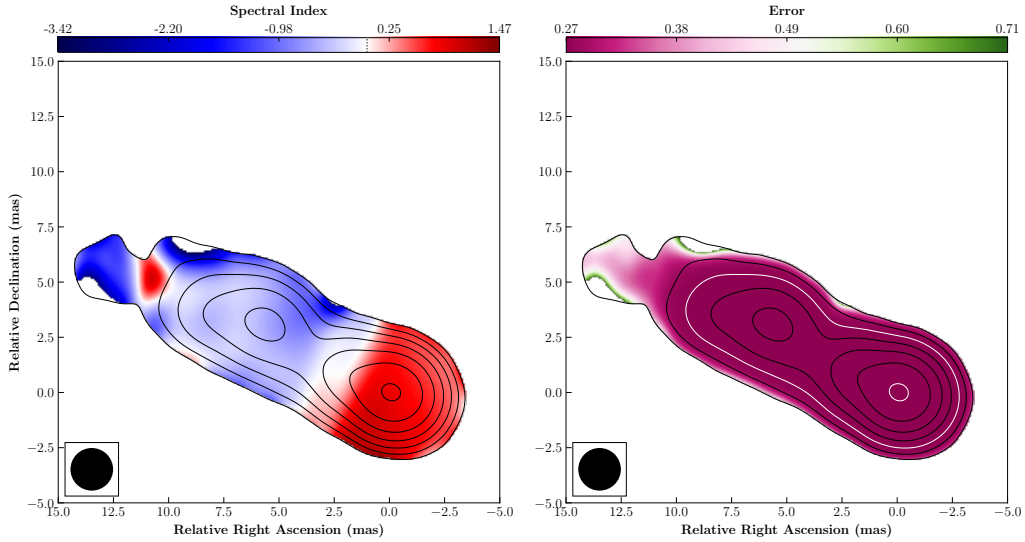

Figure 4.3: **Left:** Spectral index map between C band and X band. The value for the color change is 0. **Right:** Spectral index error map between C band and X band.

Spectral index and error XU

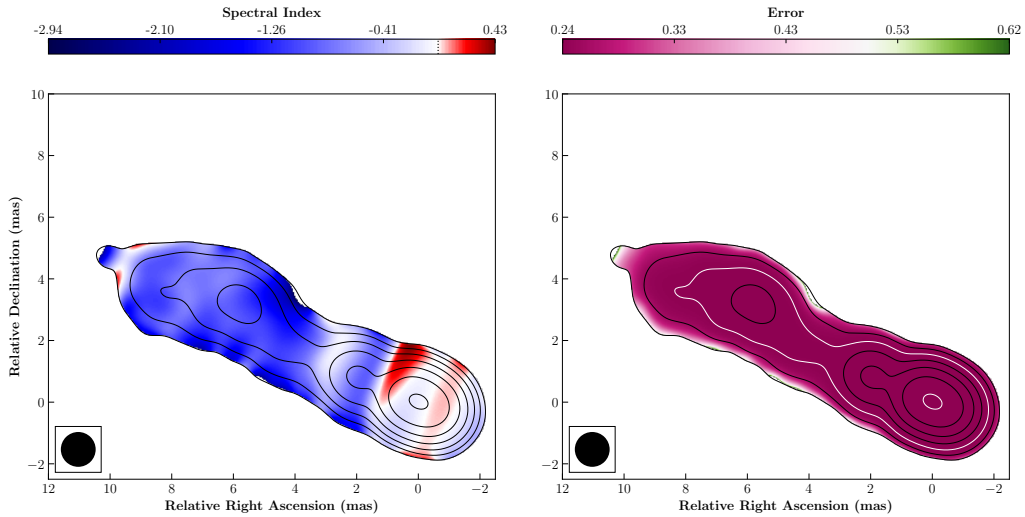

Figure 4.4: **Left:** Spectral index map between X band and U band. The value for the color change is 0. **Right:** Spectral index error map between X band and U band.

Spectral index and error UK

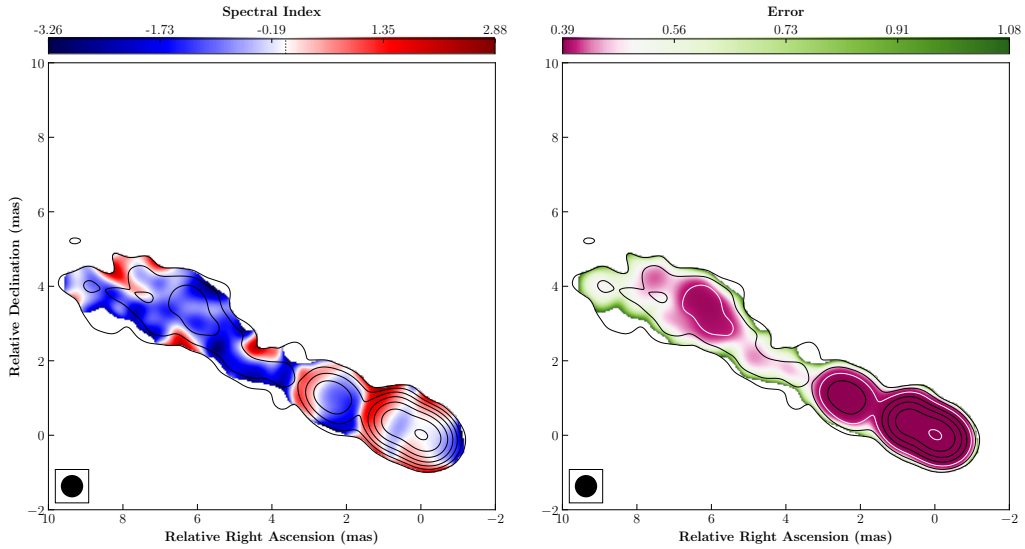

Figure 4.5: **Left:** Spectral index map between U band and K band. The value for the color change is 0. **Right:** Spectral index error map between U band and K band.

Spectral index and error KQ

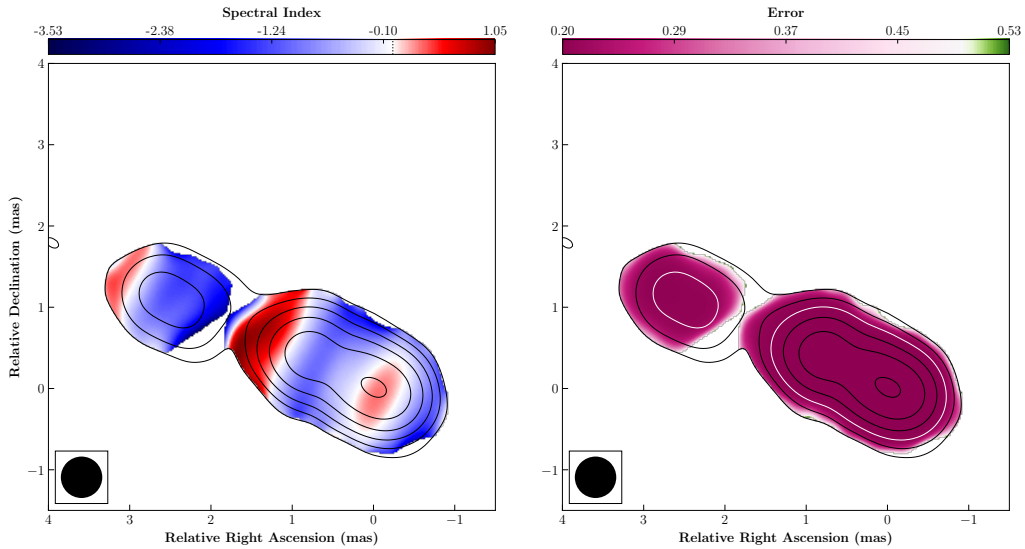

Figure 4.6: **Left:** Spectral index map between K band and Q band. The value for the color change is 0. **Right:** Spectral index error map between K band and Q band.

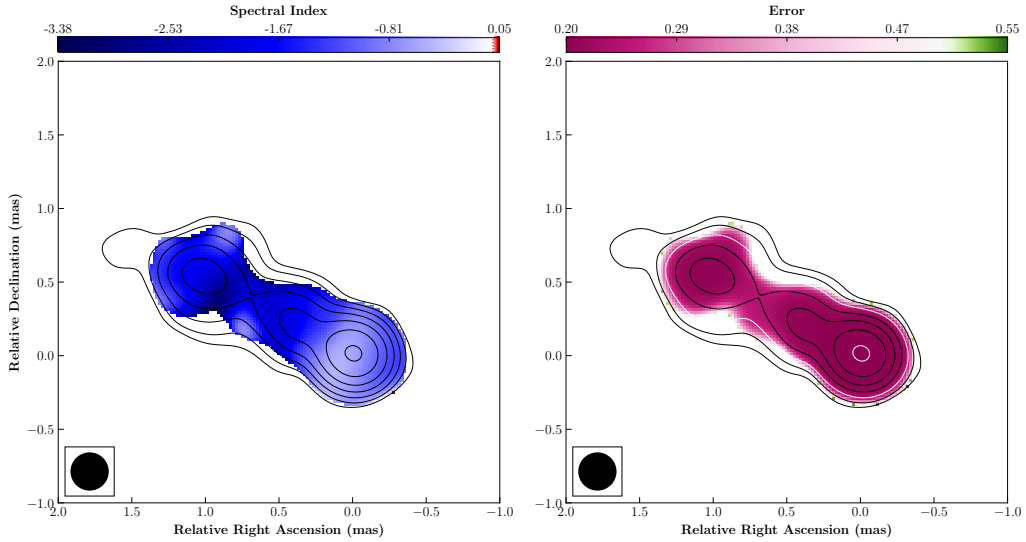

Figure 4.7: **Left:** Spectral index map between Q band and W band. The value for the color change is 0. **Right:** Spectral index error map between Q band and W band.

By looking at the spectral index maps, it is possible to notice some interesting features. For lower frequencies (4.3) the core region appears optically thick and the jet optically thin, within the errors. This is in agreement with the literature and with it has been stated in the 1.6.1. As a matter of fact, this property was found in many other jets (e.g. the one in the BL-Lac Mkr 501 Giroletti et al. (2004)). For higher frequencies the core starts to decrease its spectral index until it becomes optically thin (4.7). This is also in agreement with the literature (Jorstad et al. (2005)). In fact, the self-absorption regime, holds until the turn-over frequency (1.5) that, as stated before, is approximately $\nu_t \approx 9$ GHz. Therefore, it is expected that the core became more optically thin at higher frequencies. The spectral index along the jet is generally steep. When the same region appears in more than one frequency pair, there is clear evidence of a high frequency steepening, signature of radiative losses. This can be seen, for example for the region at ≈ 6 [mas] in R.A. and ≈ 3 [mas] in Dec. By looking at it in the CX spectral index map 4.3, it is possible to notice that the value of α oscillates around ≈ -0.5. As stated above, this value increases with the frequency and it becomes ≈ -1.25 for the XU spectral index map 4.4. A peculiar feature, that seems to be optically thick at almost all the frequencies, could be the component at ≈ 1.5 [mas] in R.A. and ≈ 0.5 [mas] in Dec. This can be seen in 4.6 and 4.5. However, in order to get a better understanding of this feature, more observations are required.

4.3 Rotation Measure maps

In order to describe the analysis performed in this section, it is mandatory to introduce the concept of the Faraday rotation.

4.3.1 Faraday rotation

In addition to the in-situ emission and self-absorption processes (1.6.1), the polarized radiation (2.3) can be further affected by electrons and magnetic fields embedded in external ionized gas. When a linearly polarized light passes through a magnetized medium with free electrons, the resulting polarization angle χ changes from the intrinsic angle χ_0 by:

$$\chi = \chi_0 + RM \times \lambda^2 \tag{4.6}$$

where λ is the wavelength and RM is the Rotation Measure:

$$RM = 8.1 \times 10^5 \int_0^L \left(\frac{n_e}{cm^{-3}}\right)\left(\frac{H_\parallel}{G}\right)\left(\frac{dl}{pc}\right) \ \ [\mathrm{rad/m^2}] \tag{4.7}$$

where n_e is the electron density, $B_\parallel$ is the magnetic field component (of the intervening medium) along line of sight and L is the distance between the source and the observer. One of useful applications of the Faraday rotation analysis is to understand the nature of the foreground medium of linearly polarized emission. The regions that cause the EVPA rotation are called *Faraday screens*. These foregrounds could be accretion flows, disk winds, or any interstellar medium between the background source and observer. The external Faraday rotation not only changes the apparent EVPA but may also decrease the fractional linear polarization. If the Faraday screen is inhomogeneous (in terms of density and magnetic field), it can induce different amount of EVPA rotations for different light rays of the same intrinsic linear polarization but passing through the screen in slightly different directions. Therefore, if the spatial RM structure in the screen is unresolved by the observing resolution, the net polarization is decreased (thus larger depolarization for larger inhomogeneity and poorer angular resolution). In addition, it is important to note that source-intrinsic Faraday rotation can occur within the jet plasma. Also, the geometry of the external screens could be complex. In this case, the observed EVPAs may not follow the λ^2 dependence and the resulting polarization patterns are generally complicated.

4.3.2 Producing the maps

After the EVPAs calibration (3.3.3), it was possible to study the rotation measure. In order to do that, the maps had to be confronted in groups of three. As already stated in the 4.2, the maps must have the same discussed parameters.

The UKQ RM image

Since the calibration of the EVPAs was possible (without other assumptions, as it will be discussed later on) only in the U,K and Q bands, these are the only three frequencies for which it was possible to compute the most reliable RM maps. For these bands, the values of the parameters are: *uvrange* $= 23.5 - 441.5$ Mλ , *beamsize* $= 0.4 \times 0.4$ mas^2, *mapsize* $= 2048$ px and *pixelsize* $= 0.04$ mas. After that, it was possible to cross correlate the images in pairs to determine the shifts to apply to the U and K bands in order to maximize the cross-correlation between the three

images. Through a python script it was therefore possible to produce the RM map (and its uncertainties) for the UKQ bands 4.8. The RM was calculated with the python module `linfit` [2] in the following way. For each pair of points in the plot $EVPAs$ rotation vs λ^2, the script calculates the line between the two values and takes that as a model. After that, it fits the third point with the previous model and it calculates the χ^2. This is done for all the three pairs and the selected line is the one with the lowest value of the χ^2. The RM value is the slope of this line (4.7). For what concerns the estimated uncertainties in the fitting parameters, these are obtained by taking the square roots of the diagonal elements of the covariance matrix. The covariance matrix is a 2x2 symmetric matrix where the diagonal elements are the variance of the fitting parameters. Their square roots provide estimates of the uncertainties in the fitting parameters. The off-diagonal elements are equal and give the cross correlation between the two fitting parameters 'a' and 'b'. In the case studied here, the variance for each EVPA value is computed as follow:

$$\sigma_{EVPA} = \sqrt{\sigma_{rms}^2 + \sigma_{cal}^2} \text{ where: } \sigma_{rms} = \frac{\sqrt{Q^2\sigma_Q^2 + U^2\sigma_U^2}}{2(Q^2+U^2)} \text{ and } \sigma_{cal} = 5°(\text{or } 0.087 \text{ rad}) \tag{4.8}$$

In the Eq. 4.8, there are various terms contributing to the uncertainties: Q and U are the values of the Stokes Q and Stokes U respectively, producing the EVPA through the Eq. 2.20; σ_Q and σ_U are the rms of the Stokes Q and Stokes U respectively; σ_{rms} is the uncertainty due to the noise of the U and Q maps and σ_{cal} is the calibration error, here taken as 5° (or 0.087 rad).

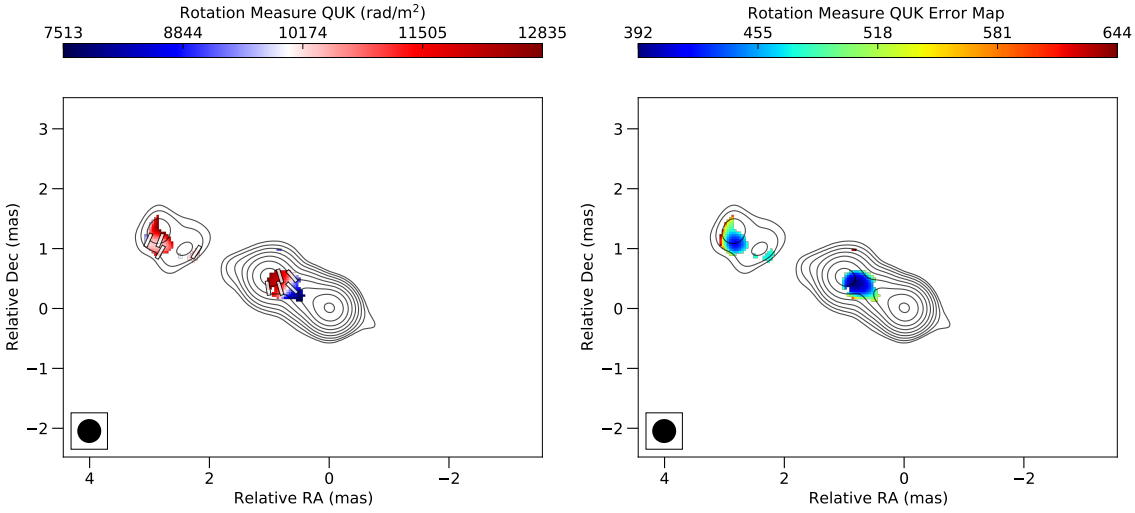

Figure 4.8: **Left:** Rotation measure map between U, K and Q bands, plotted on the Q contours. The white bars corresponds to the Faraday-corrected EVPAs. **Right:** Rotation measure error map between U, K and Q bands, plotted on the Q contours.

The UKQ polarization images are sensitive to the inner portion of the jet, out to about 3 mas ($\approx 3pc$) from the core. Two regions can be clearly seen: the brightest is at about 1 mas and shows values from $\approx$ 7500 to $\approx$ 12500 [rad/m^2]. It is in between the two brightest components visible in the total intensity emission. It

[2]linfit documentation : `https://github.com/djpine/linfit/blob/master/linfit.py`

also corresponds to a location with inverted spectrum emission 4.2. This could be consistent with the presence of substantial amount of external magnetised plasma responsible for both Faraday rotation and free-free absorption. The magnetic field orientation is almost perpendicular to the jet axis in the inner part and it is titled to $\approx 60°$ with the jet axes in the outer part. At a distance of about 3 mas, there are two additional regions with RM values from $\approx$ 10000 to $\approx$ 12500 [rad/m^2]. Here the the magnetic field seem to start to be aligned to the jet axis.
In addition to the previous uncertainties, it was also performed a more rough (but more easy to understand) way to get these values. This second method simply takes the minimum and maximum values of the RM and then it adds or subtracts σ_{cal} to the correspondent EVPAs rotation value as shown in the Fig. 4.9. By comparing these two different methods, it is possible to see that the RM uncertainties are similar to each other.

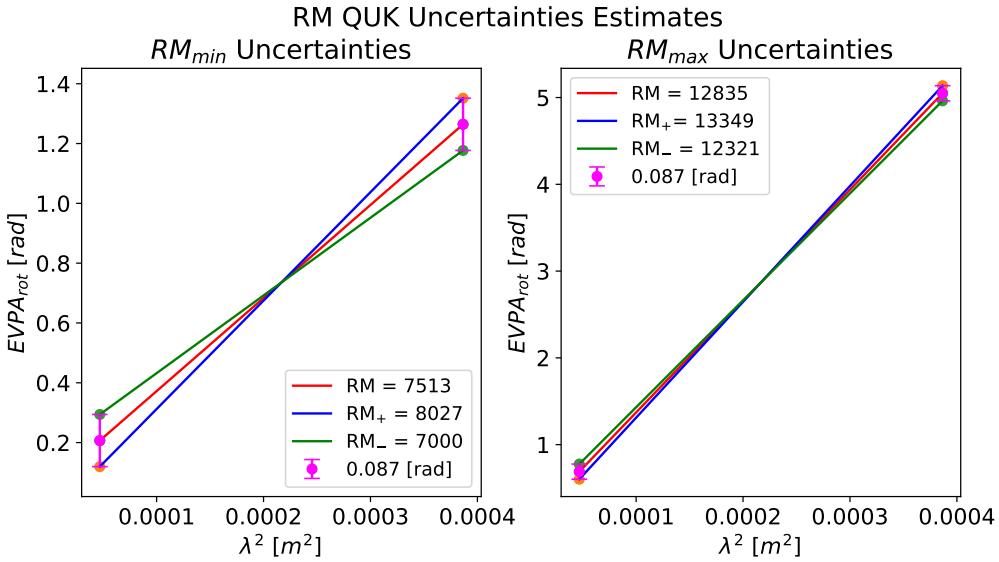

Figure 4.9: **Left:** Estimated uncertainties for the minimum value of RM (7513 rad/m^2) between U, K and Q bands. The value is taken from 4.8 and it is plotted in red. The blue line represent the value of the RM calculated by subtracting 5° to the lower value of the EVPAs rotation and by adding 5° to the higher value of the EVPAs rotation. The green line represent the value of the RM calculated by adding 5° to the lower value of the EVPAs rotation and by subtracting 5° to the higher value of the EVPAs rotation. **Right:** Estimated uncertainties for the minimum value of RM (12835 rad/m^2) between U, K and Q bands. The value is taken from 4.8 and it is plotted in red. The blue line represent the value of the RM calculated by subtracting 5° to the lower value of the EVPAs rotation and by adding 5° to the higher value of the EVPAs rotation. The green line represent the value of the RM calculated by adding 5° to the lower value of the EVPAs rotation and by subtracting 5° to the higher value of the EVPAs rotation.

The values of the RM are actually a bit high, but this can be associated with the fact that the same EVPAs can have different values. More specifically, a rotation of 2π maintain the same angle but it is computed as a different value.

The CXU RM image

The lowest frequencies sample the outer part of the jet emission and the image is presented in the Fig. 4.10. This image was obtained thanks to the EVPA calibration through single dish observations from the FGAMMA program (Myserlis (2015)). The calibrated values are $-33°$ for the C band and $-14°$ for the X band. However, since the single dish observations cannot resolve extended sources, these integrated values have to be handled carefully. Therefore, the main assumption is that these integrated values are a good estimates of the EVPAs orientation of the integrated emission of the source. With this important premise in mind, by looking at the polarization maps in the C (3.11), the X (3.12) and U (3.13) bands, it is possible to recognize a similar structure at at ≈ 6 mas from the core. Therefore, with the same process explained before, the RM map for the UCX bands have been computed, with the associated error map (Fig. 4.10).

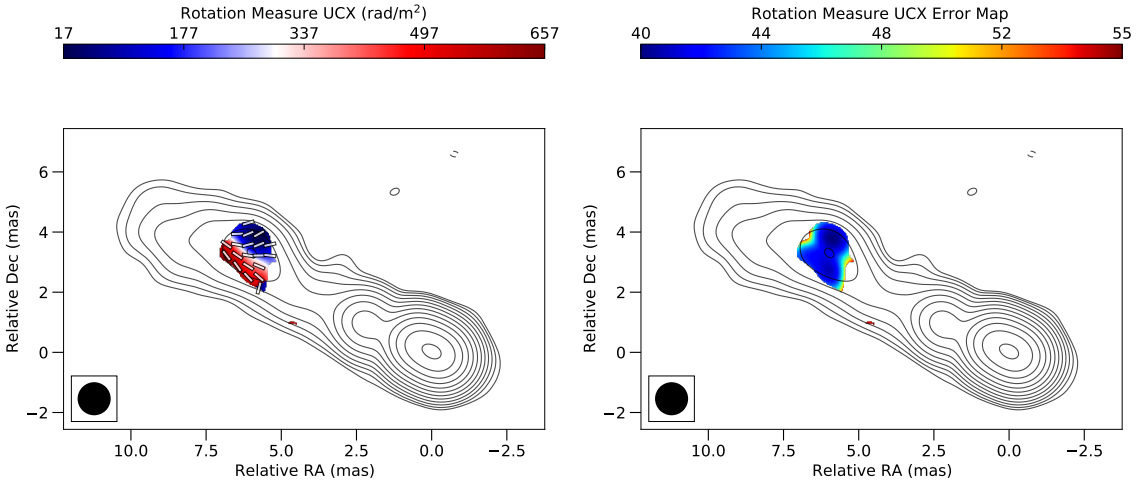

Figure 4.10: **Left:** Rotation measure map between C, X and U bands, plotted on the U contours. The white bars corresponds to the Faraday-corrected EVPAs. **Right:** Rotation measure error map between C, X and U bands, plotted on the U contours.

At these frequencies, the only region with common polarised emission sits at a distance of about 6 mas from the core, corresponding to a peak in the total intensity emission. Here, the RM detected is nearly two orders of magnitude smaller than in the inner region, which turns out to be completely depolarized, likely by diffrential Faraday rotation not resolved by the present observation. This is consistent with the high RM values found in the previous section. There is a significant gradient of RM across the jet structure, going from about $650\,\mathrm{rad/m^2}$ on the SE limb down to about $50\,\mathrm{rad/m^2}$. The magnetic field orientation is almost perpendicular to the jet axis in the SE limb and it is titled in the NO limb making it almost parallel to the jet axis. It can be clearly see that there is a gradient of orientation of the magnetic field in this region. This disposition is very similar to the one that should have an helical magnetic field, as predicted by the simulations in Fuentes et al. (2021). Therefore, if the assumption that the single dish observations could provide a good EVPA calibration, this result could prove that in this region of 3C111, the magnetic field is helical. In addition to that, as for the QUK bands, the uncertainties have

been estimated also with the method of adding and subtracting σ_{cal} to the EVPA rotation (Fig. 4.11).

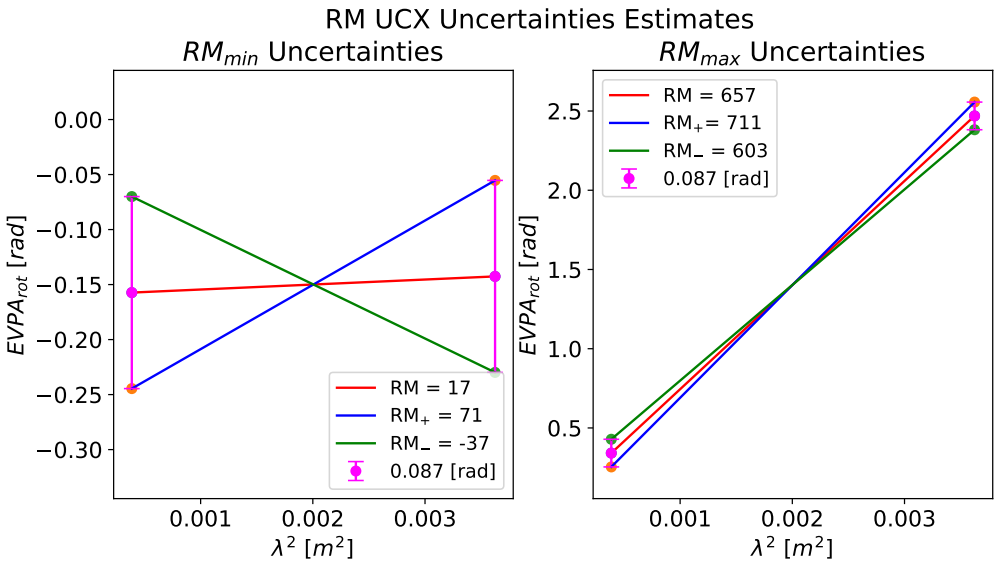

Figure 4.11: **Left:** Estimated uncertainties for the minimum value of RM (17 rad/m^2) between C, X and U bands. The value is taken from 4.8 and it is plotted in red. The blue line represent the value of the RM calculated by subtracting 5° to the lower value of the EVPAs rotation and by adding 5° to the higher value of the EVPAs rotation. The green line represent the value of the RM calculated by adding 5° to the lower value of the EVPAs rotation and by subtracting 5° to the higher value of the EVPAs rotation. **Right:** Estimated uncertainties for the minimum value of RM (657 rad/m^2) between C, X and U bands. The value is taken from 4.8 and it is plotted in red. The blue line represent the value of the RM calculated by subtracting 5° to the lower value of the EVPAs rotation and by adding 5° to the higher value of the EVPAs rotation. The green line represent the value of the RM calculated by adding 5° to the lower value of the EVPAs rotation and by subtracting 5° to the higher value of the EVPAs rotation.

4.4 Model fitting of the brightness distribution

The analysis of radio images takes advantage of a techinque termed **model-fitting** in which the source structure is interpreted in terms of a (small) number of individual (Gaussian) components, each characterized by position, 2-D size, orientation, and flux density. The model created by an iterative process, is then convolved with the observing beam and then subtracted out from the real image. In case the fit is good, the residual image should show just noise. The source component parameters are made to vary until a convergence is achieved, based on the least square differences (between real image and model). In general, in the analysis of multi-frequency images, it is also possible to assign fixed parameters to a given component. For example, it is possible to let only the flux density vary, in order to make spectral index comparisons. Real sources are more complicated and often the model has to be adapted to each image. However, the modelfitting allows to recognize the

same components at different frequencies and so to confront them (see Sect. 4.4.2). Since the images strongly depend on the beam shape, it could be very difficult to recognize the same structure at various frequencies. Therefore, even though it does not correspond to the real expected shape, all the components are assumed to be circular. In addition to that, the circle is more stable when performing the fit. That said, the modelfit was performed with `difmap` in the following way:

- Select the calibrated image.
- Through the graphical interface, select the position and size of a component.
- Perform the fitting of the model with the selected components.
- Check the residuals and the value of the reduced χ^2 and, if necessary add other components.
- When the residuals show only noise and the reduced χ^2 is low enough (i.e. ≈ 1), save the model.

The fitting variables are: the flux density $F(\nu)$, the angular size of the component θ (that is the FWHM of the 2-D Gaussian), the distance from the core r, the position angle from the core Φ and the axial ratio (that, since all the components are circular, it is always equal to 1). It is possible to impose that some of these values do not vary. This was done whenever the size of a component was smaller than 1/10 of the minor axis of the beam. The size was therefore fixed to 1/10 of the minor axis of the beam. For what concerns the estimate of the uncertainties, since the nominal errors given by `difmap` were extremely low, they were computed in the following way. The error on the flux density was taken in the same way as the one of the spectral index maps Eq. (4.5). The uncertainties on the distance from the core (e.g. the position) and on the size of the components are taken with the formulas from Orienti et al. (2011). Namely, for the position, the uncertainties are estimated as:

$$\Delta r = \frac{\theta}{SNR} \text{ where } SNR = \frac{F(\nu)}{rms * \dfrac{\theta}{beam}} \tag{4.9}$$

where SNR is the signal-to-noise ratio and $beam$ is the area of the beam. However, if $SNR > 10$ the error is conservatively taken as 1/10 of the minor axis of the beam. For the component size, it has been taken a conservative error:

$$\Delta\theta = \frac{1}{10}\theta \tag{4.10}$$

The values for all the components with the associated uncertainties are reported in Tab. 4.3. Once the fitting was performed for each band, it was possible to plot the different components for each band on the associated contours. The contours are the one found during the cleaning. The components are plotted with a color scale based on the intensity and are presented in the following pages.

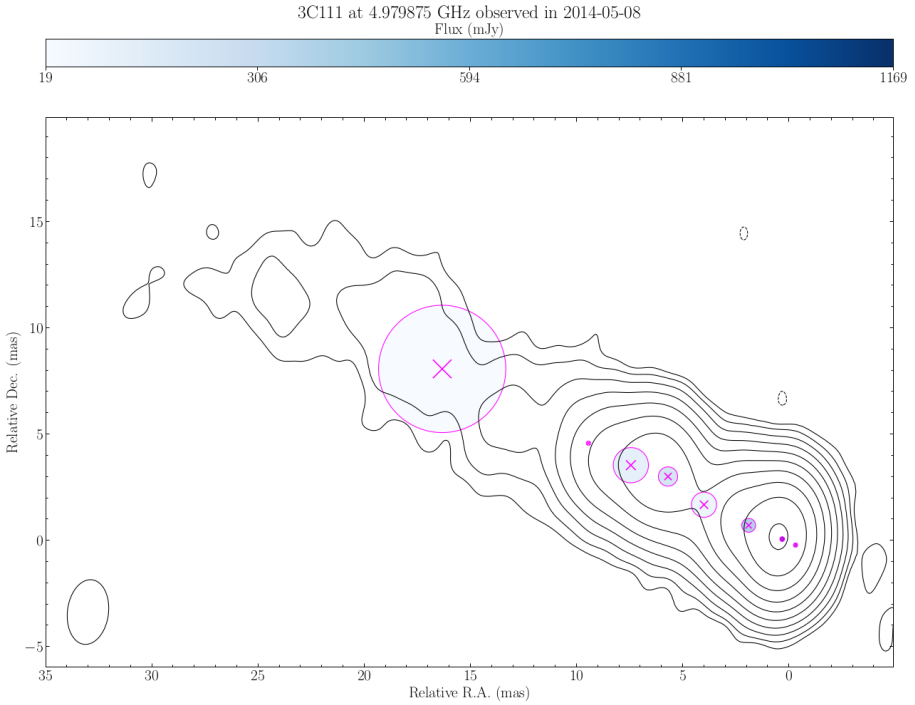

Figure 4.12: The 3C111 components map for the C band. The components are found with the `difmap` modelfitting. The contours and the beam sizes are the same as 3.2. The color scale represents the intensity of each component.

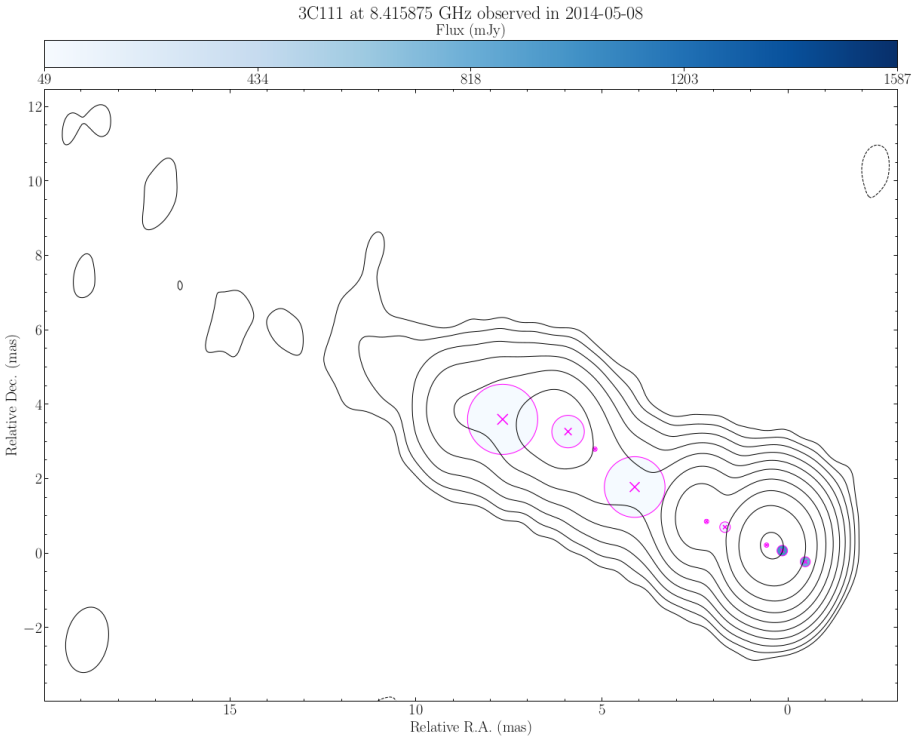

Figure 4.13: The 3C111 components map for the X band. The components are found with the `difmap` modelfitting. The contours and the beam sizes are the same as 3.3. The color scale represents the intensity of each component.

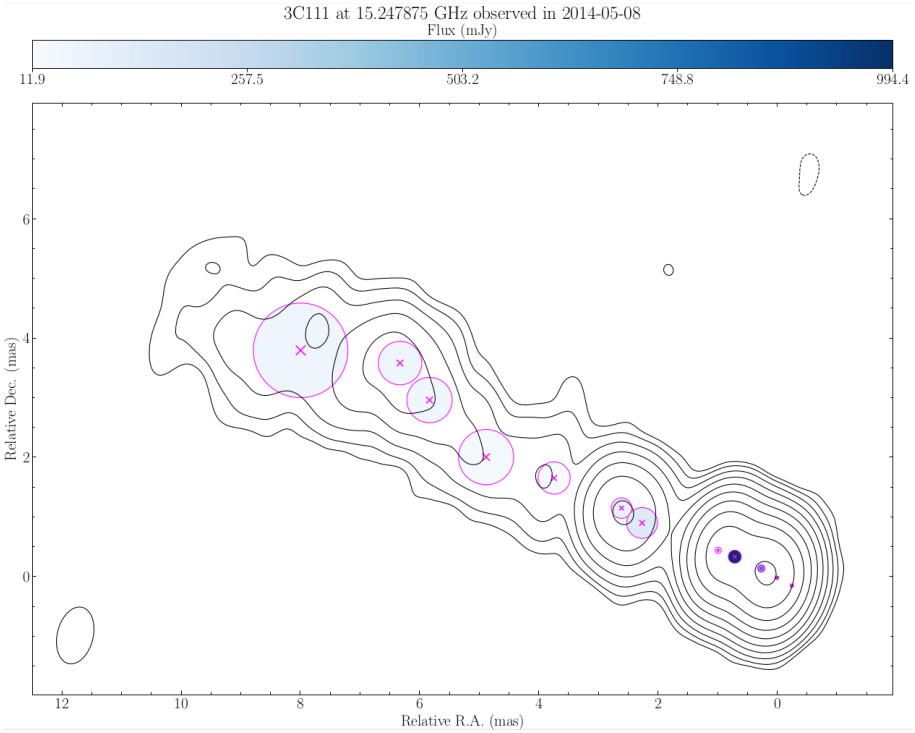

Figure 4.14: The 3C111 components map for the U band. The components are found with the `difmap` modelfitting. The contours and the beam sizes are the same as 3.4. The color scale represents the intensity of each component.

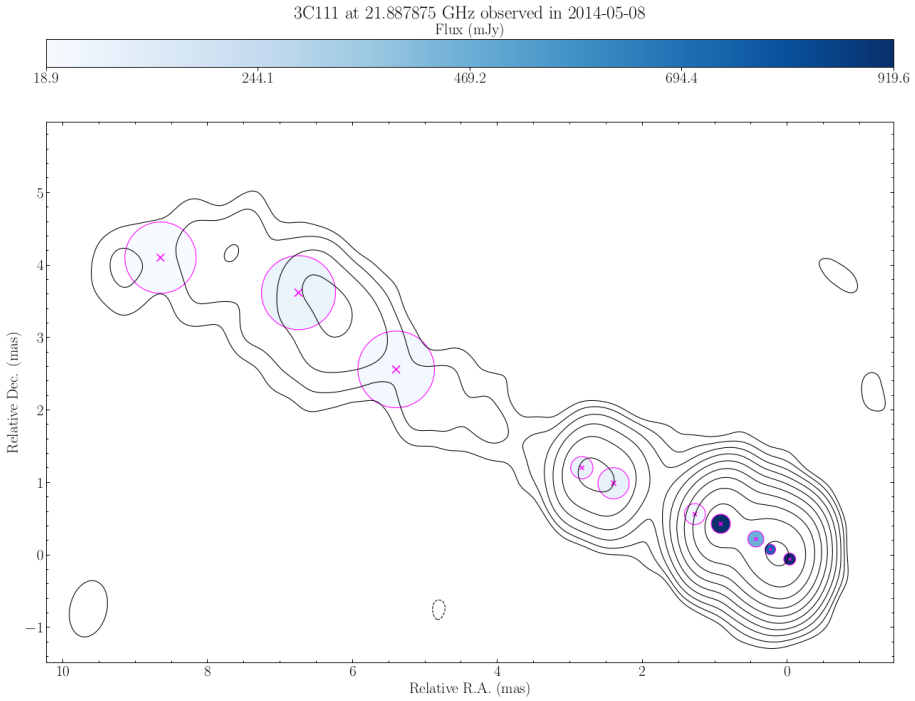

Figure 4.15: The 3C111 components map for the K band. The components are found with the `difmap` modelfitting. The contours and the beam sizes are the same as 3.5. The color scale represents the intensity of each component.

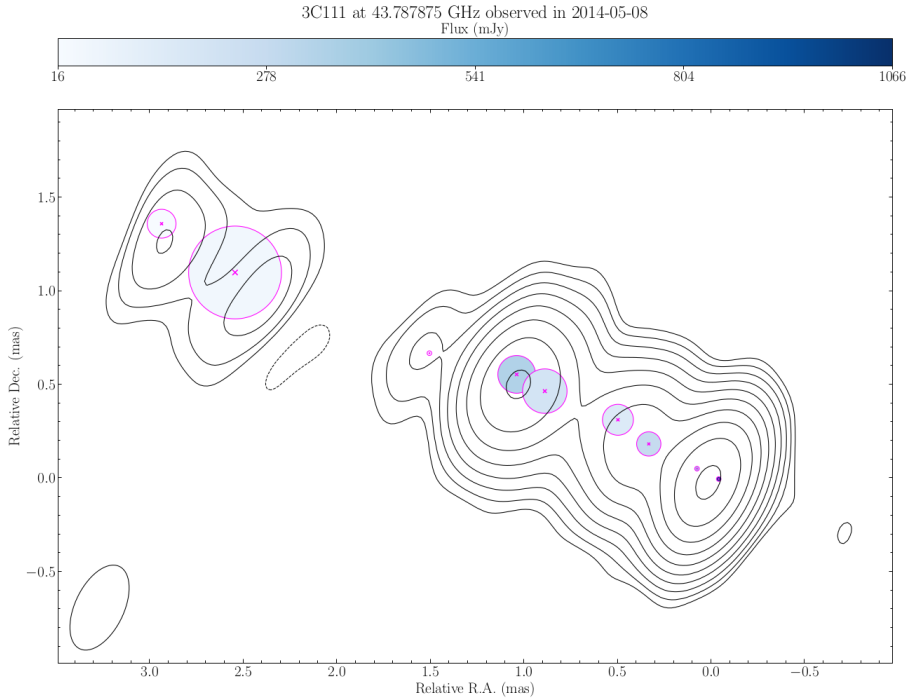

Figure 4.16: The 3C111 components map for the Q band. The components are found with the `difmap` modelfitting. The contours and the beam sizes are the same as 3.6. The color scale represents the intensity of each component.

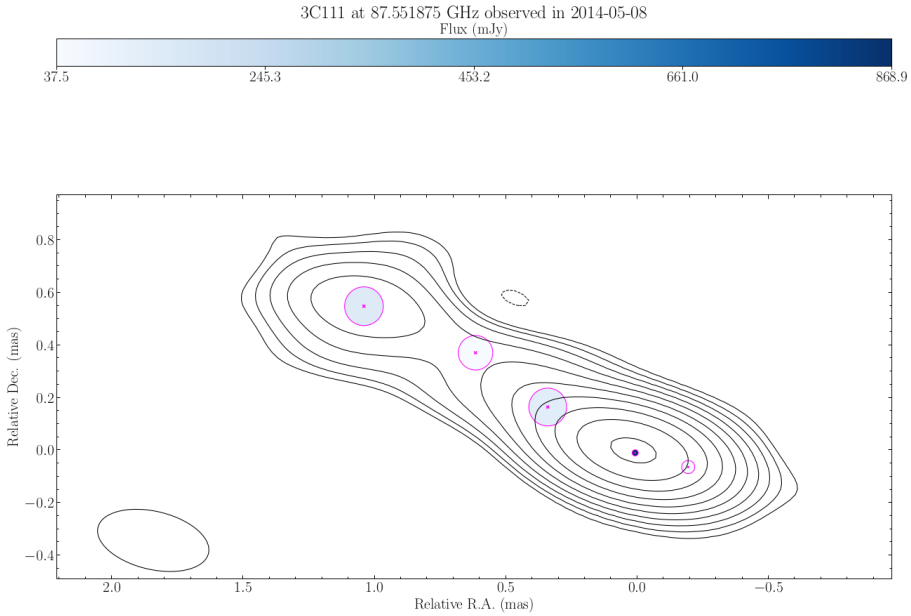

Figure 4.17: The 3C111 components map for the W band. The components are found with the `difmap` modelfitting. The contours and the beam sizes are the same as 3.7. The color scale represents the intensity of each component.

In order to have a comprehensive view of the various components found at the various frequencies, all the circular Gaussian found are represented in Fig. 4.18, shown on the contours of the C band image. Two insets have been added, zooming

on the central (contours from K band) and inner (contours from Q band) part of the jet. Components at the various frequencies are represented with different colors: the coding ranges from reddish (C and X band) through greenish (U, K) to bluish (Q,W). The position of all the components are corrected for the core shift.

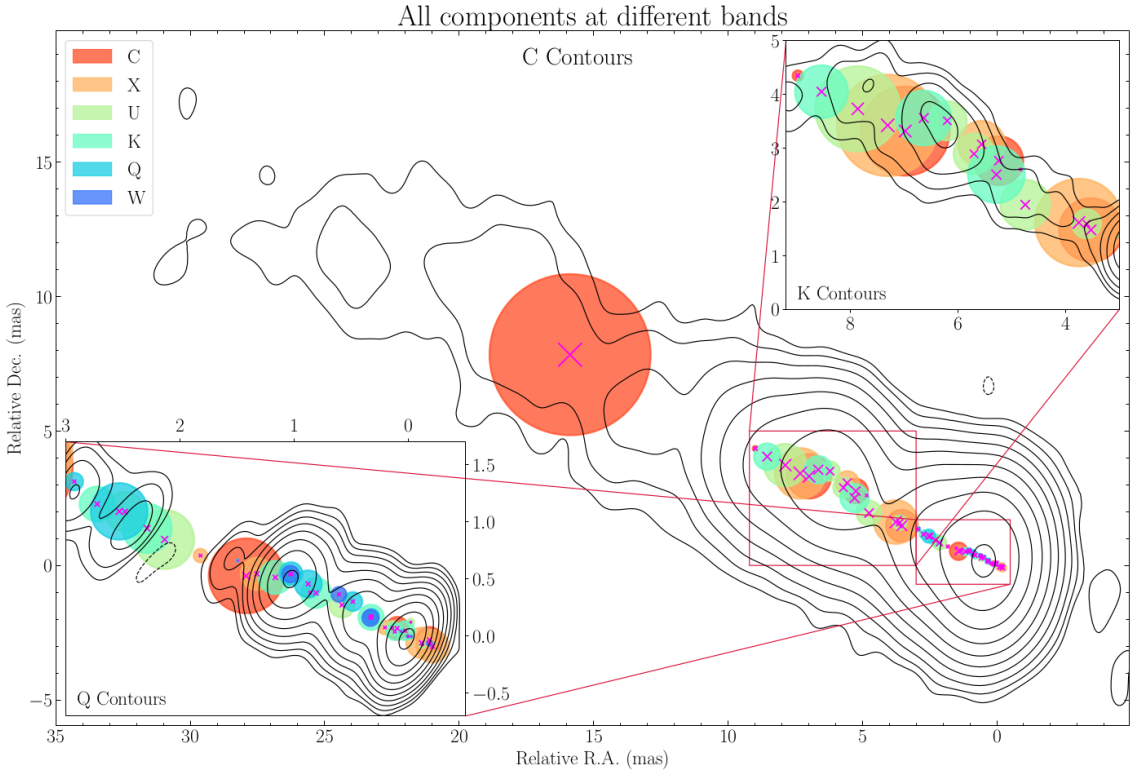

Figure 4.18: All the components of 3C111, plotted over the C contours (3.2). The components for each bands are represented by the colour in the legend. In the upper right panel it is represented the region between 9 and 2 mas in Right Ascension and 0 and 5 in Declination. The contours are the one of the K band (3.5). In the lower left panel, it is represented the region between -0.5 and 3 mas in Right Ascension and -0.7 and 1.7 in Declination. The contours are the one of the Q band (3.6).

Fig. 4.18, shows that some components are found in more than one band. This permits to analyse their characteristics and see how the quantities vary with the frequencies (e.g. in 4.24). Moreover, it has been possible to produce a plot to see how the distance from the core r scales with the size of the component θ. By looking at the plot Fig. 4.19, it is possible to see that for smaller size and distance from the core, the scatter increases.

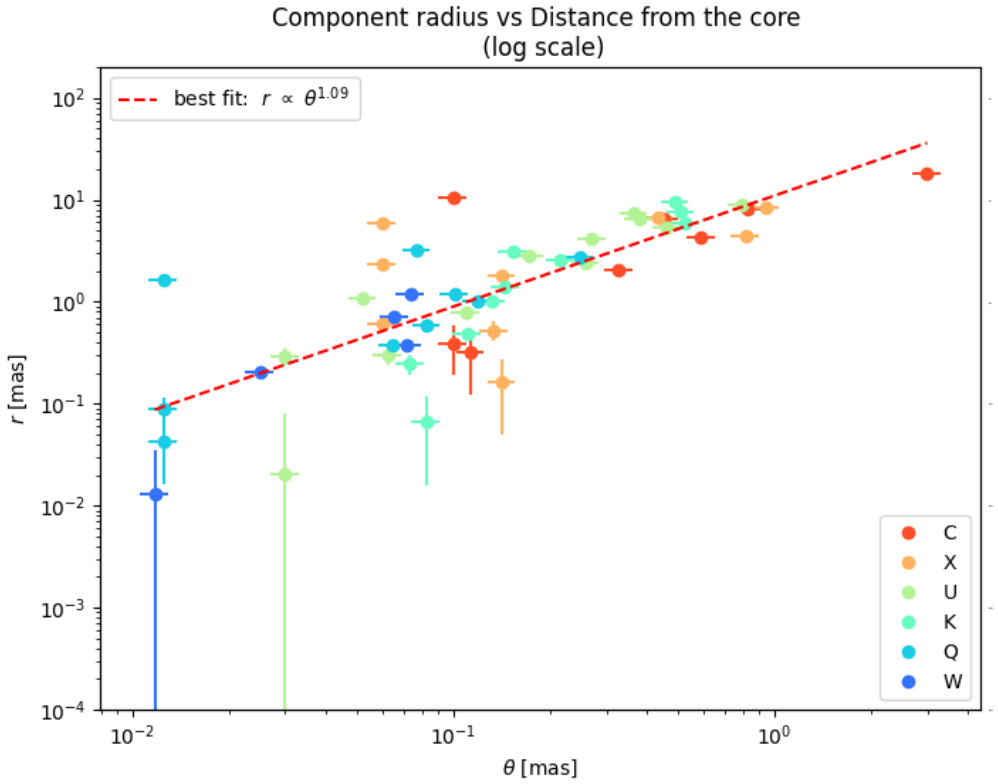

Figure 4.19: Distance from the core r in [mas] vs the size of the component θ in [mas] in logarithmic scale. The error bar represents the uncertainties computed as explained in 4.4. The red dashed line represent the best fit for the data points, estimated with the model equation $y = ax+b$. The different colors represent different bands components as can be seen from the legend.

A linear fit was performed. The model equation chosen to fit the data was $y = ax + b$, since on the log scale, the expected trend is linear. As can be seen from the legend, the best fit is obtain for $r \propto \theta^{\sim 1}$. Therefore, it can be deducted that larger components usually lie at increasing distance from the core. It is important to notice that some error bars looks really large (e.g. the errors on the W component at $r \approx 10^{-2}$ mas and $\theta \approx 10^{-2}$ mas). This can be understood by looking at the values in the Tab. 4.3. In fact if one subtracts the error from the position, the component lies at a negative distance (e.g. on the right with respect to the core). This, in the logarithmic scale, makes the error bar to $-\infty$.

4.4.1 Brightness temperature estimate

As stated in the Sect. 1.6.2, even though the brightness temperature T_B do not strictly correspond to the effective temperature for a non thermal emitting source such as 3C111, it could still give an idea of its value, since it is the temperature that a black body would have in order to emit its radiation at that temperature. In beamed sources, the brightness temperature estimate is related also to the jet velocity (1.14) and therefore, its value must take into account the Doppler factor δ.

Keeping in mind these caveats, it is possible to estimate the observed T_B for each component using the Eq. (4.11):

$$T_B \approx 1.22 \times 10^{12} \frac{F(\nu)}{\theta^2 \nu^2}(1+z) \text{ [K]} \tag{4.11}$$

where $F(\nu)$ is the flux density of the component in [Jy], θ is its angular size in [mas], ν is the observing frequency in [GHz] and z is the redshift ($= 0.048$). Eq. (4.11) is taken from Gómez et al. (2022) and represent the observed brightness temperature of the component. Unfortunately, since the observations were made in only one epoch it was not possible to estimate the jet velocity and thus calculates the intrinsic value of T_B. Nonetheless, a possible way to overcome this problem is to take the value from the literature. In Beuchert et al. (2018), the authors gave a lower limit to the 3C111 jet velocity of $v_j \approx 0.976c$. However, since the last observation they analysed was approximately two years apart from the one studied in this work, since 3C111 has been proven to have a variable activity and since each component could have different velocities, the estimate of the intrinsic T_B has not been performed. For what concerns the estimate of the uncertainties, they were computed thanks to the Theory of error propagation (Lindberg (2000)). The resulting equation is therefore:

$$\Delta T_B = T_B \sqrt{\left(\frac{\Delta F(\nu)}{F(\nu)}\right)^2 + \left(\frac{2\Delta\theta}{\theta}\right)^2} \tag{4.12}$$

The brightness temperature values with the associated uncertainties can be found in Tab. 4.3.

T_B relations

Once the T_B has been computed for all the components, it was possible to see if whether there is a correlation with some parameters. The first physical quantities that have been analysed are the T_B and the distance from the core r (Fig. 4.20). In addition to that, a linear fit was performed. The model equation chosen to fit the data was $y = ax + b$, since on the log scale, the expected trend is supposed to be linear.

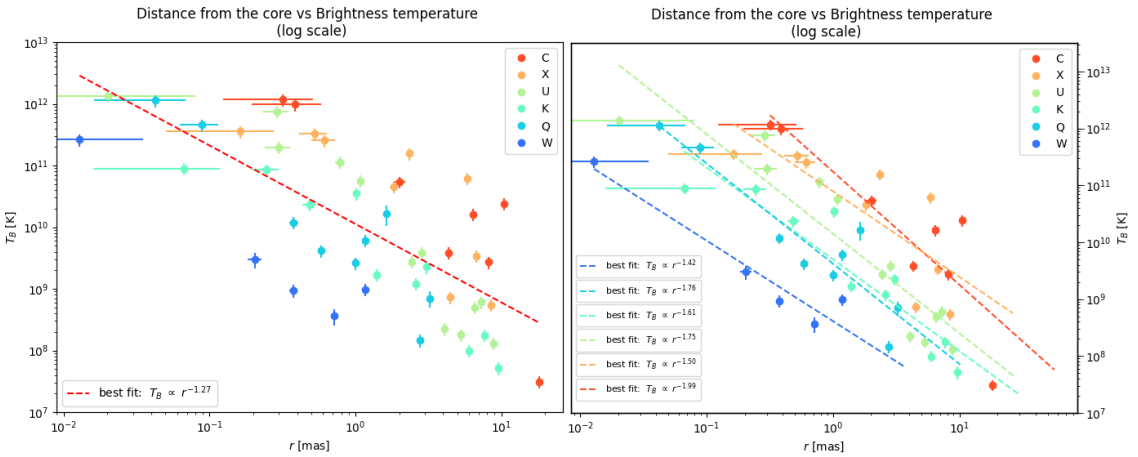

Figure 4.20: **Left:** The brightness temperature T_B in [K] vs the distance from the core r in [mas] in logarithmic scale. The error bar represents the uncertainties computed as explained in 4.4 and 4.4.1. The red dashed line represent the best fit for the data points, estimated with the model equation $y = ax + b$. The different colors represent different bands as can be seen from the legend. **Right:** The same plot as the left one. The dashed lines represent the best fit for the data points of each band, estimated with the model equation $y = ax + b$.

From Fig. 4.20 it is possible to see that there seems to be a correlation. In fact, from the right panel, it can be seen that the temperature has a similar trend for all frequencies. More specifically, the best fit values reported in the bottom left corner, suggest that the mean value of the exponent (namely a) is ≈ -1.67 that roughly corresponds to 5/3. The fits have some outliers that seems to be more distant from the fit at lower frequencies (e.g. the C component at $r \approx 10^2$ mas and $T_B \approx 10^{7.2}$ K). Therefore, more observations would be required in order to understand if this relation is reliable.
With the same logic as before, it was possible to plot the T_B as a function of the angular size of the component θ. This is shown in the Fig. 4.21. Also for these quantities, a linear fit was performed. The model equation chosen to fit the data was again $y = ax + b$, since on the log scale, the expected trend is supposed to be linear.

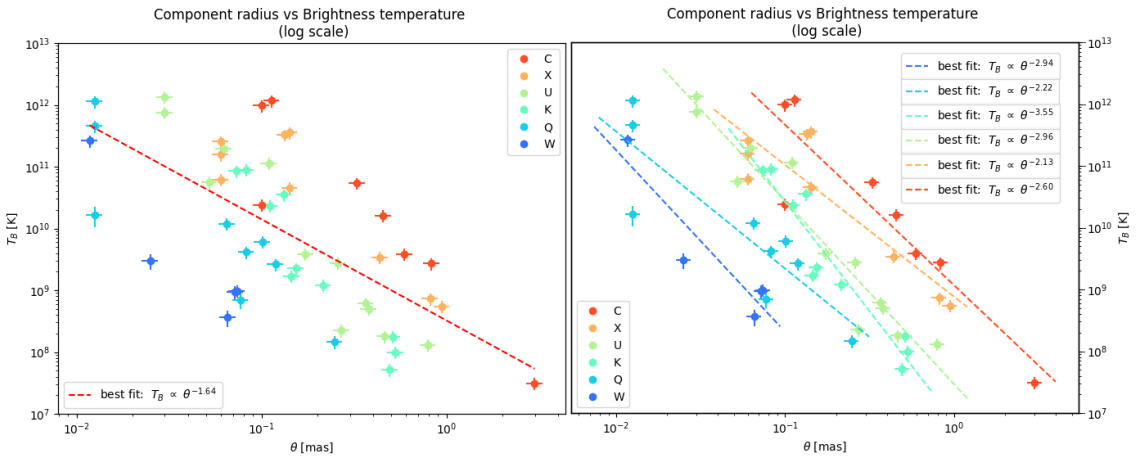

Figure 4.21: **Left:** The brightness temperature T_B in [K] vs the size of the components θ in [mas] in logarithmic scale. The error bar represents the uncertainties computed as explained in 4.4 and 4.4.1. The red dashed line represent the best fit for the data points, estimated with the model equation $y = ax + b$. The different colors represent different bands components as can be seen from the legend. **Right:** The same plot as the left one. The dashed lines represent the best fit for the data points of each band, estimated with the model equation $y = ax + b$.

As for the previous plot, the fitting was performed both for all the components and for the components at each bands. By looking at the right panel in the Fig. 4.21, it is possible to see that the values of the exponents spans from ≈ -2.13 and ≈ -3.55. Therefore, even though the mean value is ≈ -2.73, there does not seem to be a strong correlation between T_B and θ, for the dataset used in this work. However, this needs to be verified with further studies. Moreover, as expected from the literature, it is possible to see that the components with the highest brightness temperature are the one closer to the core and with the smaller angular size for each bands.

4.4.2 Magnetic field estimate

As stated in 1.6.1, it is possible to have an estimate of the magnetic field, under the assumption that the emitting region is at the minimum total energy (i.e. equipartion state). Therefore, it has been computed the value of the magnetic field of equipartition H_{eq} for each component. This was done through the Eq. 1.8 by assuming a spherical geometry with a filling factor of unity (i.e. the source volume is fully and homogeneously filled with relativistic plasma) and proton and electron energies were assumed to be equal. Therefore the formula used to compute H_{eq} is:

$$H_{eq} = \left(\frac{3}{4}\frac{L}{V}\right)^{\frac{2}{7}} \times 10^4 \ \text{mG} \tag{4.13}$$

where L and V were computed as follow:

$$L = 4\pi \left(\frac{F(\nu)}{\text{ergs}^{-1}\text{Hz}^{-1}}\right) D_L \left(\frac{\nu}{\text{Hz}}\right) \ \text{erg/s}; \ V = \frac{4}{3}\pi \left(\frac{\theta}{\text{rad}} D_L\right)^3 \ \text{rad}^3 \tag{4.14}$$

where D_L is the luminosity distance at $z = 0.048$, computed through the Ned Wright's cosmological calculator[3], and is equal to $\approx 214\,\mathrm{Mpc}$. In addition to that, the uncertainties on H_{eq} were estimated through the Eq. 4.15, obtained with the Theory of error propagation (Lindberg (2000)). D_L and ν were assumed to be without uncertainties.

$$\Delta H_{eq} = H_{eq}\frac{2}{7}\sqrt{\left(\frac{\Delta F(\nu)}{F(\nu)}\right)^2 + \left(\frac{3\Delta\theta}{\theta}\right)^2} \tag{4.15}$$

The values of the magnetic field of equipartition for each component, with the associated uncertainty, are collected in Tab. 4.3.

H_{eq} relations

As for the brightness temperature, also for the magnetic field it was possible to search for a correlation with other parameters. The first physical quantities that have been investigated are the H_{eq} and the distance from the core r (Fig. 4.22). Similarly to what have already been done with the others quantities, a linear fit was performed. The model equation chosen to fit the data was again $y = ax + b$, since on the log scale, the expected trend is supposed to be linear.

[3]Wright (2006) with standard ΛCDM parameters ($H_0 = 69.6$ $\Omega_M = 0.286$ $\Omega_\Lambda = 0.714$) taken from Bennett et al. (2014)

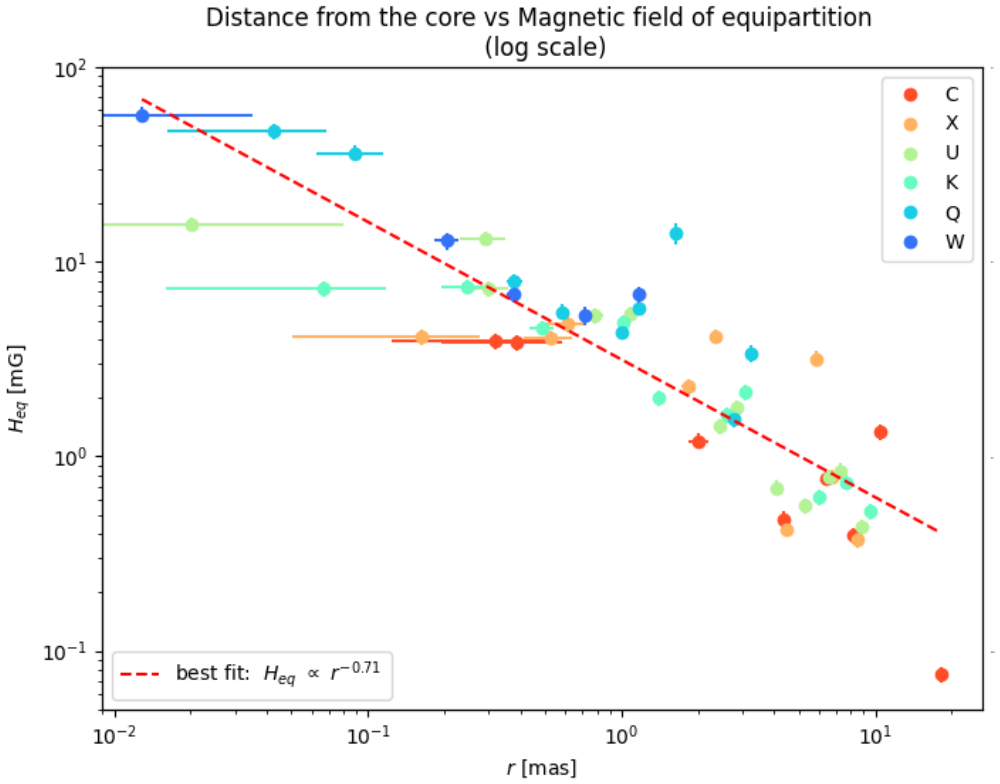

Figure 4.22: Equipartition magnetic field H_{eq} in [mG] vs the distance from the core r in [mas] in logarithmic scale. The error bar represents the uncertainties computed as explained in 4.4 and 4.15. The red dashed line represent the best fit for the data points, estimated with the model equation $y = ax + b$. The different colors represent different bands as can be seen from the legend.

As can be seen from the legend, the best fit is obtain for $H_{eq} \propto r^{\sim -0.71}$. Therefore, it can be deducted that components closer to the core usually have an higher value of H_{eq} and vice versa. Here as well, there are some points that present a large errorbar. This problem is overcome as explained in discussion of the Fig. 4.19.
Another plot was obtained in order to search for a correlation between H_{eq} and θ. This is shown in the Fig. 4.23. Also for these quantities, a linear fit was performed. The model equation chosen to fit the data was again $y = ax + b$, since on the log scale, the expected trend is supposed to be linear.

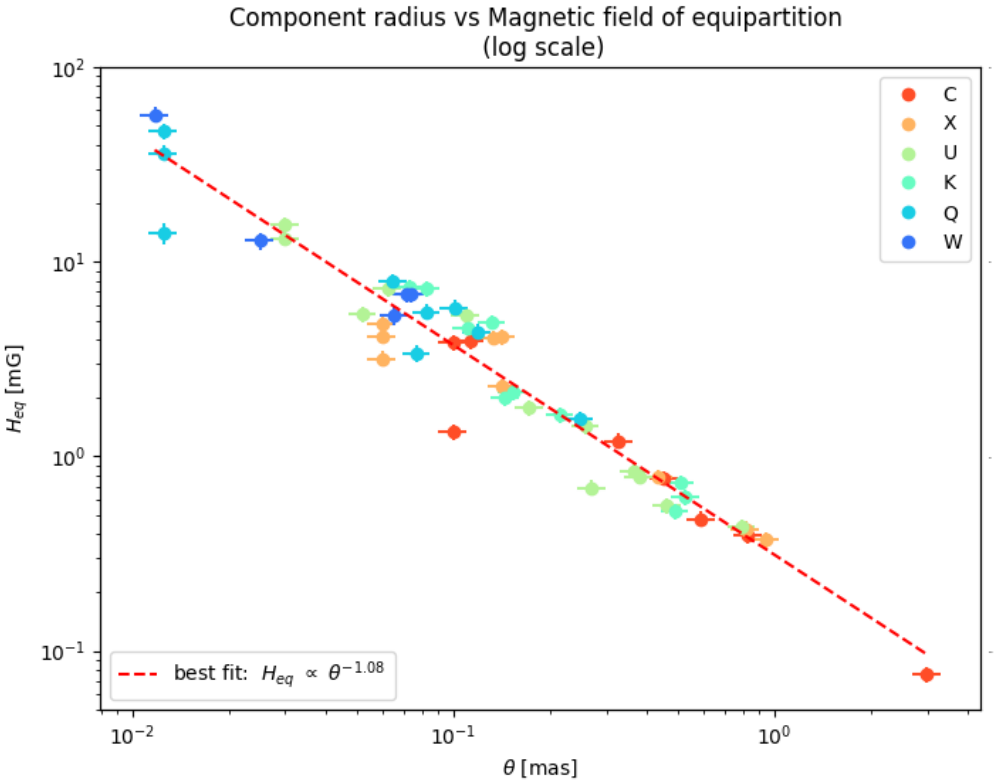

Figure 4.23: Equipartition magnetic field of H_{eq} in [mG] vs the size of the components θ in [mas] in logarithmic scale. The error bar represents the uncertainties computed as explained in 4.4 and 4.15. The red dashed line represent the best fit for the data points, estimated with the model equation $y = ax + b$. The different colors represent different bands as can be seen from the legend.

As can be seen from the legend, the best fit is obtain for $r \propto \theta^{\sim -1}$. Therefore, it can be deducted that smaller components usually have an higher value of H_{eq} and vice versa. Moreover, this plot has a small scatter. The trend with θ^{-1} is expected in the case of adiabatic expansion.
With a multifrequency dataset, it is possible to carry out a thorough analysis, and test whether there is a dependency on frequency for the magnetic field. Theoretically, H_{eq} should be an invariant for the frequency. In order to perform this analysis, the components have been corrected for the core shift and selected with the following criteria. A component is recognized at two different frequencies if:

$$|r_1 - r_2| < (\theta_1/2 + \theta_2/2) \text{ and } \frac{\theta_1}{\theta_2} < 1.3 \text{ and } \frac{\theta_2}{\theta_1} < 0.7 \tag{4.16}$$

where the subscript 1 indicates the component at the lower frequency and the subscript 2 indicates the component at the following one. From these conditions, 24 components were recognized at two frequencies, as presented in the left panel of Fig. 4.24.

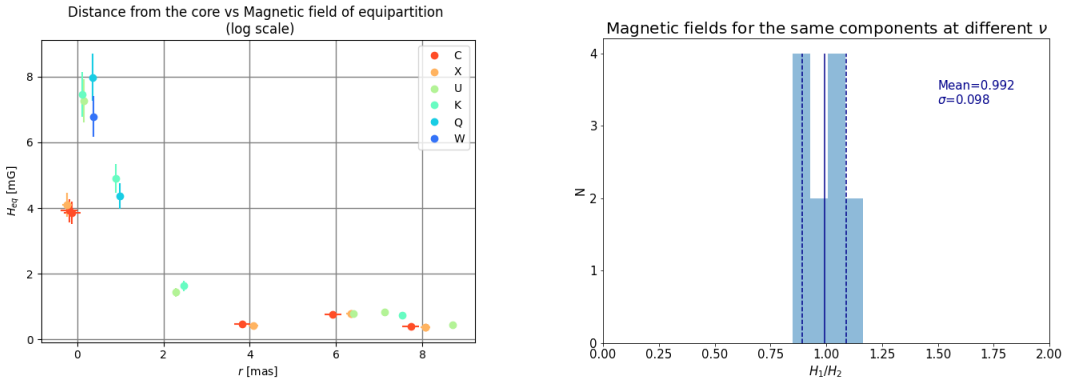

Figure 4.24: **Left:** Equipartition magnetic field of H_{eq} in [mG] vs the size of the components θ in [mas]. The 24 components were selected according to the Eq. 4.16. Different colors represent different bands as can be seen from the legend. The error bar represents the uncertainties computed as explained in 4.4 and 4.15. A grid is plotted in order to better see the positions and the value of the magnetic field. **Right:** An histogram representing the ratio between the magnetic field of equipartion found in the selected component at the lower frequency H_1 and at the following one H_2. The solid blue line represent the mean value (0.992) and the dashed ones the mean $\pm$ the standard deviation $\sigma = 0.098$. The mean and σ values are also written on the plot. The histogram bin is 4, since the number of values is 12.

The right panel of Fig. 4.24, represent an histogram with the ratio between the magnetic field of equipartion found in the selected component at the lower frequency H_1 and at the following one H_2. For all the components, this ratio is pretty close to 1 with a mean value of 0.992 and a standard deviation $\sigma = 0.098$. This is a strong confirmation that the equipartition magnetic field does not depend on the frequency. What gives this result even more importance is the fact that there is no selection condition on the flux density nor the magnetic field but only on the position and size of each component (Eq. 4.16).
Lastly, it was computed the plot between the brightness temperature T_B and the magnetic field of equipartition H_{eq}. A linear fit was performed. The model equation chosen to fit the data was again $y = ax + b$, since on the log scale, the expected trend is supposed to be linear.

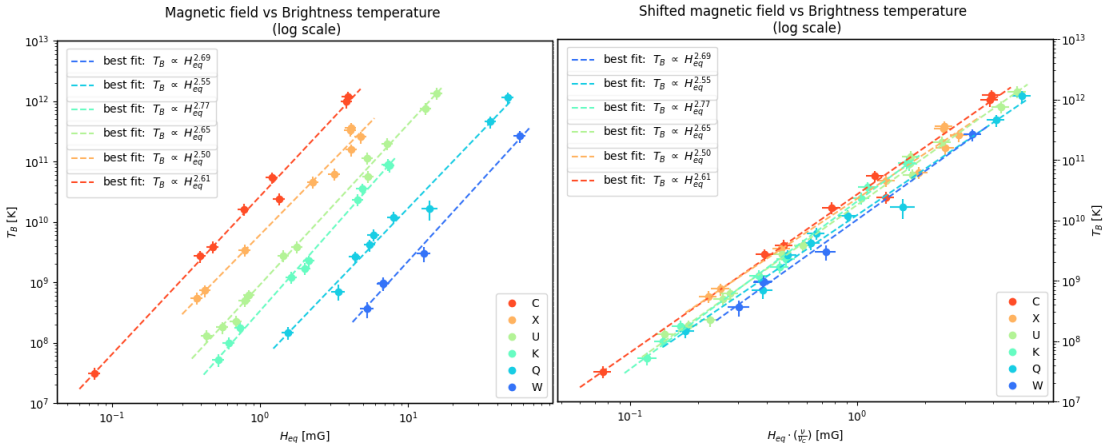

Figure 4.25: **Left:** The brightness temperature T_B in [K] vs equipartion magnetic field H_{eq} in [mG] in logarithmic scale. The error bar represents the uncertainties computed as explained in 4.4.2 and 4.4.1. The dashed lines represent the best fit for the data points of each bands, estimated with the model equation $y = ax + b$. The different colors represent different bands as can be seen from the legend. **Right:** The brightness temperature T_B in [K] vs equipartion magnetic field of shifted with the frequency $H_{eq}\dfrac{\nu}{\nu_C}$ in [mG] in logarithmic scale. The error bar represents the uncertainties computed as explained in 4.4.2 and 4.4.1. The dashed lines represent the best fit for the data points of each bands, estimated with the model equation $y = ax + b$. The different colors represent different bands as can be seen from the legend.

For data taken at any given band, a clear and tight correlation between H_{eq} and T_B is well visible in the Fig. 4.25 and supported by numerical fits. This correlation becomes even more striking when the different bands are considered all together, by shifting each H_{eq} by the ratio of the observed frequency to the reference C band. From the legends it is possible to see that the values of the exponents span from ≈ 2.49 to ≈ 2.77 and the mean value is ≈ 2.63. Such a tight correlation over two orders of magnitude in H_{eq} and over five orders of magnitude in T_B, finds a natural origin in the common dependence of T_B and H_{eq}. As can be inferred from Eqs. (4.11) and (4.13) the common quantities are the component size θ and the flux density F_ν.

Band	Flux (Jy)	Distance (mas)	Angular size (mas)	Theta (deg)	Beam min (mas)	T (K)	H (mG)
C	1.17 ± 0.12	0.32 ± 0.19	0.11 ± 0.01	79.79	1.93	1.175 ± 0.263	3.92 ± 0.35
C	0.75 ± 0.08	0.39 ± 0.19	0.1 ± 0.01	-125.36	1.93	0.971 ± 0.217	3.85 ± 0.35
C	0.45 ± 0.05	2.02 ± 0.19	0.33 ± 0.03	69.6	1.93	0.054 ± 0.012	1.2 ± 0.11
C	0.26 ± 0.03	6.43 ± 0.19	0.46 ± 0.05	62.19	1.93	0.016 ± 0.004	0.77 ± 0.07
C	0.1 ± 0.01	4.33 ± 0.19	0.59 ± 0.06	67.27	1.93	0.004 ± 0.001	0.48 ± 0.04
C	0.14 ± 0.01	8.24 ± 0.19	0.83 ± 0.08	64.59	1.93	0.003 ± 0.001	0.39 ± 0.04
C	$0.02 \pm 2e-03$	18.21 ± 0.19	3.0 ± 0.3	63.71	1.93	$3e-05 \pm 7e-06$	0.08 ± 0.01
C	$0.02 \pm 2e-03$	10.48 ± 0.19	0.1 ± 0.01	64.17	1.93	0.024 ± 0.005	1.34 ± 0.12
X	1.59 ± 0.16	0.16 ± 0.11	0.14 ± 0.01	67.35	1.13	0.356 ± 0.08	4.1 ± 0.37
X	1.3 ± 0.13	0.53 ± 0.11	0.13 ± 0.01	-116.84	1.13	0.327 ± 0.073	4.07 ± 0.37
X	0.2 ± 0.02	1.83 ± 0.11	0.14 ± 0.01	67.67	1.13	0.045 ± 0.01	2.28 ± 0.21
X	0.14 ± 0.01	6.75 ± 0.11	0.44 ± 0.04	61.1	1.13	0.003 ± 0.001	0.79 ± 0.07
X	0.11 ± 0.01	4.48 ± 0.11	0.82 ± 0.08	66.71	1.13	$0.001 \pm 1e-04$	0.42 ± 0.04
X	0.11 ± 0.01	8.47 ± 0.11	0.94 ± 0.09	64.9	1.13	$0.001 \pm 1e-04$	0.37 ± 0.03
X	0.05 ± 0.01	5.89 ± 0.11	0.06 ± 0.01	61.73	1.13	0.062 ± 0.014	3.18 ± 0.29
X	0.12 ± 0.01	2.34 ± 0.11	0.06 ± 0.01	68.82	1.13	0.156 ± 0.035	4.15 ± 0.37
X	0.2 ± 0.02	0.61 ± 0.11	0.06 ± 0.01	69.78	1.13	0.255 ± 0.057	4.77 ± 0.43
U	0.5 ± 0.05	0.29 ± 0.06	$0.03 \pm 3e-03$	-121.97	0.6	0.758 ± 0.17	13.21 ± 1.19
U	0.88 ± 0.09	0.02 ± 0.06	$0.03 \pm 3e-03$	169.52	0.6	1.351 ± 0.302	15.57 ± 1.41
U	0.55 ± 0.06	0.3 ± 0.06	0.06 ± 0.01	63.15	0.6	0.195 ± 0.044	7.27 ± 0.66
U	0.99 ± 0.1	0.78 ± 0.06	0.11 ± 0.01	64.94	0.6	0.114 ± 0.025	5.31 ± 0.48
U	0.08 ± 0.01	2.85 ± 0.06	0.17 ± 0.02	66.29	0.6	0.004 ± 0.001	1.77 ± 0.16
U	0.13 ± 0.01	2.44 ± 0.06	0.26 ± 0.03	68.37	0.6	0.003 ± 0.001	1.44 ± 0.13
U	0.06 ± 0.01	7.27 ± 0.06	0.37 ± 0.04	60.5	0.6	$0.001 \pm 1e-04$	0.84 ± 0.08
U	$0.03 \pm 3e-03$	5.28 ± 0.06	0.46 ± 0.05	67.7	0.6	$2e-04 \pm 4e-05$	0.56 ± 0.05
U	0.11 ± 0.01	1.08 ± 0.06	0.05 ± 0.01	66.04	0.6	0.057 ± 0.013	5.37 ± 0.49
U	0.06 ± 0.01	8.85 ± 0.06	0.79 ± 0.08	64.62	0.6	$1e-04 \pm 3e-05$	0.44 ± 0.04
U	0.05 ± 0.01	6.54 ± 0.06	0.38 ± 0.04	63.1	0.6	$5e-04 \pm 1e-04$	0.79 ± 0.07
U	$0.01 \pm 1e-03$	4.09 ± 0.06	0.27 ± 0.03	66.18	0.6	$2e-04 \pm 5e-05$	0.69 ± 0.06
K	0.91 ± 0.09	0.07 ± 0.05	0.08 ± 0.01	-149.77	0.51	0.089 ± 0.02	7.31 ± 0.66
K	0.68 ± 0.07	0.25 ± 0.05	0.07 ± 0.01	72.02	0.51	0.085 ± 0.019	7.46 ± 0.67
K	0.43 ± 0.04	0.49 ± 0.05	0.11 ± 0.01	63.2	0.51	0.023 ± 0.005	4.59 ± 0.41
K	0.92 ± 0.09	1.01 ± 0.05	0.13 ± 0.01	64.93	0.51	0.035 ± 0.008	4.9 ± 0.44
K	0.08 ± 0.01	2.59 ± 0.05	0.22 ± 0.02	67.59	0.51	$0.001 \pm 2e-04$	1.63 ± 0.15
K	0.08 ± 0.01	3.08 ± 0.05	0.15 ± 0.02	67.0	0.51	0.002 ± 0.001	2.14 ± 0.19
K	0.07 ± 0.01	7.65 ± 0.05	0.51 ± 0.05	61.79	0.51	$2e-04 \pm 4e-05$	0.74 ± 0.07
K	0.05 ± 0.01	1.39 ± 0.05	0.15 ± 0.01	66.17	0.51	$0.002 \pm 4e-04$	2.01 ± 0.18
K	$0.04 \pm 5e-03$	5.97 ± 0.05	0.53 ± 0.05	64.63	0.51	$1e-04 \pm 2e-05$	0.62 ± 0.06
K	$0.02 \pm 2e-03$	9.57 ± 0.05	0.49 ± 0.05	64.63	0.51	$5e-05 \pm 1e-05$	0.52 ± 0.05
Q	0.37 ± 0.04	1.18 ± 0.03	0.1 ± 0.01	61.98	0.26	0.006 ± 0.001	5.81 ± 0.53
Q	0.22 ± 0.02	1.0 ± 0.03	0.12 ± 0.01	62.45	0.26	0.003 ± 0.001	4.36 ± 0.4
Q	0.3 ± 0.03	0.38 ± 0.03	0.06 ± 0.01	61.45	0.26	0.012 ± 0.003	7.98 ± 0.72
Q	1.07 ± 0.11	0.04 ± 0.03	$0.01 \pm 1e-03$	-99.15	0.26	1.138 ± 0.254	47.03 ± 4.25
Q	0.43 ± 0.04	0.09 ± 0.03	$0.01 \pm 1e-03$	56.87	0.26	0.454 ± 0.102	36.17 ± 3.27
Q	0.17 ± 0.02	0.59 ± 0.03	0.08 ± 0.01	58.06	0.26	0.004 ± 0.001	5.52 ± 0.5
Q	0.05 ± 0.01	2.77 ± 0.03	0.25 ± 0.02	66.66	0.26	$1e-04 \pm 3e-05$	1.55 ± 0.14
Q	0.02 ± 0.01	3.23 ± 0.03	0.08 ± 0.01	65.18	0.26	$0.001 \pm 2e-04$	3.38 ± 0.35
Q	$0.02 \pm 4e-03$	1.64 ± 0.03	$0.01 \pm 1e-03$	66.12	0.26	0.017 ± 0.006	14.05 ± 1.72
W	0.87 ± 0.09	0.01 ± 0.02	$0.01 \pm 1e-03$	147.94	0.22	0.262 ± 0.059	56.99 ± 5.15
W	0.04 ± 0.01	0.21 ± 0.02	$0.02 \pm 1e-03$	-108.4	0.22	0.003 ± 0.001	12.81 ± 1.31
W	0.12 ± 0.01	0.38 ± 0.02	0.07 ± 0.01	64.31	0.22	$0.001 \pm 2e-04$	6.79 ± 0.63
W	0.13 ± 0.01	1.17 ± 0.02	0.07 ± 0.01	62.25	0.22	$0.001 \pm 2e-04$	6.83 ± 0.63
W	0.04 ± 0.01	0.72 ± 0.02	0.07 ± 0.01	58.96	0.22	$3e-04 \pm 1e-04$	5.31 ± 0.57

Table 4.3: Components found with the modelfitting with their parameters. (1) band (2) flux density and its error in Jy (3) distance from the core and its error in mas (4) FWHM of the fitted Gaussian and its error in mas (5) angle between the core and the center of the component Φ in deg (6) minor axis of the beam in mas (7) brightness temperature of the component and its error in 10^{12}K (8) equipartition magnetic field and its error in mG.

Chapter 5

Conclusions and further studies

Throughout this thesis we presented a set of multi-frequency, high angular resolution observations of the broad line radio galaxy 3C111. The images were obtained in full polarization with the VLBA, and they allow for the first time to study this jet with simultaneous data up to 86 GHz. In the highest angular resolution image, our convolving beam is as small as 0.22 [mas], corresponding to ≈ 0.3 pc. The source is well detected at all frequencies, dominated by a compact core of brightness variable between ≈ 3 [Jy] and ≈ 1 [Jy] Jy (at X and W bands, respectively). From the core, a one sided jet emerges, extending up to ≈ 25 [mas] in length in the lowest frequency image. The jet is remarkably straight, being oriented in position angle $\approx 65°$ and showing little or no evidence of bending over its full extension. Thanks to the multi-frequency analysis, it was possible to estimate the position of the peak in each bands and perform the core shift analysis, finding a trend of $r \propto \nu^{-1.20\pm0.18}$, in agreement with the literature (Dodson et al. (2017) and Lobanov (1998))
By comparing the fluxes at different frequencies, the spectral index was computed both in the core region and throughout all the jet. For the core, the spectral index varies from $\alpha \approx 1.5$ in the lower frequency pair (CX) to $\alpha \approx -0.5$ in the higher frequency pair (QW), changing from the optically thick regime to the thin one. The spectral index along the jet is generally steep, reaching the minimum value of $\alpha \approx -3.3$ at the higher frequency pair. When the same region appears in more than one frequency pair, there is clear evidence of a high frequency steepening, signature of radiative losses. The jet also presents an optically thick feature at ≈ 1.5 mas that needs to be further studied.
The polarized emission lies mostly in the jet at all the frequencies and, as the frequency is increasing, this emission arises also from regions progressively closer to the jet basis. The integrated fraction of polarization values that spans from a minimum of 4.85% in the X band (corresponding to the higher flux density) to 65.97% in the W band (corresponding to the lower flux density). The fraction of polarization computed at the peak of the polarization maps is variable between 2.19% and 14.86% at W and K band, respectively.
Thanks to the polarized regions common to various frequencies, the rotation measure it is computed for the U, K and Q bands. The UKQ polarization images are sensitive to the inner portion of the jet, out to about 3 mas ($\approx 3pc$) from the core. It is possible to recognize two regions. The brightest one is at about 1 [mas] from the core and shows values of rotation measure from ≈ 7500 to ≈ 12500 [rad/m^2]. This corresponds to the location with inverted spectrum emission. This could be

consistent with the presence of substantial amount of external magnetised plasma responsible for both Faraday rotation and free-free absorption. The magnetic field orientation is almost perpendicular to the jet axis in the inner part and it is titled to $\approx 60^{\circ}$ with the jet axes in the outer part. At a distance of about 3 [mas], there are two additional regions with RM values from ≈ 10000 to ≈ 12500 [rad/m^2]. In this outer regions, the magnetic field seems to start aligning to the jet axis. At the lowest frequencies the outer part of the jet is sampled. At these frequencies, the only region with common polarised emission is at a distance of ≈ 6 [mas] from the core. The RM detected across the jet structure, goes from about 650 [rad/m^2] down to ≈ 50 [rad/m^2]. The magnetic field orientation has a coherent gradient that spans from being perpendicular to the jet axis to being almost parallel to it, in the same jet region, in agreement with the simulations for an helical structure (Fuentes et al. (2021)).

From the model-fitting analysis, a total of 53 components have been found, with various size and distance from the core. The one that lies at the longest distance (≈ 18 [mas]) is found in the C band and has the maximum angular size (≈ 3 [mas]). Thanks to these components it is possible to estimate the brightness temperature distribution across the source for all the frequencies. The values found go from a minimum of 3.1×10^7 K (corresponding to the most distant component) in the C band, to a maximum of 1.3×10^{12} K in the U band, that is probably due to the blending of two region that could not be resolved at this frequency. Under the assumption that the emitting region is at the minimum total energy, the equipartition magnetic field was estimated. The values ranges from 0.08 [mG] in the C band (the same component that has the minimum brightness temperature) to 56.99 [mG] for the smallest component in the W band. Moreover, it was possible to compare the physical parameters of each components and find various relations between them. These plots show interesting trends for all of them. The brightness temperature and the magnetic field show a strong correlation across all the components and frequencies with a mean trend $T_B \propto H_{eq}^{2.62}$. In conclusion, this thesis has provided interesting insights in the AGN field and it fits into a wide research analysis carried out throughout many years, such as Lobanov (1998), Schulz et al. (2020), Giroletti et al. (2004). In this context, our results shows unique features in the wide range of frequencies, and in the rich structure in total intensity and polarization. Moreover, jet simulations works (such as Fuentes et al. (2021)) need studies like the one presented in this thesis to constrain the parameters in order to infer the complex jet physics. Therefore the analysis carried out in here, can provide a concrete comparison to the simulations.

Appendix A

The K band problem

The K band had probably some issues during the observations. Unfortunately, it was not possible to fully understand what happened but it was possible to work on the visibilities. In fact, the problem regarded the fact that this band has an integrated total intensity that was lower $\approx 20\%$ than expected, as can be seen in Fig. A.1.

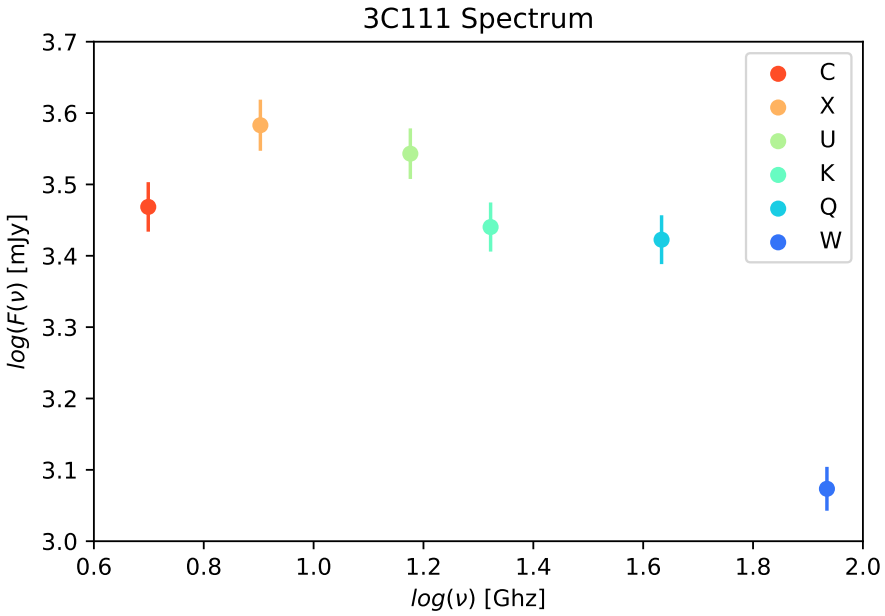

Figure A.1: The spectrum of 3C111, before the correction. The values represent the integrated values of the flux densities for each bands.

Therefore, in order to see if the problem was only related to the source or if it was an issue that affected all the observation, another analysis was performed. By looking at the Tab. 3.1, it can be seen that, apart from 3C111, there are other sources that were observed (the calibrators). 3C84 is a bright source that was used as a flux calibrator in this project. Since the calibration was performed with all the sources, it was also possible to produce the image for 3C84 at all the frequencies. These images, since the number of visibilities that they had was too little, are not so reliable for what concerns the structure of 3C84 but they could be used for the

spectrum. In fact, it was possible to compute the total integrated flux density for 3C84 at all the frequency (Fig. A.2)

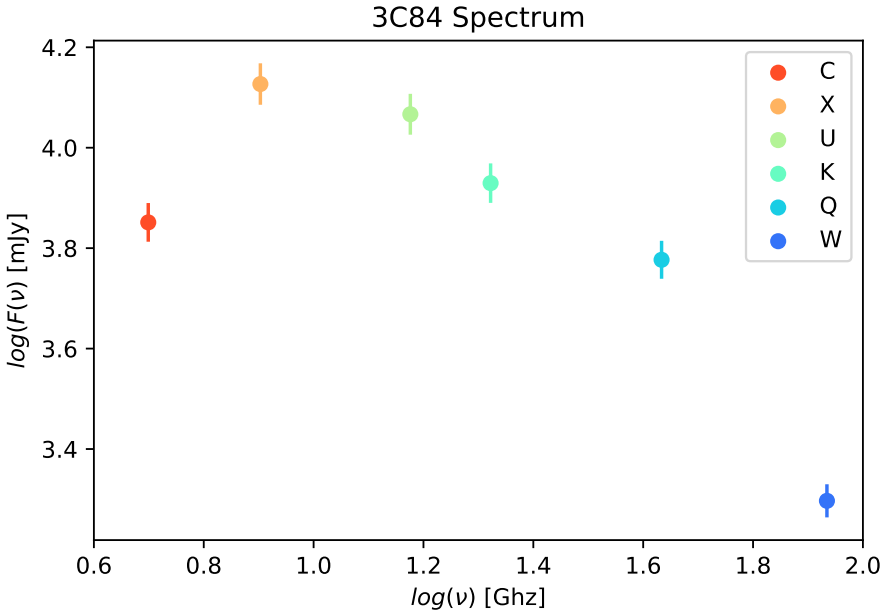

Figure A.2: The spectrum of 3C84. The values represent the integrated values of the flux densities for each bands.

Also for 3C84 the K band seems to be too low. Hence, it was possible fit the spectrum without taking into account the value for the K band. Then, by comparing the fitted value with the actual one, the scaling factor could be estimated. This was done for both 3C84 and 3C111 and the two scaling factor were both around 1.22. This scaling factor was applied to the visibilities of 3C111 in the K band, through AIPS. The scaled plot is the one presented in Fig. 4.2.

The results of this thesis work will be submitted to the Astrophysical Journal (ApJ).

Bibliography

Baldi R., Capetti A., Giovannini G., 2016, *The new class of FR0 galaxies*, https://arxiv.org/pdf/1510.04272.pdf

Bennett C. L., et al., 2014, *The 1% concordance Hubble constant*, https://arxiv.org/pdf/1406.1718.pdf

Beuchert T., et al., 2018, *VLBA polarimetric monitoring of 3C111*, https://arxiv.org/pdf/1711.01593.pdf

Condon J., 2016, *Essential Radio Astronomy*, https://science.nrao.edu/opportunities/courses/era/

Cotton W., 1995, *Very Long Baseline Interferometry and the VLBA, Astronomical Society of the Pacific Conference Series, Vol. 82*, https://www.aspbooks.org/publications/82/189.pdf

Dodson R., et al., 2017, *High-precision Astrometric Millimeter Very Long Baseline Interferometry Using a New Method for Multi-Frequency Calibration*, https://arxiv.org/pdf/1612.02958.pdf

Fanaroff Riley 1974, *The morphology of extragalactic radio sources of high and low luminosity*, https://articles.adsabs.harvard.edu/pdf/1974MNRAS.167P..31F

Fuentes A., et al., 2021, *Magnetized relativistic jets and helical magnetic fields*, https://www.aanda.org/articles/aa/abs/2021/06/aa40659-21/aa40659-21.html

Giommi P., et al., 2012, *A simplified view of blazars: clearing the fog around long-standing selection effects*, https://arxiv.org/pdf/1110.4706.pdf

Giroletti M., Giovannini G., et al., 2004, *Parsec-Scale Properties of Markarian 501*, https://iopscience.iop.org/article/10.1086/379663/pdf

Gómez J. L., et al., 2022, *Probing the Innermost Regions of AGN Jets and Their Magnetic Fields with RadioAstron. V. Space and Ground Millimeter-VLBI Imaging of OJ 287*, https://arxiv.org/pdf/2111.11200.pdf

Jae-Young K., 2018, *High Spatial Resolution Millimeter VLBI Studies of the Nearby Radio Galaxies M 87 and 3C 84*, https://kups.ub.uni-koeln.de/9341/1/thesis.pdf

Jorstad S. G., Marscher A. P., et al., 2005, *Polarimetric Observations of 15 Active Galactic Nuclei at High Frequencies: Jet Kinematics from Bimonthly Monitoring with the Very Long Baseline Array*, https://iopscience.iop.org/article/10.1086/444593/pdf

Lindberg V., 2000, *Uncertainties and Error Propagation Part I of a manual on Uncertainties, Graphing, and the Vernier Caliper*, https://www.geol.lsu.edu/jlorenzo/geophysics/uncertainties/Uncertaintiespart2.html

Lister M., 2018, *MOJAVE. XV. VLBA 15 GHz Total Intensity and Polarization Maps of 437 Parsec-scale AGN Jets from 1996 to 2017*, https://iopscience.iop.org/article/10.3847/1538-4365/aa9c44/pdf

Lobanov A. P., 1998, *Ultracompact jets in active galactic nuclei*, https://articles.adsabs.harvard.edu/pdf/1998a&a...330...79l

Madore B. F., 2002, *Fanaroff-Riley classification*, https://ned.ipac.caltech.edu/level5/Glossary/Essay_fanaroff.html

Myserlis I., 2015, *A framework for the study of physical conditions in astrophysical plasmas through radio and optical polarization: Application to extragalactic jets*, https://kups.ub.uni-koeln.de/6967/1/Myserlis_I_PhD.pdf

Orienti M., Dallacasa D., 2008, *Are young radio sources in equipartition?*, https://www.aanda.org/articles/aa/pdf/2008/33/aa09948-08.pdf

Orienti M., Venturi T., Dallacasa D., et al., 2011, *Multi-epoch parsec-scale observations of the blazar PKS 1510-089*, https://arxiv.org/pdf/1106.3205.pdf

Padovani P., et al., 2017, *Active galactic nuclei: what's in a name?*, https://arxiv.org/pdf/1707.07134.pdf

Pushkarev A. B., et al., 2012, *MOJAVE: Monitoring of Jets in Active galactic nuclei with VLBA Experiments IX. Nuclear opacity*, https://www.aanda.org/articles/aa/pdf/2012/09/aa19173-12.pdf

Schmidt M., 1963, *3C 273 : A Star-Like Object with Large Red-Shift*, https://www.nature.com/articles/1971040a0

Schulz R. F., 2012, *A Study of the Active Galaxy 3C111 with mm-VLBI*, https://www3.mpifr-bonn.mpg.de/div/vlbi/globalmm/pspdf/MSc_Schulz_3C111.2012.pdf

Schulz R., et al., 2020, *Sub-milliarcsecond imaging of a bright flare and ejection event inthe extragalactic jet 3C 111*, https://arxiv.org/pdf/2009.01294.pdf

Shepherd M., 1997, *Difmap: an Interactive Program for Synthesis Imaging*, https://www.cv.nrao.edu/adass/adassVI/shepherdm.html

Thompson A. R., Moran J. M., Swenson Jr. G. W., 2017, *Interferometry and Synthesis in Radio Astronomy*, 3 edn. Springer

Urry C. M., Padovani P., 1995, *Unified Schemes for Radio-Loud Active Galactic Nuclei*, https://articles.adsabs.harvard.edu/pdf/1995PASP..107..803U

Volonteri M., et al., 2012, *Black holes in the early Universe*, https://iopscience.iop.org/article/10.1088/0034-4885/75/12/124901

Wright E. L., 2006, *A Cosmology Calculator for the World Wide Web*, https://arxiv.org/pdf/astro-ph/0609593.pdf